

Skoltech

Skolkovo Institute of Science and Technology

TRANSITION METAL COORDINATION POLYMERS DERIVED FROM 1,2,4,5-
BENZENETETRAAMINE AS ACTIVE MATERIALS FOR ENERGY STORAGE
DEVICES

Doctoral Thesis

by

ROMAN R. KAPAEV

DOCTORAL PROGRAM IN MATERIALS SCIENCE AND ENGINEERING

Supervisor:
Professor Keith J. Stevenson

Moscow – 2021

© Roman R. Kapaev 2021

I hereby declare that the work presented in this thesis was carried out by myself at Skolkovo Institute of Science and Technology, Moscow, except where due acknowledgement is made, and has not been submitted for any other degree.

Candidate (Roman R. Kapaev)

Supervisor (Prof. Keith J. Stevenson)

Abstract

There is an on-growing demand for the next generation of energy storage materials, which have high specific capacity, excellent high-rate capabilities, and durability. Transition metal coordination polymers with π -d conjugation have recently attracted attention as candidates for the electrode materials in advanced batteries and supercapacitors. However, this class of materials remains poorly studied.

This Thesis is dedicated to Ni- and Cu-based coordination compounds derived from 1,2,4,5-benzenetetraamine, a commercially available ligand. The materials were synthesized, characterized using a set of physicochemical techniques, and tested in positive or negative electrodes for energy storage devices that use alkali metal ions as charge carriers.

As the positive electrode materials, the compounds exhibited redox activity in half-cells with lithium metal as the anode. For the copper-based material, higher specific capacities of up to 262 mA h g^{-1} were demonstrated. However, the cycling stability of the polymers was inferior. The charge storage mechanisms were studied using *ex situ* X-ray photoelectron spectroscopy.

It was shown that the compounds might be used as anode materials for metal-ion batteries. Particularly, the nickel-based coordination polymer exhibited a combination of attractive properties in Li-based, Na-based and K-based cells, such as high specific capacities ($>200 \text{ mA h g}^{-1}$), high-rate capabilities and excellent cycling stability. The material might be considered a promising alternative to lithium titanate. It has safe operation potentials ($>0.5 \text{ V vs. M}^+/\text{M}$) while possessing higher capacities and being compatible with various charge carriers. Basing on the electrochemical features of the material, as well as data from *ex situ* X-ray photoelectron spectroscopy, *operando* and *ex situ* X-ray diffraction, and *operando* Raman spectroscopy measurements, it was concluded that the charge storage mechanism involved reversible two-electron reduction of the polymer repeating units. In the partially reduced states of the Na- and K-based systems, the Ni-based material showed features of intercalation pseudocapacitance.

Publications

Articles in peer-reviewed journals:

1. Kapaev, R. R.; Olthof, S.; Zhidkov, I. S.; Kurmaev, E. Z.; Stevenson, K. J.; Meerholz, K.; Troshin, P. A., Nickel(II) and Copper(II) Coordination Polymers Derived from 1,2,4,5-Tetraaminobenzene for Lithium-Ion Batteries. *Chem. Mater.* **2019**, *31* (14), 5197-5205. DOI: [10.1021/acs.chemmater.9b01366](https://doi.org/10.1021/acs.chemmater.9b01366).
2. Kapaev, R. R.; Zhidkov, I. S.; Kurmaev, E. Z.; Stevenson, K. J.; Troshin, P. A., A nickel coordination polymer derived from 1,2,4,5-tetraaminobenzene for fast and stable potassium battery anodes. *Chem. Commun.* **2020**, *56* (10), 1541-1544. DOI: [10.1039/c9cc07748k](https://doi.org/10.1039/c9cc07748k).
3. Kapaev, R. R.; Troshin, P. A., Organic-based active electrode materials for potassium batteries: status and perspectives. *J. Mater. Chem. A* **2020**, *8* (34), 17296-17325. DOI: [10.1039/D0TA04741D](https://doi.org/10.1039/D0TA04741D).

Submitted manuscripts:

1. Kapaev, R. R.; Zhugayevych, A.; Stevenson, K. J., Charge Storage Mechanisms of a π -d Conjugated Polymer for Alkali-Ion Battery Anodes. *Submitted 2021*.

Conferences:

1. Kapaev, R.R.; Stevenson, K.J.; Troshin, P.A., "Metal-Ion Batteries Based on New Copper and Nickel Coordination Polymers with Aromatic Polyamine Ligands". *Electrochemical Conference on Energy and the Environment (ECEE 2019)*, July 21–26, **2019**, Glasgow, Scotland (oral talk).
2. Kapaev, R.R.; Stevenson, K.J.; Troshin, P.A., "Ni(II) and Cu(II) coordination polymers derived from aryl amine for Li-ion batteries". *MIT-Skoltech*

Conference: “Collaborative Solutions for Next Generation Education, Science and Technology”, October 15–16, **2018**, Moscow, Russia (poster).

3. Kapayev, R.R.; Troshin, P.A., “Coordination polymers derived from aryl amines and transition metal salts for lithium-ion batteries”. *III International Conference of Young Scientists 2018*, September 23–26, **2018**, Vozdvizhenskoe, Russia (poster).

Acknowledgements

This work could be accomplished only with the support and contributions from my mentors and colleagues at Skolkovo Institute of Science and Technology, Institute of Problems of Chemical Physics of the Russian Academy of Sciences (IPCP RAS), Zelinsky Institute of Organic Chemistry of the Russian Academy of Sciences (ZIOC RAS), Nesmeyanov Institute of Organoelement Compounds of the Russian Academy of Sciences (INEOS RAS), Ural Federal University (UrFU), University of Cologne, and Moscow State University (MSU).

Most of the work presented in this Thesis was done at Skoltech. Ball-milling of the samples was performed at IPCP RAS.

I would like to thank my advisor, Prof. Keith Stevenson, as well as my colleagues for their help and useful advice: Zoia Bobyleva, Dr. Aleksandra Boldyreva, Prof. Stanislav Fedotov, Dr. Vladislav Gorshkov, Dr. Maria Kirsanova, Irina Klimovich, Prof. Viktoria Nikitina, Artyom Novikov, Filipp Obrezkov, Sergey Porokhin, Dr. Sergey Ryazantsev, Dr. Pavel Troshin, Dr. Sergey Tsarev, Artem Zaikin, Dr. Maksim Zakharkin, Prof. Andriy Zhugayevych.

I want to acknowledge my colleagues who carried out some of the experiments featured in this Thesis. Solid-state NMR spectra were measured by Dr. Sergey Vasil'ev (IPCP RAS). X-ray photoelectron spectroscopy measurements were performed by Prof. Ivan Zhidkov (UrFU) and Dr. Selina Olthof (University of Cologne). Scanning electron microscopy images were acquired by Dr. Aleksey Galushko (ZIOC RAS). Olga Kraevaya (IPCP RAS) measured the electron spin resonance spectrum. Dr. Rina Takazova and Prof. Anastasia Buyanovskaya (INEOS RAS) carried out the elemental analysis.

I am grateful to my friends and family for their kind support.

Table of Contents

| | |
|--|----|
| Abstract..... | 3 |
| Publications..... | 4 |
| Acknowledgements | 6 |
| Table of Contents | 7 |
| List of Symbols, Abbreviations | 11 |
| List of Figures | 14 |
| List of Tables | 20 |
| Chapter 1. Introduction..... | 21 |
| Chapter 2. Literature review | 24 |
| 2.1. Working principles and terminology for metal-ion batteries and related energy storage technologies | 24 |
| 2.1.1. Definitions of metal-ion batteries, dual-ion batteries and pseudocapacitors | 24 |
| 2.1.2. Key characteristics of energy storage devices | 30 |
| 2.1.3. Requirements for the next generation of energy storage materials..... | 31 |
| 2.2. Structural features of coordination polymers with π -d conjugation | 34 |
| 2.3. Applications of π -d conjugated coordination polymers as active materials in energy storage devices | 36 |
| 2.3.1. Applications in supercapacitors | 36 |

| | |
|--|----|
| 2.3.2. Applications in cathodes for metal-ion batteries and dual-ion batteries..... | 40 |
| 2.3.3. Applications in anodes for metal-ion batteries | 47 |
| Chapter 3. Research objectives | 52 |
| Chapter 4. Experimental section | 53 |
| 4.1. Synthesis of NiTIB and CuTIB | 53 |
| 4.2. Ball-milling..... | 53 |
| 4.3. Electrode preparation | 53 |
| 4.3.1. Electrodes for testing cathode materials..... | 53 |
| 4.3.2. Electrodes for testing anode materials | 54 |
| 4.3.3. Electrodes for <i>ex situ</i> and operando XRD measurements | 54 |
| 4.3.4. Electrodes for operando Raman spectroscopy measurements..... | 55 |
| 4.4. Assembling of the electrochemical cells..... | 55 |
| 4.4.1. Galvanostatic charge-discharge and cyclic voltammetry | 55 |
| 4.4.2. <i>Ex situ</i> XRD measurements..... | 56 |
| 4.4.3. Operando XRD measurements | 56 |
| 4.4.4. Operando Raman spectroscopy measurements..... | 56 |
| 4.5. Electrochemistry | 57 |
| 4.5.1. Galvanostatic charge-discharge | 57 |
| 4.5.2. Cyclic voltammetry..... | 57 |
| 4.6. Sample preparation for <i>ex situ</i> XRD measurements | 57 |

| | |
|---|----|
| 4.7. <i>Operando</i> XRD measurement conditions | 58 |
| 4.8. <i>Operando</i> Raman spectroscopy measurement conditions..... | 58 |
| 4.9. Sample preparation for UV-Vis-NIR spectra measurements | 59 |
| 4.9.1. Film preparation..... | 59 |
| 4.9.2. Preparation of alkaliation solutions..... | 59 |
| 4.9.3. Alkaliation of the films..... | 59 |
| 4.9.4. Washing and drying of the films..... | 59 |
| 4.10. Sample preparation for <i>ex situ</i> XPS measurements | 59 |
| 4.11. Pellet preparation | 60 |
| 4.12. Deposition of conductive coating onto the pellets | 60 |
| 4.13. Characterization | 60 |
| 4.13.1. FTIR spectroscopy | 60 |
| 4.13.2. Raman spectroscopy..... | 60 |
| 4.13.3. UV-Vis-NIR spectroscopy | 60 |
| 4.13.4. Elemental analysis..... | 61 |
| 4.13.5. ESR spectroscopy..... | 61 |
| 4.13.6. Conductivity measurements..... | 61 |
| 4.13.7. Scanning electron microscopy | 61 |
| 4.13.8. Solid-state NMR spectroscopy | 61 |
| 4.13.9. XPS measurements..... | 62 |

| | |
|---|-----|
| 4.13.10. X-ray diffraction..... | 62 |
| Chapter 5. Results and Discussion | 64 |
| 5.1. Synthesis and characterization..... | 64 |
| 5.2. Applications as cathode materials..... | 71 |
| 5.2.1. Electrochemical properties | 71 |
| 5.2.2. Charge-discharge mechanisms | 75 |
| 5.3. Applications as anode materials | 76 |
| 5.3.1. Electrochemical properties | 76 |
| 5.3.2. Charge-discharge mechanisms | 87 |
| Chapter 6. Conclusions..... | 101 |
| Bibliography | 103 |
| Appendix A. Supplementary materials..... | 127 |

List of Symbols, Abbreviations

Symbols:

λ – wavelength

θ – angle of diffraction

C – capacitance

E – electrochemical potential

F – Faraday constant

I – current

M – molecular mass

n – number of transferred electrons

P – power

Q – capacity

t – time

v – potential sweep rate

V – voltage

W – energy

Abbreviations:

2D – two-dimensional

8OH-DBC – dibenzo[g,p]chrysene-2,3,6,7,10,11,14,15-octaol

acac – acetylacetonate

BHT – benzenhexathiolate

BTA – 1,2,4,5-benzenetetraamine

CMC – carboxymethylcellulose sodium salt

CP – cross-polarization

CV – cyclic voltammetry; cyclic voltammogram

DCD – 3,6-diimino-1,4-cyclohexadiene-1,4-diamine

DFT – density functional theory

DIBDT – 1,4-diiminobenzene-2,5-dithiolate

DME – 1,2-dimethoxyethane

DMC – dimethyl carbonate

DOL – 1,3-dioxolane

EC – ethylene carbonate

EDLC electrical double layer capacitor

EDX – energy-dispersive X-ray spectroscopy

ESR – electron spin resonance

ETT – ethenetetrathiolate

EXAFS – extended X-ray absorption fine structure

FTIR – Fourier-transform infrared

GCD – galvanostatic charge-discharge

HHTP – 2,3,6,7,10,11-hexahydroxytriphenylene

HIB – hexaiminobenzene

HITP – 2,3,6,7,10,11-hexaiminotriphenylene

ICE – initial Coulombic efficiency

LIB – lithium-ion battery

LTO – lithium titanate

MAS – magic angle spinning

MOF – metal-organic framework

NCA – $\text{LiNi}_x\text{Co}_y\text{Al}_z\text{O}_2$

NIR – near infrared

NMC – $\text{LiNi}_x\text{Mn}_y\text{Co}_z\text{O}_2$

NMR – nuclear magnetic resonance

PIB – potassium-ion battery

PVdF – poly(vinylidene difluoride)

RF – radio frequency

SEI – solid electrolyte interphase

SIB – sodium-ion battery

ssNMR – solid-state NMR

TFSI – lithium bis(trifluoromethanesulfonyl)imide

THQ – tetrahydroxy-1,4-benzoquinone

TIB – 1,2,4,5-tetraaminobenzene

TMS – tetramethylsilane

TTO – tetrathiooxalate

XANES – X-ray absorption near edge structure

XAS – X-ray absorption spectroscopy

XPS – X-ray photoelectron spectroscopy

XRD – X-ray diffraction

UV-Vis – ultraviolet-visible

List of Figures

| | |
|--|----|
| Figure 1. Schematic representation of the working principle of metal-ion batteries. ...25 | 25 |
| Figure 2. Features of materials for EDLCs, pseudocapacitors and batteries: CV profiles (a), GCD profiles (b) and dependencies of CV current on the scan rate (c). Reproduced with permission from ref. ⁵⁰ Copyright 2019, Wiley-VCH.26 | 26 |
| Figure 3. Types of pseudocapacitance. Reproduced with permission from ref. ⁵⁹ Copyright 2014, Royal Society of Chemistry.....28 | 28 |
| Figure 4. Electrochemical features of pseudocapacitive materials: CV profiles (a), GCD profiles (b) and Nyquist plots (c). Reproduced with permission from ref. ⁵⁹ Copyright 2014, Royal Society of Chemistry.28 | 28 |
| Figure 5. Orbital representation of a potential charge transport pathway in a coordination polymer with π -d conjugation. Reproduced from ref. ¹⁰⁷ under CC BY license. Copyright 2020, American Chemical Society.....34 | 34 |
| Figure 6. Hydroquinoid (2 ⁻), semiquinoid (1 ⁻) and quinoid (0) motifs of ligands in π -d conjugated coordination polymers. Reproduced from ref. ¹⁰⁷ under CC BY license. Copyright 2020, American Chemical Society.35 | 35 |
| Figure 7. Structure of NiHITP (a), relative size of NiHITP pores, Et ₄ N ⁺ , BF ₄ ⁻ ions and acetonitrile from the electrolyte (b) and cyclic voltammograms of NiHITP measured at a scan rate of 10 mV s ⁻¹ (c). Reproduced with permission from ref. ¹⁰⁸ Copyright 2017, Springer Nature.36 | 36 |
| Figure 8. Synthetic scheme for CuHIB and NiHIB (a), structure of CuHIB (b) and CV profiles of CuHIB (c) and NiHIB (d) measured at different scan rates. Reproduced with permission from ref. ¹¹⁰ Copyright 2018, Springer Nature.....38 | 38 |

Figure 9. Simulated structure of **NiBHT** (a), CV profiles of **NiBHT** measured at the scan rate of 5 mV s^{-1} with 1M LiPF_6 , NEt_4PF_6 , NEt_4BF_4 or NBu_4BF_4 solutions in acetonitrile as the electrolytes (b) and gravimetric capacitances for different electrolytes (b). Reproduced with permission from ref.¹¹² Copyright 2021, American Chemical Society.39

Figure 10. Schematic representation of charge-discharge mechanisms of **NiHIB** in Li-based batteries. Reproduced with permission from ref.¹¹⁴ Copyright 2018, Wiley-VCH.41

Figure 11. CV profiles of **Co_xNi_{1-x}HIB** at the potential scan rate of 0.5 mV s^{-1} obtained after ten pre-conditioning cycles (a); proposed charge-discharge mechanisms (b); structures of different motifs (c); charge-discharge curves of **Co_xNi_{1-x}HIB** at 100 mA g^{-1} . Reproduced with permission from ref.¹¹⁵ Copyright 2020, American Chemical Society.42

Figure 12. Charge-discharge voltage profiles of (a) and proposed charge-discharge mechanism of **CuTHQ** (b). Reproduced with permission from ref.¹¹⁶ Copyright 2020, Wiley-VCH.43

Figure 13. Scheme of a Zn-ion battery with **CuHHTP** (a), structure of **CuHHTP** (b) and proposed charge-discharge mechanism (c). Reproduced from ref.¹¹⁸ under CC BY license. Copyright 2019, The Authors.....44

Figure 14. Proposed charge-discharge mechanism of **NiTTO** in Na-based cells (a), CV profiles of **NiTTO** measured at 0.5 mV s^{-1} for different cycle numbers (b) and charge-discharge profiles of **NiTTO** at 0.1 A g^{-1} for different cycle numbers (c). Reproduced with permission from ref.¹²¹ Copyright 2019, Royal Society of Chemistry.....46

| | |
|---|----|
| Figure 15. Proposed charge-discharge mechanism for CoHIB as a Na-ion battery anode (a) and discharge curve profiles for CoHIB at various current densities (b). Reproduced with permission from ref. ¹²⁶ Copyright 2018, American Chemical Society. | 48 |
| Figure 16. Electrochemical properties of NiTIB (a-c) and NiDIBDT (d-f): initial charge-discharge curves at 0.1 A g ⁻¹ (a, d), cycling stability at 0.1 A g ⁻¹ (b, e) and rate performance (c, f); proposed charge-discharge mechanism for NiTIB and NiDIBDT (g). Reproduced with permission from ref. ¹²⁸ Copyright 2019, Wiley-VCH..... | 49 |
| Figure 17. Proposed charge-discharge mechanism for NiTIB as an anode material for Na-ion batteries. Reproduced with permission from ref. ¹²⁹ Copyright 2020, Wiley-VCH..... | 50 |
| Figure 18. Synthesis of NiTIB and CuTIB | 64 |
| Figure 19. ¹³ C MAS ssNMR spectrum of NiTIB (a), FTIR spectra of the as-synthesized NiTIB and CuTIB (b) and XRD patterns for the as-synthesized NiTIB and CuTIB (c). | 65 |
| Figure 20. Resonance structures of NiTIB repeating unit..... | 65 |
| Figure 21. Raman spectra of NiTIB and CuTIB measured using a laser with $\lambda = 532$ nm..... | 66 |
| Figure 22. SEM images of NiTIB and CuTIB | 69 |
| Figure 23. Direct-current polarization data for a NiTIB pellet at room temperature. Conductance, diameter and height of the cylindrical pellet are given in the figure..... | 70 |
| Figure 24. Electrochemical behavior of ball-milled CuTIB as a cathode material: charge-discharge curves for different cycles at 50 mA g ⁻¹ in 1.5-4.1 V range (a); specific discharge capacities in 1.5-4.1 V range (b); CVs for different cycles at 0.1 mV | |

s^{-1} scanning rate in 1.5-4.1 V range (c); the same set of plots for 2.0-3.8 V range (d-f).
72

Figure 25. Electrochemical behavior of ball-milled **NiTIB** as a cathode material: charge-discharge curves for different cycles at 50 mA g^{-1} in 1.5-4.1 V range (a); specific discharge capacities in 1.5-4.1 V range (b); CVs for different cycles at 0.1 mV s^{-1} scanning rate in 1.5-4.1 V range (c); the same set of plots for 2.0-3.8 V range (d-f).
73

Figure 26. Maximal specific energy achieved for **CuTIB** and **NiTIB**, calculated per material mass unit (a) and material corrected mass unit (b).75

Figure 27. X-ray photoelectron spectra regions of the cathode materials: N1s region for **CuTIB** (a) and Ni2p region for **NiTIB** (b).76

Figure 28. Electrochemical behavior of **CuTIB** in lithium-based cells in the potential range of 0.8-2.0 V vs. Li^+/Li : charge-discharge curves for different cycles at 50 mA g^{-1} (a); CVs for different cycles at 0.1 mV s^{-1} scanning rate (b); cycling stability at 50 mA g^{-1} (c).77

Figure 29. Charge-discharge curves of **NiTIB**-based electrodes in lithium-based cells with the ether-based (a) and carbonate-based (b) electrolytes at 0.1, 0.2, 0.5, 1, 2 and 5 A g^{-1} ; dependencies of charge and discharge capacities on the cycle number at varying current densities for the cells with ether-based (c) and carbonate-based (d) electrolytes. The electrodes contained 75% wt. of **NiTIB**. Decent performance was shown for diluted electrodes (40% wt. of **NiTIB**) as well.¹⁴⁷79

Figure 30. Charge-discharge curves of **NiTIB**-based electrodes in sodium (a) and potassium (b) cells at 0.1, 0.2, 0.5, 1, 2 and 5 A g^{-1} ; dependencies of charge and

| | |
|---|----|
| discharge capacities on the cycle number at varying current densities for the sodium (c) and potassium (d) cells. | 80 |
| Figure 31. Capacity vs. current density calculated per NiTIB mass for various types of cells (a) and NiTIB capacity after subtracting the contribution from Super P (b). | 81 |
| Figure 32. Rate performance of NiTIB -based electrodes with different electrode loadings and Super P contents in potassium cells: capacity vs. current per material mass (a), total electrode mass (b) and electrode area (c). | 83 |
| Figure 33. Cycling stability of NiTIB in Li-based (a), Na-based (b) and K-based (c) cells at 2 A g^{-1} | 84 |
| Figure 34. CV profiles for NiTIB in Li-based (a), Na-based (b) and K-based (c) cells, measured at scan rates of 0.2, 0.4, 0.6, 0.8 and 1 mV s^{-1} ; $\lg I $ vs. $\lg(v)$ dependencies for the CV peaks (d-f); b values of the CV peaks estimated from the linear fit (equation $\lg I = b*\lg(v) + \lg(a)$) (g-i). Ten CV cycles at 1 mV s^{-1} in the potential ranges of 0.5-2.0 V vs. M^+/M were performed prior to the measurements to eliminate irreversible processes, after which the cells were resting for 10 minutes. | 86 |
| Figure 35. Potential differences for oxidation and reduction CV peaks of NiTIB at a scan rate of 0.2 mV s^{-1} | 87 |
| Figure 36. X-ray photoelectron spectra regions of CuTIB in the initial and reduced states: Cu2p regions (a) and N1s regions (b). | 88 |
| Figure 37. Redox reaction scheme for 1,4-quinones (a) and proposed overall redox reaction scheme for NiTIB as the anode material (b). | 90 |
| Figure 38. <i>Ex situ</i> XPS profiles for NiTIB -based electrodes cycled in potassium-based cells: C1s (a) and Ni2p (b) spectra regions for the charged and discharged states. | |

Experimental data points for (a) are shown in circles, overall fit curves are shown as black lines.92

Figure 39. Intensity maps for *operando* XRD patterns of **NiTIB** during galvanostatic charge-discharge in Li-based (a), Na-based (b) and K-based (c) cells, measured with CuK α radiation. Charge-discharge profiles of the cells are plotted below.....93

Figure 40. *Ex situ* XRD patterns for discharged and pristine **NiTIB**, measured with CoK α 1 radiation ($\lambda=1.78892 \text{ \AA}$).94

Figure 41. Evolution of Raman spectra of **NiTIB** measured with an infrared laser ($\lambda = 780 \text{ nm}$) for Li-based (a, b), Na-based (c, d) and K-based (e, f) cells: Raman intensity maps and current vs. time (vs. potential) profiles (a, c, e); normalized initial spectrum compared to the spectra after the 1st and the 2nd cycles (b, d, f).96

Figure 42. UV-Vis-NIR spectra of **NiTIB** before and after chemical reduction.....98

Figure 43. Evolution of Raman spectra of **NiTIB** measured with a green laser ($\lambda = 532 \text{ nm}$) for Li-based (a, b), Na-based (c, d) and K-based (e, f) cells: Raman intensity maps and current vs. time (vs. potential) profiles (a, c, e); averaged Raman spectra for selected potential ranges during the initial discharge (b, d, f).....99

List of Tables

| | |
|---|----|
| Table 1. Elemental composition of NiTIB and CuTIB | 68 |
|---|----|

Chapter 1. Introduction

Electrochemical energy storage is one of the key topics of modern materials science. Its development is important for many aspects of technological and societal progress, such as transition from fossil fuels to sustainable energy sources, implementation of smart grids, electric vehicles, and useful portable electronics.¹⁻³

There are various types of energy storage devices, each of which has a unique set of advantages targeted for particular applications.⁴⁻⁸ However, among others, lithium-ion batteries (LIBs) have become the most widespread kind, which is also the most essential in everyday life.^{9,10} The popularity of Li-ion batteries arises from a combination of reasonably high energy and power densities, decent cycling stability and low self-discharge rate.^{1,9} Significance of this technology was highlighted by awarding the Nobel Prize in Chemistry in 2019 to M. Stanley Whittingham, John B. Goodenough and Akira Yoshino.¹¹ However, although lithium-ion batteries are in many aspects more attractive than other types of energy storage devices, they have several drawbacks that limit their applicability.

Modern lithium-ion batteries are still too expensive and bulky for electric vehicles.^{12,13} Over the past decades, performance of LIBs significantly improved, with the volumetric energy increasing from ~ 200 to $>700 \text{ W h L}^{-1}$, and their price dropped by more than an order of magnitude.¹³ However, the batteries that are able to power up an electric car (50-100 kW h) still take up to $\sim 500 \text{ L}$ of space and weigh more than half a ton.¹³ Charge-discharge rates and cycle life of modern LIBs are also limited.¹⁴⁻¹⁶ At high current rates, lithium dendrites form at graphite anode, causing severe safety issues because a risk of battery short-circuiting appears.¹⁷ Improvements of the LIB performance are becoming minor as the conventional technologies approach their

fundamental limits.¹³ Tremendous effort is currently put into developing new chemistries for fast-charging durable energy storage devices with high energy densities.¹⁸⁻²²

Furthermore, continuous growth of lithium consumption^{23, 24} raises concerns about the scarcity of its resources, which questions the sustainability of LIBs. Lithium is a rare element; its major feedstocks in the Earth's crust are concentrated only in few countries, making the industry generally dependent on the import.²⁵ In some scenarios of LIB market expansion, the lithium supply might become insufficient during the next decades.²⁶ In the short term, an even more serious issue is shortage of cobalt resources, which are important for the most widespread cathode materials.^{13, 27} If cobalt-free batteries remain underdeveloped, production of Co will have to increase up to an order of magnitude to satisfy the future demand.^{25, 28} This might lead to substantial price growth for LIBs, as well as bottlenecks in the large-scale production.²⁷ Developing cobalt-free and lithium-free batteries should help to solve these sustainability issues.

Sodium- and potassium-ion batteries (SIBs and PIBs) are among the most promising alternatives to LIBs that are more sustainable. Although sodium and potassium have smaller specific capacities than lithium (which decreases the energy density of SIBs and PIBs), they have a strong advantage of being extremely widespread and cheap elements. For both SIBs and PIBs, cheaper and lighter aluminum can be used as the anode current collector instead of copper because sodium and potassium form no alloys with Al.^{25, 29} Each type of charge carriers (Na^+ , K^+) has its own advantages. Sodium has lower atomic weight, so its specific capacity is higher. On the other hand, standard reduction potential for K is -2.93 V, which is close to that for Li (-3.04 V) and lower than for Na (-2.71 V); in propylene carbonate, the reduction potential for K is even lower than that for Li and Na.^{30, 31} Both higher capacities and lower anode potentials

help to enhance energy density of the batteries. Graphite, which is a standard anode for LIBs, can be used in PIB anodes, which is in contrast with the SIBs.³¹⁻³³ Owing to a weak Lewis acidity of potassium ions, diffusion coefficients of K^+ in electrolytes are higher than for Li^+ or Na^+ , which is beneficial for fast charge-discharge.^{34, 35} At the same time, radii of desolvated Na^+ ions are smaller compared to K^+ ions; consequently, the amplitude of volume expansion-contraction of active battery materials is expected to be smaller, potentially leading to longer cycle life of sodium-ion batteries.^{36, 37} Since each type of batteries has its unique set of advantages, it is reasonable to develop these technologies simultaneously.

Metal-organic redox-active materials can be attractive as materials for the next generation of batteries. Redox chemistry of organic-based compounds is generally weakly dependent on the nature of counter-ions that balance excessive charges upon reduction/oxidation.^{38, 39} This is in contrast to inorganic battery materials, which usually rely on cation-specific complex intercalation mechanisms.^{38, 39} Versatility of these compounds should make the development of alternative battery technologies easier since the same material can be successfully applied for lithium, sodium, potassium chemistries and other. Recently, a new family of metal-organic compounds, namely π -d conjugated coordination polymers of transition metals, have attracted attention for energy storage applications. The next chapter provides a literature review regarding this topic, as well as briefly overviews metal-ion batteries and related technologies.

Chapter 2. Literature review

2.1. Working principles and terminology for metal-ion batteries and related energy storage technologies

2.1.1. Definitions of metal-ion batteries, dual-ion batteries and pseudocapacitors

Working principle of a metal-ion battery is schematically represented in Figure 1. The device contains two electrodes, positive and negative, separated by an ionically conductive electrolyte, which is typically a liquid solution of an alkali metal salt immobilized in a porous separator. In the charged state, the negative electrode (typically referred to as anode) contains extractable metal cations, which can be inserted into the positive electrode (typically referred to as cathode) upon discharging. These reactions, driven by a difference in electrochemical potentials, induce an electric current between the electrodes. The reactions are reversible, and if an external current is applied in the opposite direction, the metal cations migrate back from the cathode to the anode, and energy is stored in this way. This type of energy storage devices, where one type of charge carriers goes back and forth between the electrodes, is sometimes called “rocking-chair batteries”.⁴⁰ For lithium-ion batteries, commercial cathode materials are exemplified by $\text{LiNi}_x\text{Mn}_y\text{Co}_z\text{O}_2$ (NMC), $\text{LiNi}_x\text{Co}_y\text{Al}_z\text{O}_2$ (NCA), LiFePO_4 or LiMn_2O_4 .⁴¹ The most popular commercial anode materials are graphite and lithium titanate (LTO).⁴¹ If alkali metals are used as the anodes, the devices should be called “metal batteries”, e.g., “lithium metal batteries”²⁰ or “sodium metal batteries”,⁴² rather than “metal-ion batteries”. Certain types of batteries with conversion-type cathodes, such as metal-air,^{21, 22, 43} metal-sulfur^{18, 44} or metal-iodine⁴⁵ batteries, are also considered

distinct types of energy storage devices and represent a family of “post-lithium-ion batteries”.

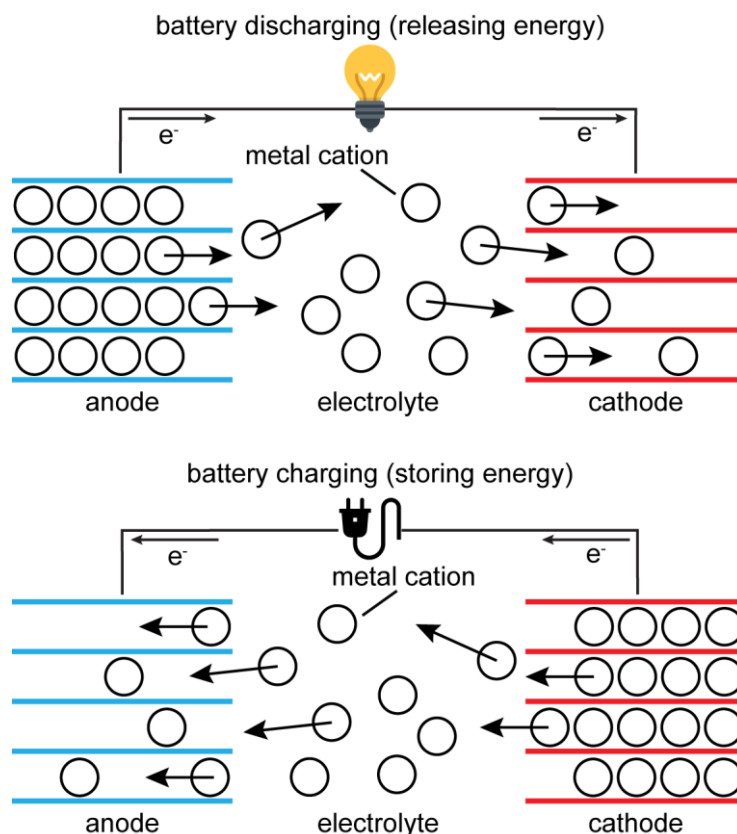


Figure 1. Schematic representation of the working principle of metal-ion batteries.

A related type of rechargeable batteries, which also utilizes reversible insertion/extraction of ions, is dual-ion batteries.^{46, 47} Upon charging of dual-ion batteries, cations from the electrolyte are inserted in the anode, while anions are inserted into the cathode. In other words, the electrolyte salt is reversibly decomposed upon charging. A classic example of a dual-ion battery is dual-graphite battery.⁴⁸ These devices have an advantage of high operating voltages (>4 V), but also have limited capacity because the amount of electrolyte (electrolyte salt) has to be much larger than for metal-ion batteries.

Another related type of energy storage technology is supercapacitors. The main types of supercapacitors are electric double layer capacitors (EDLCs) and pseudocapacitors. In EDLCs, the energy is stored via charge separation at the interfaces between electrolyte and electrodes with high surface area (typically carbon-based), where electrical double layers form.⁴⁹ For the energy storage, cations and anions from the electrolyte migrate to the electrode surfaces that become charged when a potential difference is applied externally. The charge storage mechanism is somewhat similar to dual-ion batteries, but for EDLCs its nature is non-Faradaic and occurring only near the electrode surface. Cyclic voltammograms (CVs) for EDLCs have a nearly rectangular shape, and galvanostatic charge-discharge (GCD) profiles are linear (Figure 2a, b). EDLCs can deliver high power densities ($\sim 15 \text{ kW kg}^{-1}$) and are extremely robust (stable up to millions of charge-discharge cycles), but have low energy densities ($5\text{-}10 \text{ W h kg}^{-1}$).⁵⁰

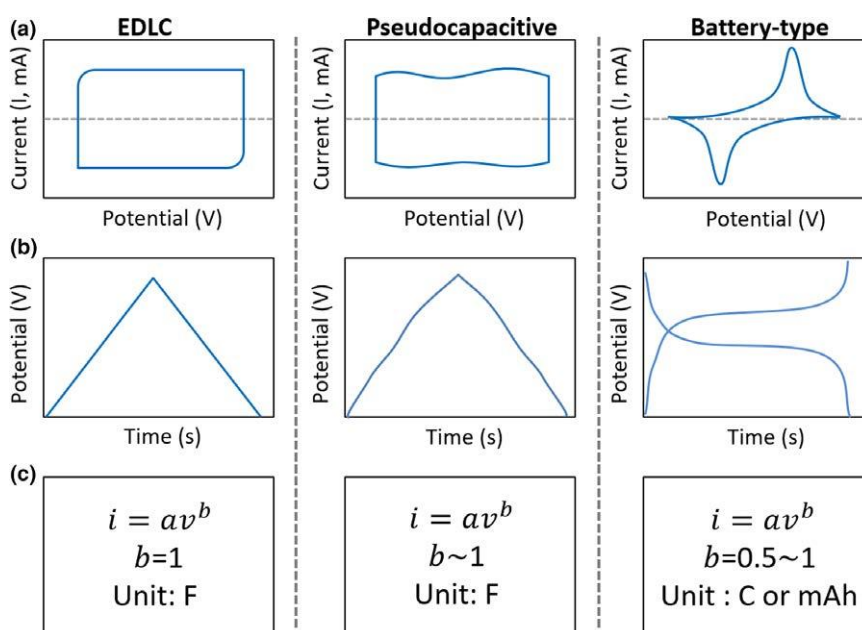


Figure 2. Features of materials for EDLCs, pseudocapacitors and batteries: CV profiles (a), GCD profiles (b) and dependencies of CV current on the scan rate (c). Reproduced with permission from ref.⁵⁰ Copyright 2019, Wiley-VCH.

The energy density is higher for pseudocapacitors, which enable redox chemistry at the electrodes. Initially, pseudocapacitance was defined as Faradaic processes taking place near the surface of electrodes.^{50,51} Classic examples are MnO_2 and RuO_2 .^{52,53} Their CV profiles are nearly rectangular, but also feature broad peaks (Figure 2a). However, this definition of pseudocapacitance became ambiguous as nanosized materials for energy storage evolved.⁵⁰ When the particle size of the battery materials is reduced to nanoscale, fraction of the charge storage sites near the surface increases, and their power density improves, which blurs the distinction between batteries and supercapacitors.^{54,55} Furthermore, some intercalation-type materials, such as Nb_2O_5 , MoO_3 or TiO_2 , were reported to have fast charge-discharge kinetics, sometimes even surpassing traditional pseudocapacitive materials.⁵⁶⁻⁵⁸ To rationalize their charge-discharge mechanisms, Dunn *et al.*^{54,59} proposed a term “intercalation pseudocapacitance”, which is intercalation of ions into the layers or tunnels of the electrode materials, during which no crystallographic phase change occurs. Pseudocapacitive mechanisms were then classified into three types (Figure 3):⁵⁹ (1) underpotential deposition, which is an infrequent phenomenon occurring when metal monolayers are electrodeposited at the surfaces of foreign metals above their reduction potentials;⁶⁰ (2) redox pseudocapacitance, which is the most common type when ions are electrochemically adsorbed at the surfaces of redox-active materials; (3) intercalation pseudocapacitance, when the intercalation of ions into the host is fast and kinetically indistinguishable from capacitance.⁵⁶

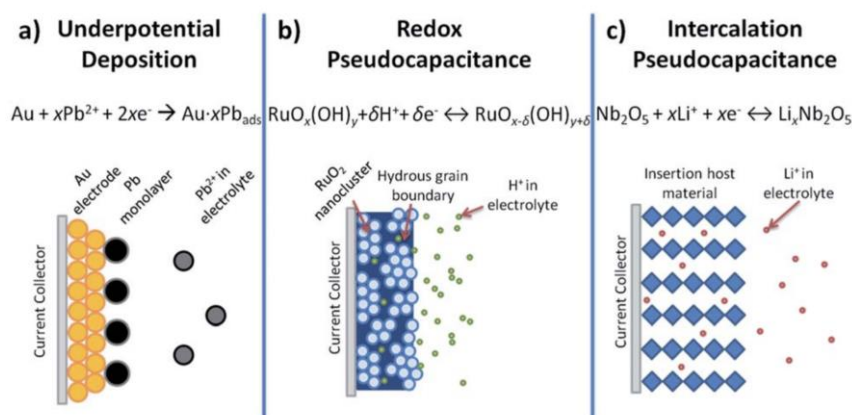


Figure 3. Types of pseudocapacitance. Reproduced with permission from ref.⁵⁹ Copyright 2014, Royal Society of Chemistry.

Dunn *et al.*⁵⁹ proposed a new definition of pseudocapacitance basing on the electrochemical features: (1) CV profiles that are nearly rectangular or featuring broad peaks with small separation on the potential axis; (2) sloping GCD profiles; (3) electrochemical impedance Nyquist plot containing a nearly vertical line with a phase angle of 90° or less (Figure 4).

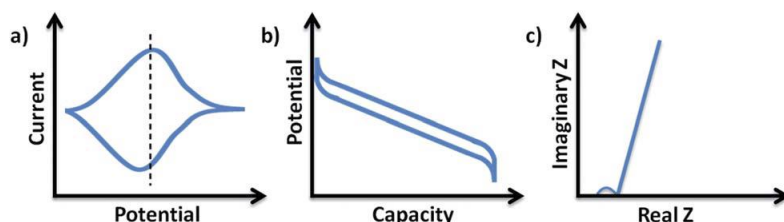


Figure 4. Electrochemical features of pseudocapacitive materials: CV profiles (a), GCD profiles (b) and Nyquist plots (c). Reproduced with permission from ref.⁵⁹ Copyright 2014, Royal Society of Chemistry.

An important experiment to understand if the redox reactions are controlled by the solid-state diffusion is measuring CV profiles at various scan rates.⁵⁰ At a given potential E , current I is considered originating from a linear combination of diffusion-controlled insertion ($k_1v^{0.5}$) and capacitive processes (k_2v) components:⁶¹

$$I(E) = k_1(E)v^{0.5} + k_2(E)v \quad (1)$$

Here v stands for the scan rate, k_1 and k_2 are potential-dependent parameters. Equation (1) can be linearized in coordinates $Iv^{-0.5}$ vs. $v^{0.5}$:

$$I(E)v^{-0.5} = k_2(E)v^{0.5} + k_1(E) \quad (2)$$

This formula is sometimes simplified to:

$$I(E) = a(E)v^{b(E)} \quad (3)$$

where a and b are potential-dependent parameters, with the b value ranging from 0.5 to 1. It is proposed that $b = 0.5$ indicates a battery-related behavior, while $b \sim 1$ is typical for capacitive or pseudocapacitive materials. However, it should be stressed that b values close to 1 were reported for nanosized materials with battery-like electrochemical features, such as obvious CV peaks with significant peak-to-peak separation ($\Delta E > 0.2$ V).^{50, 62, 63} In other words, kinetics analysis might be useful for understanding the charge-discharge mechanisms, but it cannot be used solely to determine if the materials are pseudocapacitive because the electrochemical signatures (shown in Figure 4) have to be firstly considered.⁵⁰

An interesting type of energy storage devices are hybrid supercapacitors, where one of the electrodes stores charge via a battery-type Faradaic process, while the second electrode relies on the capacitive mechanism.⁶ The concept of these devices is to increase the energy density by using battery-type electrodes while retaining high power densities of the supercapacitors. In terms of the specific energy, power and cycling stability, hybrid supercapacitors occupy a middle ground between metal-ion batteries and classic supercapacitors.⁶⁴

2.1.2. Key characteristics of energy storage devices

Important characteristics of energy storage devices are the amount of energy that can be stored per mass of volume unit, charge-discharge rate (or power, which is a related parameter) and cycling stability. If a device operates in a galvanostatic mode, the energy W that is retrieved upon discharging can be calculated as follows:

$$W = \int_0^Q V(q) dq = I \int_0^\tau V(t) dt \quad (4)$$

where I is current, τ is discharge time, Q is capacity, i.e., charge that is transferred through an external circuit, and V is the voltage that is generally dependent on the state of charge and is the potential difference between the positive and the negative electrodes:

$$V(q) = E^c(q) - E^a(q) \quad (5)$$

Equation (4) may be expressed in terms of average voltage V_{avg} :

$$W = QV_{avg} \quad (6)$$

$$V_{avg} = \frac{\int_0^Q V(q) dq}{Q} = \frac{\int_0^Q E^c(q) dq}{Q} - \frac{\int_0^Q E^a(q) dq}{Q} = E_{avg}^c - E_{avg}^a \quad (7)$$

For the cyclic voltammetry experiments, W can be calculated as follows:

$$W = \frac{1}{2\nu(V_2 - V_1)} \oint_{V_1}^{V_2} I(V) dV \quad (8)$$

where V_2 and V_1 are maximal and minimal operating voltages, ν is scan rate. This formula, however, should be applied when charge and discharge capacities of the material are close, i.e., no obvious irreversible side reactions occur.

For supercapacitors, a typically reported value is capacitance C , which reflects what charge (capacity) ΔQ is stored under a given voltage change:

$$C = \frac{\Delta Q}{\Delta V} \quad (9)$$

The stored energy for supercapacitors can be calculated from the capacitance as follows:

$$W = \frac{CV^2}{2} \quad (10)$$

Power P is typically reported as the ratio between the energy and the discharge time:

$$P = \frac{W}{t} \quad (11)$$

This formula reflects the average power of a device. It should be noted, however, that if the voltage is dependent on the state of charge, the power is also not constant. At each moment of time, power can be expressed as a product of voltage and current.

Cycling stability for batteries and supercapacitors is typically studied using continuous cycling in the GCD mode. Capacity retention (in percent) is typically reported after a certain number of charge-discharge cycles. If the capacity decays linearly, capacity decay per cycle (in percent, mA h g⁻¹, etc.) can be reported.

2.1.3. Requirements for the next generation of energy storage materials

For the new generation of energy storage devices, it is desirable to approach high specific energy and power along with excellent cycling stability and safety. Two ways to improve the energy density are to increase the voltage and to increase the capacity (or capacitance). To approach high voltages, a device should combine a positive

electrode with high reduction potential and a negative electrode with a low oxidation potential. To increase the capacity, cathode and anode materials must have high concentrations of redox-active sites. Theoretical specific capacity can be calculated as follows:

$$Q_{theor} = \frac{nF}{M} \quad (12)$$

where n is the number of electrons that can be donated/accepted per formula unit of the material, M is molar mass of the material formula unit, F is Faraday constant (26 801 mA h mol⁻¹).

To achieve high power densities, high charge transfer rates and fast ion diffusion are required. This implies high electronic and ionic conductivities within the electrodes, as well as high ionic conductivity of the electrolyte.⁶⁵ Using conductive electrode materials with pseudocapacitive charge-discharge mechanisms is beneficial for designing energy storage devices with high power.⁶⁵

To ensure decent cycling stability, several conditions have to be fulfilled:

- Charge-discharge processes (either Faradaic or non-Faradaic) must be highly reversible.
- Solubility of the electrode materials and their reduction/oxidation products in the electrolytes should be negligible, so no shuttling of redox-active species to counter-electrodes is occurring.⁶⁶
- Volumetric changes upon charging-discharging should be small, so that the structural integrity of the electrodes can be retained, avoiding particle fracturing and delamination. It should be noted, however, that even for materials with high intrinsic volume expansion, e.g., silicon, structural stability of the electrodes can

be approached by nanoengineering, tuning the binder or solid electrolyte interphase (SEI) structure.^{37, 67-70}

- No extensive continuous decomposition of the electrolyte should take place at the electrodes upon charging-discharging. This condition becomes increasingly difficult to fulfill (especially at elevated temperatures^{71, 72}) when electrode potentials are high (>4.5 V vs. Li^+/Li) or low (<0.5 V vs. Li^+/Li), because liquid-state electrolytes typically start to decompose. One of the main approaches to overcome this issue is to create stable SEI layers that will prevent continuous parasitic reactions.⁷³⁻⁷⁶ The second option is to use solid-state electrolytes, which, however, have other issues, such as high interfacial resistance or low conductivity.⁷⁷⁻⁷⁹ The third option is to sacrifice the energy density by, for example, using anode materials with higher redox potentials, such as LTO for Li-ion batteries.⁸⁰ This strategy is useful not only for improving the stability, but also for making fast charging of the batteries safe by eliminating the possibility of metal dendrite deposition.¹⁷

Safety of energy storage devices is in a certain way conflicting with the requirements for higher energy and power. In terms of energy, the best anode materials are alkali metals because they have the highest specific capacities and the lowest redox potentials.^{20, 42} These anodes, however, are highly reactive and prone to the dendrite growth. Other anodes with low redox potentials, such as graphite, are also reactive in metalated states, and the dendrites might form at their surfaces upon fast charging-discharging.¹⁷ High-voltage cathode materials also tend to have safety issues, which are related to factors such as electrolyte decomposition or instability of the charged states.^{72,}

81, 82

Some of the 2D structures can be considered as metal-organic analogs of graphene, owing to their extended conjugation within the *ab* plane.^{104, 107} Many π -d conjugated coordination polymers have high electron conductivity,¹⁰⁷ in some cases surpassing 1000 S cm^{-1} (in films).^{92, 96} Charge transport in these polymers occurs mainly within the π -d conjugated planes.¹⁰⁷

An important feature of these structures is reversible redox activity of the ligands. Typically, structures with hydroquinoid (2⁻), semiquinoid (1⁻) and quinoid (0) motifs can be stable (Figure 6).¹⁰⁷ The ligands are usually oxidized during synthesis, which leads to deprotonation of amines, catecholates or dithiols.¹⁰⁷ Notably, partial oxidation might introduce charge carriers into the metal-organic frameworks, which results in the conductivity increase.¹⁰⁷

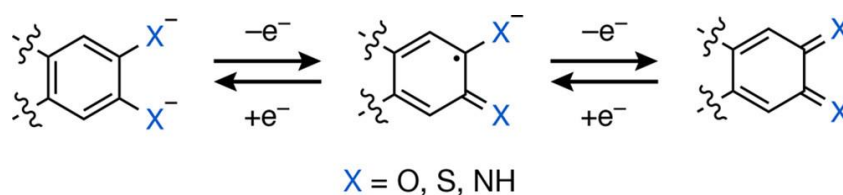


Figure 6. Hydroquinoid (2⁻), semiquinoid (1⁻) and quinoid (0) motifs of ligands in π -d conjugated coordination polymers. Reproduced from ref.¹⁰⁷ under CC BY license.

Copyright 2020, American Chemical Society.

Coordination polymers with π -d conjugation combine several features that are attractive for energy storage purposes. Their frameworks remain stable upon reduction or oxidation. High specific capacities might be approached for these structures, especially if low-molecular ligands with multiple functional groups are used. High electronic conductivity of many of these polymers should be helpful for developing high-power devices on their basis. The next section reviews papers that reported π -d conjugated coordination polymers in supercapacitors and batteries.

2.3. Applications of π -d conjugated coordination polymers as active materials in energy storage devices

2.3.1. Applications in supercapacitors

The first report dedicated to using π -d conjugated MOFs in electrical double layer capacitors was made by Dincă *et al.* in 2016.¹⁰⁸ The authors used neat **NiHITP** (Ni_3HITP_2 , HITP = 2,3,6,7,10,11-hexaiminotriphenylene, Figure 7a), a material with high electron conductivity ($>50 \text{ S cm}^{-1}$), in EDLCs with $[\text{Et}_4\text{N}][\text{BF}_4^-]$ /acetonitrile electrolyte. Predominant double-layer capacitance mechanism originated from a large specific surface area ($630 \text{ m}^2 \text{ g}^{-1}$), and large pore size (Figure 7a, b) enabled the diffusion of Et_4N^+ and BF_4^- ions and their solvates with acetonitrile. The electrodes demonstrated high gravimetric and areal capacitances of 111 F g^{-1} and $18 \mu\text{F cm}^{-2}$, respectively. The cycling stability was also excellent, with 90% capacitance retention after 10 000 cycles.

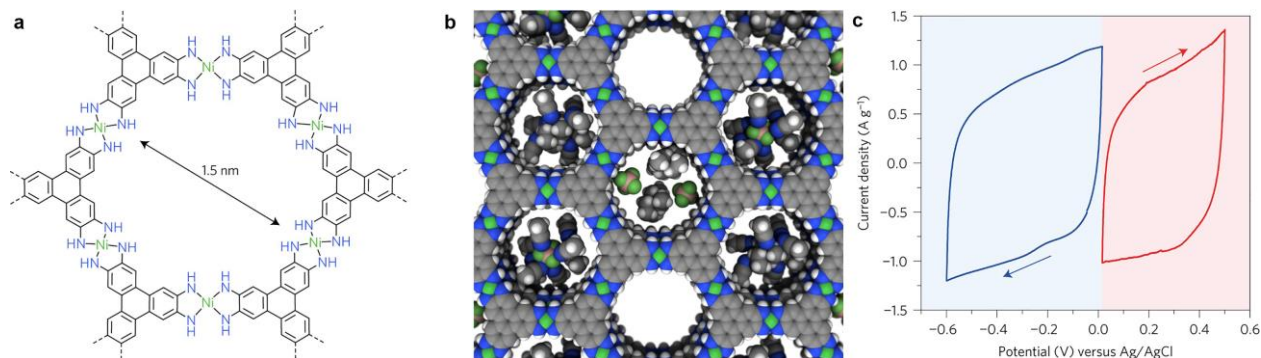


Figure 7. Structure of **NiHITP** (a), relative size of **NiHITP** pores, Et_4N^+ , BF_4^- ions and acetonitrile from the electrolyte (b) and cyclic voltammograms of **NiHITP** measured at a scan rate of 10 mV s^{-1} (c). Reproduced with permission from ref.¹⁰⁸ Copyright 2017, Springer Nature.

Later, Xu and co-authors¹⁰⁹ reported a catecholate-based 2D MOF **CuHHTP** ($\text{Cu}_3(\text{HHTP})_2$, HHTP = 2,3,6,7,10,11-hexahydroxytriphenylene) with a nanowire morphology for direct use in solid-state supercapacitors. Because of the high porosity and

electronic conductivity, high specific capacitance of 202 F g^{-1} was achieved at a current density of 0.5 A g^{-1} . A symmetric solid-state supercapacitor delivered an areal capacitance of $22 \text{ } \mu\text{F cm}^{-2}$ and had decent high-rate capabilities.

In 2018, Bao *et al.*¹¹⁰ reported a further increase of the areal and volumetric capacitance by introducing MOFs with a high density of redox-active centers, namely **CuHIB** and **NiHIB** (HIB = hexaiminobenzene, Figure 8a, b). With 1M KOH solution in water as the electrolyte, both MOFs exhibited obvious redox activity (Figure 8c, d), and the charge storage mechanism was mainly pseudocapacitance with a relatively small contribution from electric double-layer capacitance. Large gravimetric capacitances of 215 and 420 F g^{-1} were reported for **CuHIB** and **NiHIB**, respectively. Moreover, pellets of **NiHIB** with a thickness of 50 microns demonstrated exceptionally high gravimetric and volumetric capacitances of 427 F g^{-1} and 760 F cm^{-3} , respectively. Even when the electrode thickness was 0.36 mm, the areal capacitance still approached 20 F cm^{-2} . Excellent cycling stability was also shown, with 90% capacitance retention after 12 000 cycles.

Lately, Bao *et al.*¹¹¹ studied the charge storage mechanism of **NiHIB** in supercapacitors using a combination of *operando* Raman spectroscopy, *operando* XAS experiments and XPS, as well as electrochemical methods. *Operando* Raman spectroscopy revealed changes in the region from 1400 to 1600 cm^{-1} upon charging-discharging, which indicates redox activity of the HIB ligands. However, no in-depth analysis of these Raman spectra changes was carried out. From XAS and XPS studies, it was concluded that nickel remained in divalent state during the charge-discharge. The authors studied electrochemical properties of **NiHIB** using electrolytes with charge carriers having different size, such as Li^+ , Na^+ , K^+ , tetraethylammonium and

tetrahexylammonium. The material behaved similarly with all electrolyte compositions, from which it was concluded that the charge storage was predominantly surface-controlled pseudocapacitance rather than bulk pseudocapacitance. It was also shown that the charge-discharge mechanism was pH-dependent. Particularly, the redox features of **NiHIB** were present only with strong alkaline solutions (such as 0.5–1 M KOH), while rectangular-shaped CV profiles were observed with neutral or mildly basic electrolytes, e.g., KF, KBr or KHCOO solutions.

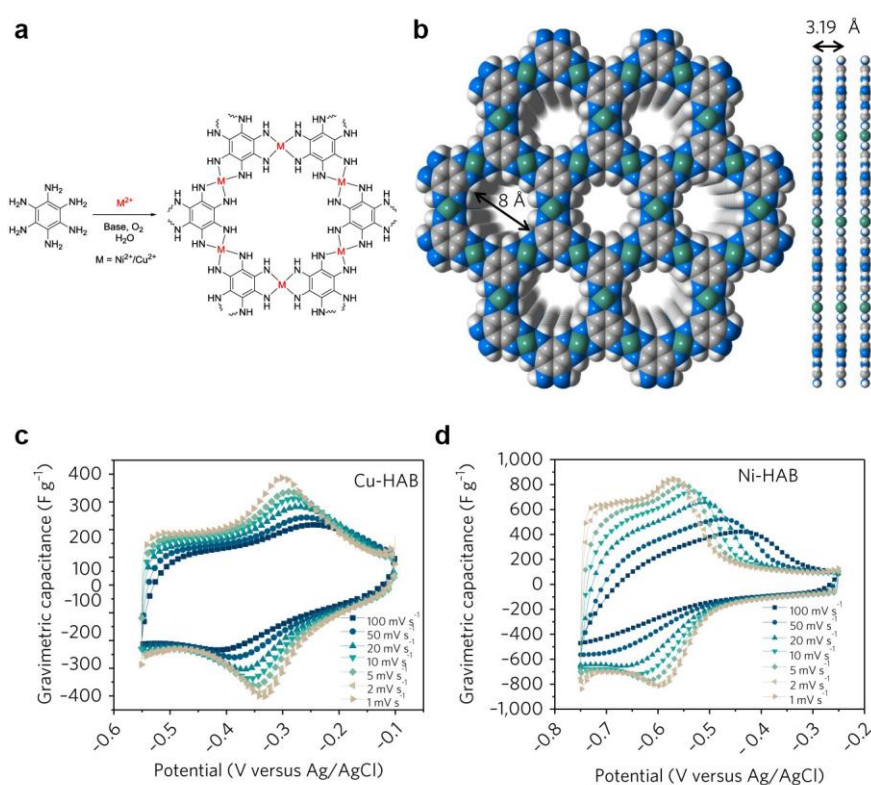


Figure 8. Synthetic scheme for **CuHIB** and **NiHIB** (a), structure of **CuHIB** (b) and CV profiles of **CuHIB** (c) and **NiHIB** (d) measured at different scan rates. Reproduced with permission from ref.¹¹⁰ Copyright 2018, Springer Nature.

A different charge storage mechanism was observed for **NiBHT** (Ni_3BHT , BHT = benzenehexathiolate, Figure 9a) with $\text{LiPF}_6/\text{acetonitrile}$ as the electrolyte, as recently

reported by Dincă *et al.*¹¹² In contrast to **NiHIB**, the specific capacitance of **NiBHT** dropped from 227 F g⁻¹ to ~30 F g⁻¹ at the scan rate of 5 mV s⁻¹ when LiPF₆ was changed to NEt₄PF₆, NEt₄BF₄ or NBu₄BF₄ (Figure 9b, c). Such behavior is an indicator of intercalation pseudocapacitance for Li⁺ ions and surface pseudocapacitance for the large cations, which was relatively small because of the limited specific surface area of **NiBHT** (~25 m² g⁻¹). The intercalation mechanism for Li⁺ ions was confirmed using ⁷Li ssNMR and powder X-ray diffraction, and it was shown that Li⁺ were desolvated prior to the intercalation. According to XAS data, the BHT ligands were redox-active, while nickel remained in the +2 state during the charge-discharge processes.

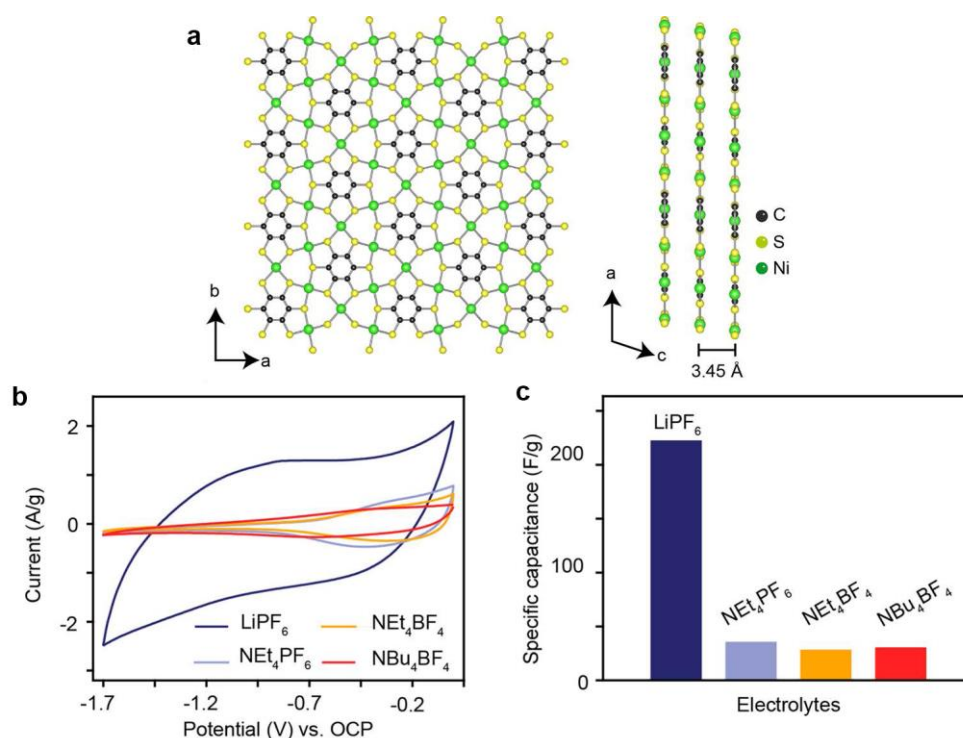


Figure 9. Simulated structure of **NiBHT** (a), CV profiles of **NiBHT** measured at the scan rate of 5 mV s⁻¹ with 1M LiPF₆, NEt₄PF₆, NEt₄BF₄ or NBu₄BF₄ solutions in acetonitrile as the electrolytes (b) and gravimetric capacitances for different electrolytes (b). Reproduced with permission from ref.¹¹² Copyright 2021, American Chemical

Society.

Regarding other coordination polymers, a redox-active conductive metal-organic framework **CuDBC**, which is derived from dibenzo[g,p]chrysene-2,3,6,7,10,11,14,15-octaol (8OH-DBC), has recently been reported to have a high gravimetric capacitance (up to 479 F g^{-1} at 0.2 A g^{-1}).¹¹³ In symmetrical solid-state supercapacitors, **CuDBC** delivered high areal and volumetric capacitances of 879 mF cm^{-2} and 22 F cm^{-3} , respectively.

2.3.2. Applications in cathodes for metal-ion batteries and dual-ion batteries

The first example of using a π -d conjugation as a cathode material for batteries was demonstrated in 2018 by Nishihara *et al.*,¹¹⁴ who used bis(diimino)nickel framework **NiHIB** in lithium-based batteries. In the voltage range of 2.0–4.5 V vs Li^+/Li , the material showed a specific capacity of 155 mA h g^{-1} at a current rate of 10 mA g^{-1} , which corresponded to a specific energy density of 434 W h kg^{-1} . At a higher current rate of 500 mA g^{-1} , the capacity dropped sharply to $\sim 55 \text{ mA h g}^{-1}$. The capacity was relatively stable over 300 cycles at 250 mA g^{-1} . The charge-discharge curves were sloping with some broad redox features appearing at $>3 \text{ V vs. Li}^+/\text{Li}$. Using X-ray photoelectron spectroscopy (XPS), the authors showed that Li^+ ions acted as charge-carriers at lower potentials, accompanied by **NiHIB** reduction (n-doping), and PF_6^- anions were inserted into the structure at higher potentials, accompanied by **NiHIB** oxidation (p-doping) (Figure 10). In other words, the polymer behaved as a cathode material for rocking-chair batteries or for dual-ion batteries, depending on the potential range.

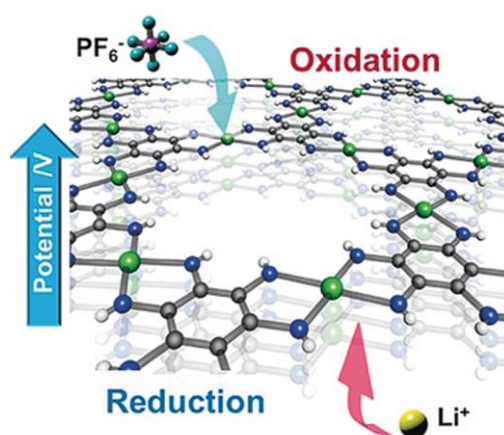


Figure 10. Schematic representation of charge-discharge mechanisms of **NiHIB** in Li-based batteries. Reproduced with permission from ref.¹¹⁴ Copyright 2018, Wiley-VCH.

In a recent paper, Nishihara *et al.*¹¹⁵ studied a series of similar MOFs where nickel ions in **NiHIB** were partially or totally replaced by cobalt ions. The CV profiles of all materials had broad features that were slightly different for **NiHIB**, **CoHIB** and mixed **Co_xNi_{1-x}HIB** compositions (Figure 11a). In the potential range of 1.0–3.5 V vs Li⁺/Li, the charge-discharge curves were sloping, with the capacity approaching 248 mA h g⁻¹ at 100 mA g⁻¹ for **Co_{0.56}Ni_{0.44}HIB** (Figure 11d). The authors suggested that for all materials Li⁺ ions were inserted at lower potentials and PF₆⁻ ions were inserted at higher potentials. However, no detailed mechanistic studies were carried out. According to *ex situ* powder XRD, the authors observed negligible changes of the lattice parameters after oxidation.

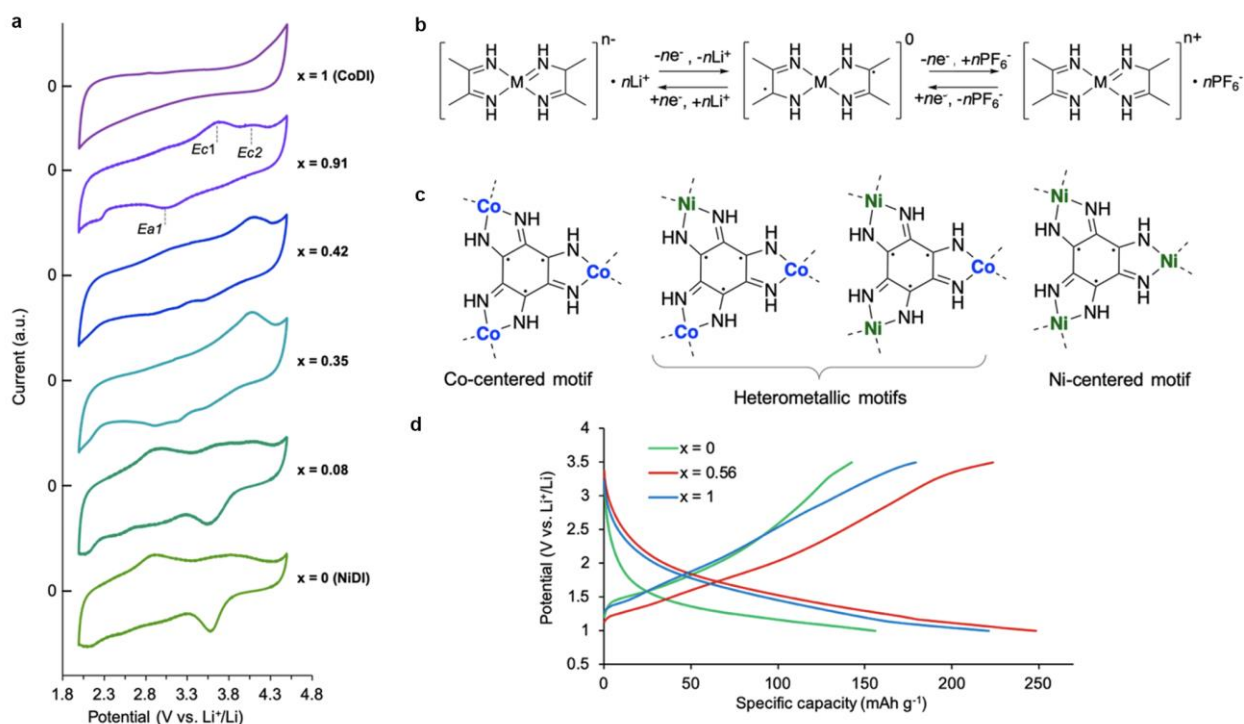


Figure 11. CV profiles of $\text{Co}_x\text{Ni}_{1-x}\text{HIB}$ at the potential scan rate of 0.5 mV s^{-1} obtained after ten pre-conditioning cycles (a); proposed charge-discharge mechanisms (b); structures of different motifs (c); charge-discharge curves of $\text{Co}_x\text{Ni}_{1-x}\text{HIB}$ at 100 mA g^{-1} . Reproduced with permission from ref.¹¹⁵ Copyright 2020, American Chemical Society.

A two-dimensional copper-benzoquinoid MOF **CuTHQ** was tested as a cathode material for lithium-based batteries by Liu *et al.*¹¹⁶ The capacity for this material approached 387 mA h g^{-1} in the potential range of 1.2–4.0 V vs Li^+/Li , corresponding to the specific energy density of 775 W h kg^{-1} . Using *ex situ* XPS, FTIR, ESR and XAS techniques, the authors demonstrated that the redox process involved a reversible two-electron reduction of ligands (n-doping) and an additional oxidation of Cu(I) to Cu(II) at the potentials above 3 V vs. Li^+/Li (p-doping) (Figure 12). As reported by another group of researchers, Wang *et al.*,¹¹⁷ the same material after particle exfoliation could

deliver a stable capacity of $\sim 120 \text{ mA h g}^{-1}$ in the potential range of 1.3–2.6 V vs Li^+/Li , and the capacities approached 300 and 400 mA h g^{-1} when the potential ranges of 1.3–3.3 and 1.3–4.0 V vs Li^+/Li were selected, respectively. However, the cycling stability was inferior when the wide potential ranges were applied.

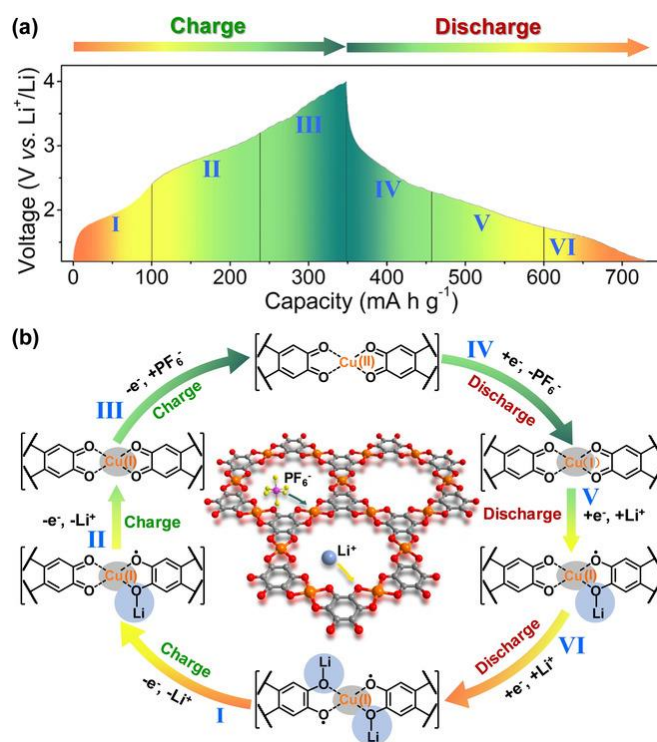


Figure 12. Charge-discharge voltage profiles of (a) and proposed charge-discharge mechanism of **CuTHQ** (b). Reproduced with permission from ref.¹¹⁶ Copyright 2020, Wiley-VCH.

A similar catechol-based MOF **CuHHTP** was tested as a cathode material for aqueous Zn-ion batteries (Figure 13).¹¹⁸ In the potential range of 0.5–1.3 V vs. Zn^{2+}/Zn , the capacity reached 228 mA h g^{-1} at 50 mA g^{-1} , and 124 mA h g^{-1} retained at 4 A g^{-1} . The capacity retention was 75% after 500 cycles. Insertion of Zn^{2+} ions into the structure upon discharging was confirmed using XPS and EDX mapping. XPS data

and DFT calculations suggested that both Cu^{2+} ions and the ligands were undergoing reversible reduction upon discharging.

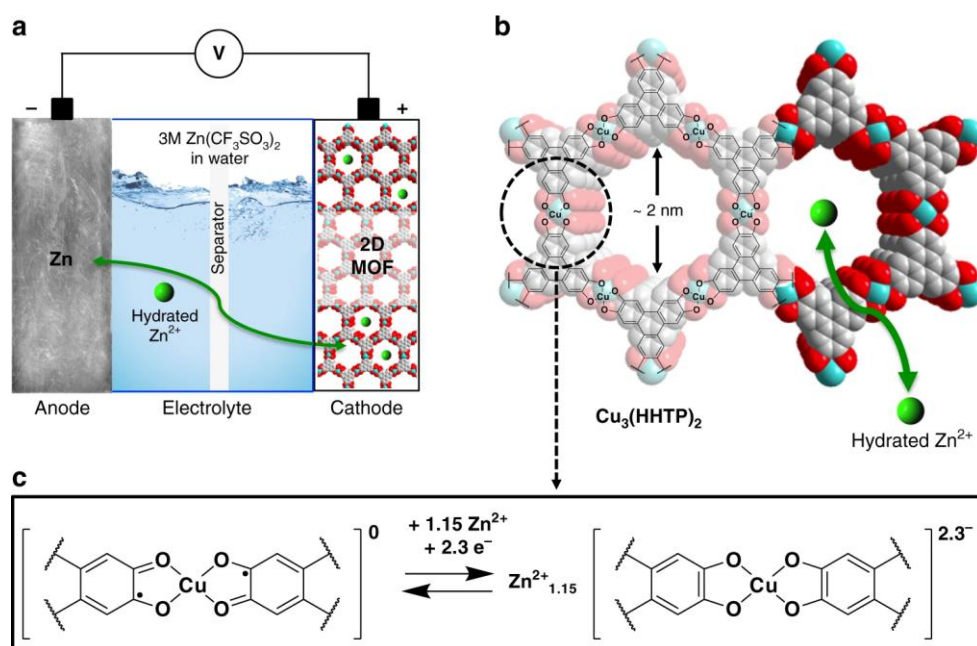


Figure 13. Scheme of a Zn-ion battery with **CuHHTP** (a), structure of **CuHHTP** (b) and proposed charge-discharge mechanism (c). Reproduced from ref.¹¹⁸ under CC BY license. Copyright 2019, The Authors.

Several other catecholate-based MOFs were tested as cathode materials for Li-based batteries. Chen *et al.*¹¹⁹ reported that a Cu-based coordination polymer derived from dicyano-2,3,5,6-tetrahydroxybenzene could reach the capacity of 268 mA h g^{-1} at 30 mA g^{-1} in the potential range of 1.5–3.5 V vs Li^+/Li . Unfortunately, it possessed inferior cycling stability due to the material dissolution. Both copper ions and organic moieties were redox-active according to *ex situ* XPS and FTIR spectroscopy. Long *et al.*¹²⁰ showed that an iron-based MOF derived from 2,5-dichloro-3,6-dihydroxybenzoquinone delivered the capacity of up to 195 mA h g^{-1} at 20 mA g^{-1} in the potential range of 1.8–4.2 V vs Li^+/Li , which corresponded to the energy density of 533 W h kg^{-1} . The capacity was relatively stable over 50 cycles. Similar electrochemical performance was

achieved in sodium- and potassium-based batteries. Basing on Mössbauer and FTIR spectroscopy data, the authors concluded that both iron cations and the ligands were redox-active.

Another coordination polymer, nickel tetrathiooxalate **NiTTO**, was investigated as a cathode material for non-aqueous sodium-based batteries.¹²¹ Transition metal polymers based on tetrathiooxalate ($C_2S_4^{2-}$) or ethenetetrathiolate ($C_2S_4^{4-}$) ligands are compounds with high electrical conductivity ($\sim 1-100 \text{ S cm}^{-1}$) that have been known for decades.¹²²⁻¹²⁴ In the potential range of 1.2-3.2 V vs. Na^+/Na , the capacity approached 140 mA h g^{-1} at 0.1 A g^{-1} and changed only slightly when the current density increased to 5 A g^{-1} . Stability of the material was demonstrated over 100 cycles at 0.1 A g^{-1} (the capacity retention was 83%). Charge-discharge curves had two plateaus located at ~ 2.5 and $\sim 1.6 \text{ V}$ vs. Na^+/Na , which agreed with the cyclic voltammetry data showing two groups of peaks (Figure 14b, c). From the electrochemical data, XPS and FTIR it was concluded that $C_2S_4^{2-}$ species were reversibly reduced to $C_2S_4^{4-}$, forming sodium-nickel ethenetetrathiolate **Na₂NiETT** (Figure 14a).

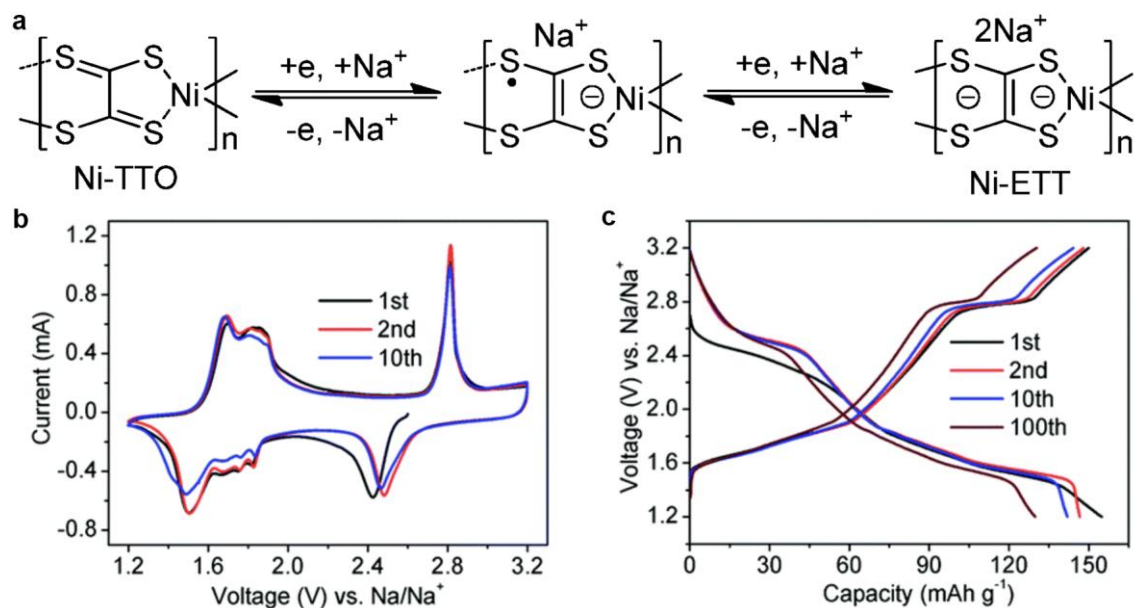


Figure 14. Proposed charge-discharge mechanism of **NiTTO** in Na-based cells (a), CV profiles of **NiTTO** measured at 0.5 mV s^{-1} for different cycle numbers (b) and charge-discharge profiles of **NiTTO** at 0.1 A g^{-1} for different cycle numbers (c). Reproduced with permission from ref.¹²¹ Copyright 2019, Royal Society of Chemistry.

Lately, a benzenehexathiolate-based conductive MOF **CuBHT** has been proposed as a cathode material for lithium-ion batteries.¹²⁵ The material was electrochemically active in a similar potential range to **NiTTO** ($\sim 1.5\text{-}2.5 \text{ V vs. Li}^+/\text{Li}$). Its reversible specific capacity at 0.1 and 2 A g^{-1} was 174 and 100 mA h g^{-1} , respectively. At a low current density of 50 mA g^{-1} , the capacity reached 202 and 189 mA h g^{-1} when the electrode loading was 2.52 and 3.06 mg cm^{-2} , respectively. When the content of **CuBHT** in the electrodes was increased from 70% to 90% wt., the discharge capacity was still $\sim 80 \text{ mA h g}^{-1}$ at 1 A g^{-1} , owing to high electron conductivity of the active material. **CuBHT** also showed decent cycling stability, with 75% capacity retention after 500 cycles at 0.3 A g^{-1} . According to *ex situ* XPS, the redox-active moieties of the

MOF were ligands, while the oxidation state of copper(II) retained during the charge-discharge processes.

2.3.3. Applications in anodes for metal-ion batteries

A hexaaminobenzene-derived conductive 2D MOF **CoHIB** was tested by Bao *et al.*¹²⁶ as an anode material for sodium-ion batteries (Figure 15). In a potential range of 0.5-3.0 V vs. Na⁺/Na, a high reversible capacity of 291 mA h g⁻¹ was shown at 50 mA g⁻¹. Moreover, the capacities were still 214 and 152 mA h g⁻¹ at 2 and 12 A g⁻¹, respectively (charge/discharge within ~7 minutes and ~45 seconds, respectively). Remarkably, **CoHIB** content in the electrodes was 90% wt. The conductive MOF also showed decent stability over >100 cycles at 4 A g⁻¹. Excellent high-rate capabilities of the material originated from its electrical conductivity (1.57 S cm⁻¹). According to the authors, the charge-discharge mechanism of **CoHIB** involved a reversible three-electron reduction of the ligands. Further sodiation (<0.5 V) led to irreversible destruction of the material, which likely involved reduction of Co²⁺.

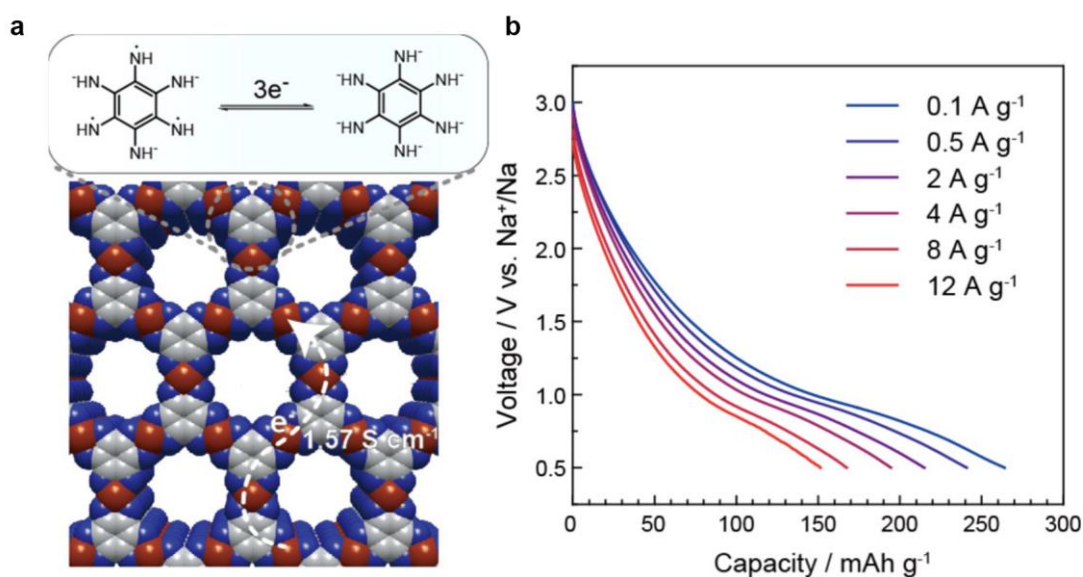


Figure 15. Proposed charge-discharge mechanism for **CoHIB** as a Na-ion battery anode (a) and discharge curve profiles for **CoHIB** at various current densities (b). Reproduced with permission from ref.¹²⁶ Copyright 2018, American Chemical Society.

A similar structure, **NiHIB**, has been recently tested as an anode material for sodium-ion batteries.¹²⁷ The electrochemical behavior of this material was similar to **CoHIB**. In a voltage range of 0.5-3.0 V vs. Na⁺/Na, it delivered capacities of ~300 and ~100 mA h g⁻¹ at 0.05 and 10 A g⁻¹, respectively, and had a decent capacity retention of 84% after 500 cycles at 1 A g⁻¹. Broadening the voltage range to 0.01-3.0 V vs. Na⁺/Na led to a capacity increase up to ~450 mA h g⁻¹ at 50 mA g⁻¹, but the high-rate performance and cycling stability significantly deteriorated at the same time. According to XPS, only the ligands were electrochemically active at the potentials above 0.5 V vs. Na⁺/Na, while Ni²⁺ reduction took place at lower potentials.

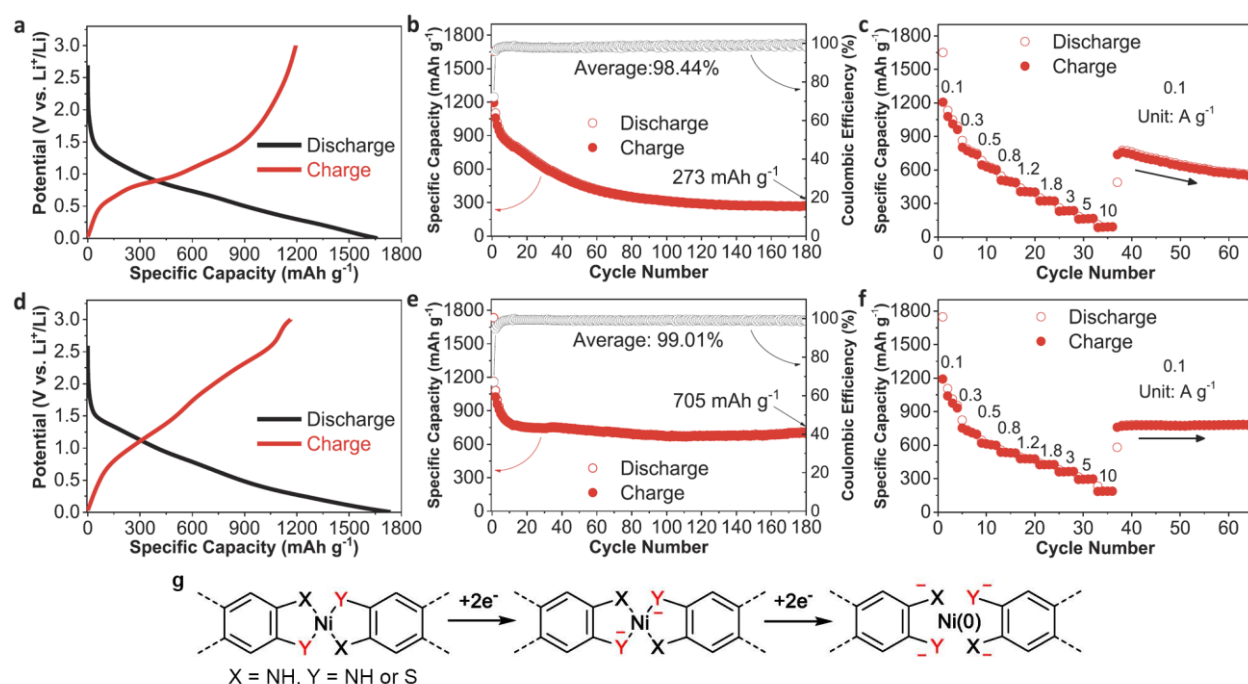


Figure 16. Electrochemical properties of **NiTIB** (a-c) and **NiDIBDT** (d-f): initial charge-discharge curves at 0.1 A g^{-1} (a, d), cycling stability at 0.1 A g^{-1} (b, e) and rate performance (c, f); proposed charge-discharge mechanism for **NiTIB** and **NiDIBDT** (g). Reproduced with permission from ref.¹²⁸ Copyright 2019, Wiley-VCH.

Xie *et al.*¹²⁸ reported one-dimensional nickel-based coordination polymers, **NiTIB** ($\text{Ni}[\text{C}_6\text{H}_2(\text{NH})_4]$, TIB = 1,2,4,5-tetraaminobenzene) and **NiDIBDT** ($\text{Ni}[\text{C}_6\text{H}_2(\text{NH})_2\text{S}_2]$, DIBDT = 1,4-diiminobenzene-2,5-dithiolate), as anode materials for lithium-ion batteries. In the potential range of 0.005-3.0 V vs. Li^+/Li , large reversible capacities were shown at 0.1 A g^{-1} (1195 mA h g^{-1} for **NiTIB**, 1164 mA h g^{-1} for **NiDIBDT**, Figure 16a, d). For **NiTIB**, the capacity was unstable, decreasing to 273 mA h g^{-1} after 180 cycles, while the capacity for **NiDIBDT** stabilized at $\sim 700 \text{ mA h g}^{-1}$ (Figure 16b, e). The authors proposed that the improved stability was associated with stronger Ni-S bonding. **NiDIBDT** also showed better rate capabilities, delivering 292 and 185 mA h g^{-1} at 5 and 10 A g^{-1} , respectively. The authors supposed that the charge-

discharge mechanisms involved two-electron reduction of ligands and reduction of Ni²⁺ to Ni⁰ (Figure 16g). However, no studies were performed to support this hypothesis. It should be stressed that theoretical capacities for the four-electron reduction of the repeating units are 556 and 472 mA h g⁻¹ for **NiTIB** and **NiDIBDT**, respectively, which are much smaller than the reported experimental values.

NiTIB was later studied as an anode material for Na-ion batteries in the voltage range of 0.01-2.5 V vs. Na⁺/Na.¹²⁹ The reported capacity at 0.1 A g⁻¹ reached 420 mA h g⁻¹ after subtracting contribution from Super P, and the capacity at 10 A g⁻¹ was up to 330 mA h g⁻¹. The material was stable over 90 cycles at 0.1 A g⁻¹ and over 400 cycles at 1 A g⁻¹. Basing on the experimental specific capacity, the authors suggested that the charge-discharge mechanism of **NiTIB** included two-electron reduction of ligands and reduction of Ni(II) to Ni(I) (Figure 17).

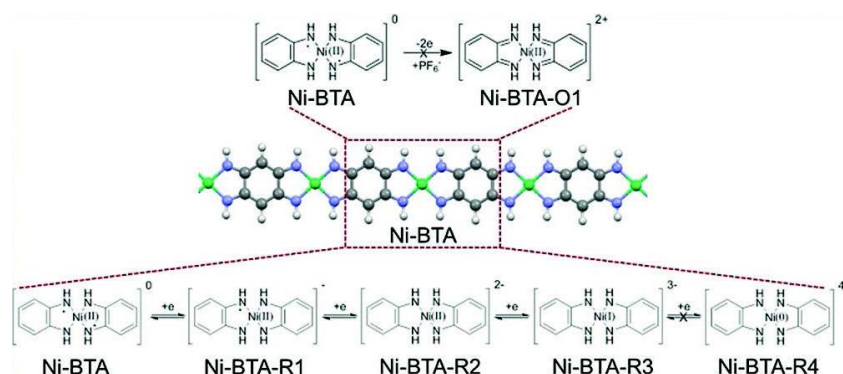


Figure 17. Proposed charge-discharge mechanism for **NiTIB** as an anode material for Na-ion batteries. Reproduced with permission from ref.¹²⁹ Copyright 2020, Wiley-

VCH.

However, data supporting the hypothesis about the nickel transition were ambiguous. According to XPS, oxidation state of nickel remained as +2 in the sodiated state. Almost no changes in EXAFS were observed as well. Some minor shifts in Ni K-

edge XANES were reported, but it is challenging to say if they were certainly caused by Ni(I) formation. Surprisingly, only minor changes in FTIR spectra or XRD patterns were observed after the sodiation, which is untypical for the cases when major structural rearrangements take place. Other experimental evidence is hardly useful for determining the nickel oxidation state in the sodiated **NiTIB**:

- ESR signal increased for the discharged state, but it was unclear which radical species caused this increase.
- The authors indicated that when wet discharged electrodes were exposed in air, white smoke was immediately observed; although the authors speculated that the smoke was caused by oxidation of highly reactive Ni(I) species, this experiment provides little information about the chemical structure.
- The reduced **NiTIB** had catalytic activity in Negishi coupling reactions, which are typically performed using Ni(0)-based catalysts and are believed to involve Ni(I)-based intermediates.¹³⁰ At the same time, no catalysis occurred for the pristine or charged **NiTIB**. However, as in the case with the “smoking” experiment, conclusions about the nature and content of catalytically active species are hard to make. Even if the catalytically active species were Ni(I), it is unclear if they were present in sodiated **NiTIB** initially or if they formed after introducing the material to the reaction mixture, which contained substances such as zinc chloride, phenylmagnesium chloride and *p*-iodoanisole.

Chapter 3. Research objectives

As follows from the literature review, although coordination polymers with π -d conjugation show promising features as materials for energy storage, their electrochemical properties and charge-discharge mechanisms remain poorly studied, and this area of research has only started to emerge. Emphasis has been put on studying two-dimensional materials, such as ones derived from benzenehexamine, benzenehexathiolate or hexasubstituted triphenylenes. Structures derived from hexasubstituted benzenes showed higher capacities, which is expectable considering higher concentrations of redox-active units. It should be stressed, however, that benzenehexathiolate and especially benzenehexamine precursors are challenging to synthesize and handle because they readily oxidize and decompose.^{131, 132} While still having many functional groups per mass unit, tetrasubstituted benzenes are much more stable and easily accessible compounds, which makes them more suitable for practical applications.

This Thesis is dedicated to nickel- and copper-based coordination polymers derived from 1,2,4,5-benzenetetraamine (**NiTIB** and **CuTIB**), which is a commercially available ligand. Objectives of this work included:

- Synthesis and characterization of the coordination polymers.
- Studying electrochemical properties of the materials in non-aqueous energy storage devices, which are based on alkali metal ions (Li^+ , Na^+ or K^+) as charge carriers. Applications as both positive or negative electrode materials are considered relevant.
- Studying the charge storage mechanisms of the materials.

Chapter 4. Experimental section

4.1. Synthesis of NiTIB and CuTIB

In a typical synthesis, nickel(II) chloride (1.36 mmol), copper(II) sulfate (1.36 mmol) or copper(II) chloride (1.36 mmol) was dissolved in 20 mL of water was added to 1,2,4,5-benzenetetraamine tetrahydrochloride (1.36 mmol) solution in 200 mL of water. Concentrated aqueous ammonia (4.5 mL) was added and the mixture was stirred in air at 65-70 °C for 1.5 h. The solvent was removed in vacuum and the residue was extensively washed with water and then with acetone using a Soxhlet extractor. The resulting product was oven-dried at 100 °C for 1 h.

4.2. Ball-milling

Milling was performed using a Fritsch Pulverisette 7 premium line system equipped with zirconia jars and 1 mm zirconia balls. The materials were milled with isopropanol for 30 min at 1000 rpm. The solvent was then vacuum-evaporated.

4.3. Electrode preparation

4.3.1. Electrodes for testing cathode materials

To test the ball-milled polymers as cathode materials, active materials, Super P carbon black and poly(vinylidene difluoride) (PVdF) with the mass ratio of 4:5:1 were thoroughly mixed with N-methylpyrrolidone (NMP) to form a homogeneous slurry, which was then tape-casted onto Al foil and dried in air at 70 °C. After that, the electrodes were vacuum-dried at 110 °C for ~5 h, calendered at room temperature and vacuum-dried again at 110 °C for ~2 h. The composite mass loading was around 1.2 mg cm⁻² (active material loading of 0.5 mg cm⁻²).

4.3.2. Electrodes for testing anode materials

To test ball-milled **CuTIB** as an anode material, the electrode was prepared the same way as for testing the polymers as cathode materials. To test pristine (non-ball-milled) **NiTIB** as an anode material, the procedure was similar, but the mass ratio between **NiTIB**, Super P and PVdF was 70:15:15, the slurry was tape-casted onto carbon-coated copper foil. The resulting composite mass loading was 1.3 mg cm^{-2} for galvanostatic experiments and 0.7 mg cm^{-2} for cyclic voltammetry experiments (the active material mass loadings of 0.9 and 0.5 mg cm^{-2} , respectively). For testing in potassium-based cells, electrodes with 80% wt. of **NiTIB**, 10% wt. of Super P and 10% wt. of carboxymethylcellulose sodium salt (CMC) were also prepared, with deionized water used instead of NMP for the slurry preparation; in this case, the slurry was tape-casted onto carbon-coated Al foil. Electrodes with the composite mass loadings of 1.6, 5.0 and 15.3 mg cm^{-2} were prepared (**NiTIB** loadings were 1.3, 4.0 and 12.2 mg cm^{-2} , respectively). For control experiments for testing the anode materials, electrodes containing 70% wt. of Super P and 30% wt. of PVdF were prepared, with carbon-coated Cu foil used as the current collector; the composite mass loading for these electrodes was 1.6 mg cm^{-2} (Super P mass loading of 1.1 mg cm^{-2}).

4.3.3. Electrodes for ex situ and operando XRD measurements

For XRD measurements of **NiTIB** as the anode material, an NMP-based homogeneous slurry containing 70% wt. of **NiTIB**, 15% wt. of Super P and 15% wt. of PVdF was tape-casted onto bare Al foil. Thickness of the slurry was set to 0.6 mm. The slurry was dried in air at $70 \text{ }^\circ\text{C}$, and the electrode was vacuum-dried at $110 \text{ }^\circ\text{C}$ overnight. The electrode was calendered, after which it delaminated from the foil. Circle electrodes with a diameter of 16 mm were prepared, and these free-standing electrodes were

additionally dried at 110 °C overnight. The electrode composite loading was 10.5-11 mg cm⁻² (**NiTIB** loading was 7.4-7.7 mg cm⁻²).

4.3.4. *Electrodes for operando Raman spectroscopy measurements*

For *operando* Raman spectroscopy measurements of pristine (non-ball-milled) **NiTIB** as the anode material, a water-based slurry containing 80% wt. of **NiTIB**, 10% wt. of Super P and 10% wt. of CMC was deposited onto carbon-coated Cu foil, the electrode was dried in air at 40 °C, vacuum-dried at 110 °C for ~5 h and calendered at room temperature. The composite mass loading was ~1.2 mg cm⁻². Rectangular electrodes with length of ~10 mm and width of ~1 mm were prepared.

4.4. Assembling of the electrochemical cells

All electrochemical cells were assembled in an Ar-filled glovebox, where levels of oxygen and moisture were below 1 ppm and 0.1 ppm, respectively.

4.4.1. *Galvanostatic charge-discharge and cyclic voltammetry*

For galvanostatic charge-discharge and cyclic voltammetry experiments, CR2032-type coin cells were assembled using alkali metals as counter electrodes (lithium for Li-based cells, sodium for Na-based cells, potassium for K-based cells). Glass fiber was used for the separators. For testing **NiTIB** and **CuTIB** as cathode materials in Li-based cells, the electrolyte was 1M LiPF₆ solution in an anhydrous mixture of ethylene carbonate and dimethyl carbonate (EC:DMC, 1:1 v/v). The same electrolyte was used for testing **CuTIB** as anode material in lithium-based cells. For **NiTIB** testing as the anode material, the electrolyte was 1M LiPF₆ solution in EC:DMC (1:1 v/v) or 1M lithium bis(trifluoromethanesulfonyl)imide (LiTFSI) solution in an anhydrous mixture of 1,2-dimethoxyethane and 1,3-dioxolane (DME:DOL, 1:1 v/v). For sodium- and

potassium-based cells, the electrolytes were 1.5M NaPF₆ and 1.5M KPF₆ solutions in anhydrous DME. Each cell contained 70-80 μL of the electrolyte.

4.4.2. *Ex situ XRD measurements*

For *ex situ* XRD measurements of **NiTIB**-based electrodes, disassemblable cells (ECC-Ref, EL-CELL) were assembled in two-electrode configuration. Alkali metals were used as counter-electrodes. Glass fiber was used for the separators, and additional layer of porous polypropylene separator was placed on top of each working electrode to avoid sticking of the glass fiber to the working electrode. The electrolytes were 1M LiPF₆ solution in EC:DMC (1:1 v/v), 1.5M NaPF₆ in DME and 1.5M KPF₆ in DME for Li-based, Na-based and K-based cells, respectively. Each cell contained 100 μL of the electrolyte.

4.4.3. *Operando XRD measurements*

For *operando* XRD measurements of **NiTIB**-based electrodes, a Swagelok-type cell with a beryllium window¹³³ was used. The working electrodes were placed next to the beryllium window, followed by three layers of glass fiber separator to avoid premature short-circuiting due to the dendrite growth. Alkali metals deposited onto a copper current collector were used as counter electrodes. The electrolytes were 1M LiPF₆ solution in EC:DMC (1:1 v/v), 1.5M NaPF₆ in diglyme and 1.5M KPF₆ in diglyme for Li-based, Na-based and K-based cells, respectively. The cells contained 240 μL of the electrolyte.

4.4.4. *Operando Raman spectroscopy measurements*

For *operando* Raman spectroscopy measurements, a cell with an optically transparent sapphire window (ECC-Opto-Std, EL-Cell)¹³⁴ was assembled in a two-electrode configuration. The electrodes were placed in direct contact with the sapphire window,

with the active material facing the window. Glass fiber was used for the separators, and alkali metals were used as the counter electrodes. The electrolytes were 1M LiPF₆ solution in EC:DMC (1:1 v/v), 1.5M NaPF₆ in diglyme and 1.5M KPF₆ in diglyme for Li-based, Na-based and K-based cells, respectively.

4.5. Electrochemistry

4.5.1. Galvanostatic charge-discharge

Galvanostatic charge-discharge experiments were performed using Neware BTS-4000 stations at various current densities. The potential ranges were 1.5–4.1 V or 2.0–3.8 V vs. Li⁺/Li for testing the polymers as cathode materials, 0.8–2.0 V vs. Li⁺/Li for testing **CuTIB** as anode material, and 0.5–2.0 V vs. M⁺/M (M = Li, Na or K) for **NiTIB** as anode material. Current densities and specific capacities were calculated basing on the mass of **NiTIB** or **CuTIB** unless stated otherwise. Coulombic efficiency was determined as the ratio between charge and discharge capacities of the half-cells for the anode materials, and as the ratio between discharge and charge capacities for the cathode materials.

4.5.2. Cyclic voltammetry

Cyclic voltammograms were measured with BioLogic VMP3 or Elins P-20X8 potentiostates at various scan rates. The potential ranges were the same as for the galvanostatic cycling experiments. Current densities were calculated basing on the mass of **NiTIB** or **CuTIB**.

4.6. Sample preparation for *ex situ* XRD measurements

The **NiTIB**-based electrodes were discharged in galvanostatic mode to 0.5 V vs. M⁺/M (M = Li, Na or K) at a current density of 30 mA g⁻¹. The cells were then disassembled in an Ar-filled glovebox, the electrodes were washed with ~4–5 mL of

anhydrous DME and dried in the glovebox environment at room temperature. In the glovebox environment, the washed and dried electrodes were placed onto a Mylar film in a sample holder for the Huber Guinier Camera 670 X-ray diffractometer, and the holder was sealed using Kapton tape to prevent decomposition in air during the measurements.

4.7. Operando XRD measurement conditions

The assembled electrochemical cell for XRD measurements was placed in a Bruker D8 ADVANCE powder X-ray diffractometer operating with CuK α radiation. The cell was connected to a Biologic SP-150 potentiostat/galvanostat. The XRD patterns were collected during galvanostatic discharging to 0.5 V vs. M⁺/M (M = Li, Na or K) and subsequent charging to 2.0 V M⁺/M. The current density was 30 mA g⁻¹ basing on the mass of NiTiB. Single scans were measured each 0.1 h, the resolution was 0.04°, the range of 2 θ was 12-32° for the lithium-based cell and 14-38° for sodium- and potassium-based cells.

4.8. Operando Raman spectroscopy measurement conditions

The assembled cell for Raman spectroscopy measurements was placed in a Thermo Scientific DXRxi Raman Imaging microscope equipped with lasers having excitation wavelengths of 780 nm or 532 nm. The cell was connected to a Biologic SP-150 potentiostat/galvanostat. Raman spectra were collected during two cyclic voltammetry scans performed at the scan rate of 0.047 mV s⁻¹ in the potential range of 0.5-2.0 V vs. M⁺/M (M = Li, Na or K). The spectra were collected in four points of the electrode located at the edges of a 0.1 mm square, and the spectra were averaged during post-processing. The laser power was 1 mW, exposure time was 0.5 s, and the number of

scans for each point was set to 60. Single scans were measured every 7 minutes (~20 mV).

4.9. Sample preparation for UV-Vis-NIR spectra measurements

4.9.1. Film preparation

36 mg of **NiTIB** and 4 mg of CMC were dispersed in 4 mL of deionized water via ultrasonication. The resulting suspension was deposited onto glass (~2x2 cm pieces, 0.6 mL of the suspension per piece) via spincoating. The rotation rate of the spincoater was set to 2000 rpm.

4.9.2. Preparation of alkaliation solutions

The alkaliation solutions were prepared in an Ar-filled glovebox. Naphthalene (0.8 mmol, 103 mg) was dissolved in anhydrous diglyme (8 mL). Metallic potassium (~50-100 mg) was then introduced to the solution, and the mixture was stirred at room temperature for 2 h, resulting in dark-green solution of naphthalenide. Excess of potassium was then taken out from the mixtures.

4.9.3. Alkaliation of the films

The **NiTIB**-based films were introduced to the pre-alkaliation solution and kept at room temperature for two days in an Ar-filled glovebox.

4.9.4. Washing and drying of the films

After the potassiation of **NiTIB**, the films were taken out from the solution, washed with ~4 mL of anhydrous DME and dried in an Ar-filled glovebox at room temperature.

4.10. Sample preparation for *ex situ* XPS measurements

For the *ex situ* measurements, the lithium-based coin cells were discharged to 1.5 V or 0.8 V vs. Li^+/Li at 50 mA g^{-1} . For studying charged states of the cathode

materials, discharging to 1.5 V was carried out before charging to 4.1 V at 50 mA g⁻¹. For the potassium-based cells, the electrodes were discharged/charged to 0.5/2.0 V vs. K⁺/K at 50 mA g⁻¹. The cells were disassembled in an Ar-filled glove box, the electrodes were extensively washed with anhydrous DMC (for the Li-based cells) or DME (for the K-based cells) and dried in argon at room temperature.

4.11. Pellet preparation

Cylindrical pellets of **NiTIB** or **CuTIB** ($d = 10$ mm) were prepared by cold pressing of the powders (70–150 mg) with commercial pressing equipment (Carver). Applied load was 5 metric tons.

4.12. Deposition of conductive coating onto the pellets

Prior to the conductivity measurements, top and bottom of the pellets were coated with 30–50 nm of gold using a Quorum Q150T ES magnetron. Sides of the pellet were covered with an adhesive tape before the sputtering.

4.13. Characterization

4.13.1. FTIR spectroscopy

FTIR spectra were measured using a Perkin Elmer Spectrum BX system in KBr-based pellets.

4.13.2. Raman spectroscopy

Raman spectra were measured using Thermo Fischer DXRxi Raman Imaging microscope equipped with 532 nm or a 780 nm laser.

4.13.3. UV-Vis-NIR spectroscopy

UV-Vis-NIR absorption spectra were recorded using an AvaSpec-2048-2 fiber-optic spectrometer placed in a nitrogen-filled glovebox.

4.13.4. Elemental analysis

Chemical composition (CHNS, halogens) was analyzed by express gravimetry using Elementar vario MICRO cube.

4.13.5. ESR spectroscopy

ESR spectrum of **CuTIB** was recorded using Adani CMS8400 spectrometer.

4.13.6. Conductivity measurements

The coated pellets were placed in a symmetrical cell between two copper disks. Direct-current polarization was applied using BioLogic VMP3. The voltage was changed in 50 mV steps between -1 and 1 V for **NiTIB** and between -2 and 2 V for **CuTIB**, the current was measured over 5 s at each step.

4.13.7. Scanning electron microscopy

SEM measurements were carried out using Hitachi SU8000 field-emission scanning electron microscope (FE-SEM). Images were acquired in a secondary electron mode at 20 kV accelerating voltage and at working distance of 8-10 mm.

4.13.8. Solid-state NMR spectroscopy

The ssNMR spectroscopy experiments were recorded on a Bruker AVANCE III spectrometer operating at 101 MHz for ^{13}C nuclei, using a 3.2 mm MAS probe at 22 ± 1 °C. The chemical shifts were referenced to tetramethylsilane (TMS) at 0 ppm by adjusting the CH_2 signal of solid adamantane spinning at 8 kHz to 38.48 ppm. Conventional cross-polarization (CP) experiments were used for the ^{13}C NMR spectra acquisition with the spinning rate of 16 kHz. For the cross-polarization, a ramped RF field from 70 to 100% was applied on ^1H , and the ^{13}C channel RF field was matched to obtain the optimal signal. The duration of ^1H $\pi/2$ pulse was 2.5 μs , contact time was 250 μs . SPINAL-64 decoupling was applied during the 20 ms acquisition with a RF amplitude

of 100 kHz. The delay between the scans was set to 5 s and the number of scans was 8192.

4.13.9. XPS measurements

XPS measurements were performed using a PHI XPS Versaprobe 5000 spectrometer (ULVAC Physical Electronics) or Phoibos 100 (Specs) hemispherical analyzer. Al or Mg sources were used, and the energy resolution was 0.5 or 0.8 eV. A dual-channel neutralizer was used to compensate for the local charging of the sample under study due to the loss of photoelectrons. Samples showed varying degrees of charging, which was compensated by calibrating the spectra to the C 1s peak at 284.8 eV. For *ex situ* measurements of the potassium-based cells, all spectra were calibrated for external reference Au 4f_{7/2} binding energies (84.1 eV); to study the active material itself rather than the SEI layer, Ar⁺ ions with 500 eV energy (3 min) were used to eliminate upper SEI layers and reach the subsurface prior to the measurements.

4.13.10. X-ray diffraction

XRD patterns of the pristine materials were recorded using a Bruker D8 ADVANCE diffractometer with CuK α radiation.

To determine the content of Cu₂O in **CuTIB** sample, fixed amounts of Cu₂O were added to the sample, and integral intensity of the most intensive Cu₂O peak (hkl = 111) was measured. The mass of **CuTIB** sample was fixed for all XRD measurements, and the measurement conditions were constant. Cu₂O content was calculated by extrapolating the resulting linear dependence to zero signal (standard addition method).

For the *ex situ* measurements of the electrodes, Huber Guinier Camera 670 operating with CoK α 1 radiation was used. The measurements were performed directly after the Kapton-sealed electrodes were taken out from the glovebox. Single XRD scans

were measured in the 2θ range of 4-100° each 10 minutes to monitor possible changes in the XRD patterns caused by oxidation. The measurements continued overnight. The scans that were measured before changes in the XRD patterns started to occur were then averaged.

Chapter 5. Results and Discussion

5.1. Synthesis and characterization

Synthesis of the coordination polymers was performed following the previously reported routes⁸⁷ and described in detail in Experimental section. Briefly, 1,2,4,5-benzenetetraamine tetrahydrochloride (BTA*4HCl) and NiCl₂ or CuSO₄ aqueous solutions were mixed, concentrated aqueous ammonia was added and the mixtures were heated in air, which caused the formation of precipitates (Figure 18). The resulting substances, denoted as **NiTIB** and **CuTIB**, were virtually insoluble in water and common organic solvents. Densities of **NiTIB** and **CuTIB** at room temperature in pellets was 1.84 and 1.74 g cm⁻³, respectively.

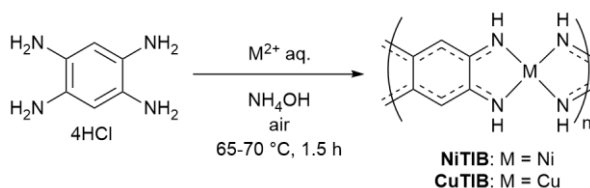


Figure 18. Synthesis of **NiTIB** and **CuTIB**.

Solid-state Magic Angle Spinning NMR (MAS ssNMR) spectrum of **NiTIB** showed two major ¹³C signals at 93.70 and 168.81 ppm (Figure 19a), which correspond to the CH- and CN-carbons in the molecular structure of the polymer, respectively. The observed chemical shift values agreed well with those reported for the low molecular weight analogs of **NiTIB** produced in the reactions of an oxidized form of BTA (3,6-diimino-1,4-cyclohexadiene-1,4-diamine, DCD) and Ni(acac)₂.¹³⁵

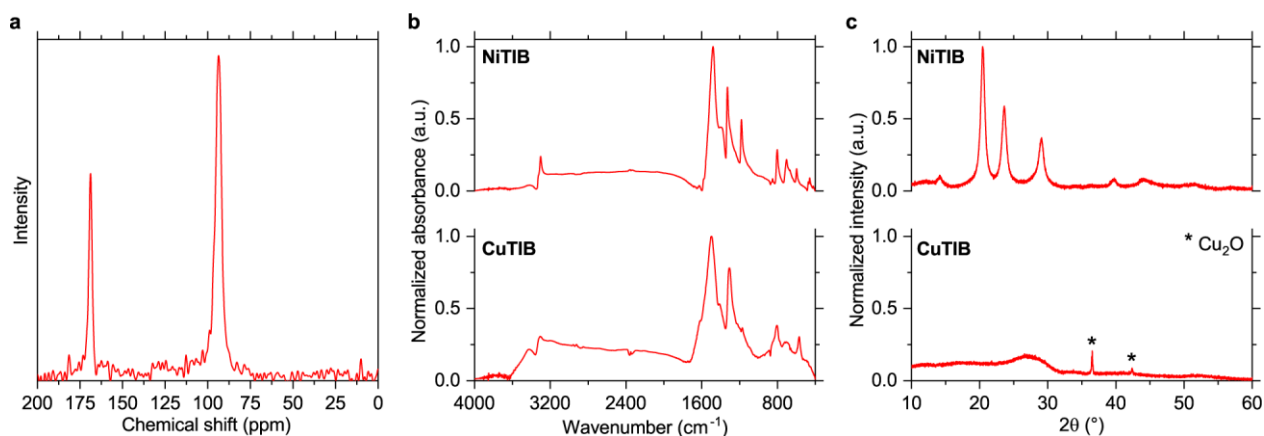


Figure 19. ^{13}C MAS ssNMR spectrum of **NiTIB** (a), FTIR spectra of the as-synthesized **NiTIB** and **CuTIB** (b) and XRD patterns for the as-synthesized **NiTIB** and **CuTIB** (c).

Free DCD ligand shows three signals at 99.35, 147.3 and 165.15 ppm in ^{13}C MAS ssNMR,¹³⁵ indicating that the imino and amino groups are spectrally well distinguishable. In **NiTIB**, all NH-groups were equivalent, i.e., each **NiTIB** repeating unit can be represented as a superposition of two resonance structures (Figure 20). The chemical shift for the CN-carbons in **NiTIB** was larger compared to the CN-carbons of the free DCD, which is expected for the ligand groups binding a cation. The chemical shift for the CH-carbons of **NiTIB** was in the higher field compared to the corresponding atoms of the free ligand, indicating the increase in the electron density at these sites.

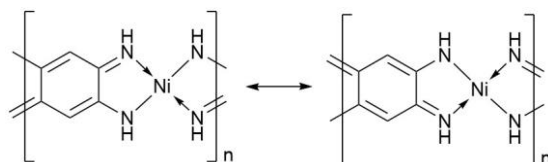


Figure 20. Resonance structures of **NiTIB** repeating unit.

The MAS ssNMR spectrum of **CuTIB** provided no useful information since it appeared as a single broad line due to the presence of paramagnetic Cu^{2+} ions. Indeed, the electron spin resonance (ESR) spectrum revealed a broad signal with g-factor value

of 2.0685 (Figure A1), which is matching that reported for similar Cu^{2+} -based coordination complexes.^{136, 137} FTIR spectra of **NiTIB** and **CuTIB** were similar (Figure 19b), which indicates that these materials shared the same structural pattern. The FTIR peaks at $\sim 3300 \text{ cm}^{-1}$ correspond to NH-stretching vibrations, and the most intensive bands at $\sim 1400\text{-}1500 \text{ cm}^{-1}$ should be attributed to vibrations associated with C=N and C=C stretching.¹²⁹

NiTIB had an intensive well-structured Raman spectrum (Figure 21). The signals at $\sim 1400\text{-}1500 \text{ cm}^{-1}$ that were also intensive in the FTIR spectra should be associated with C=N and C=C bonds, while an intensive peak at $\sim 635 \text{ cm}^{-1}$ should be attributed to Ni–N bond stretching.¹¹¹ The signals appearing at $\sim 2000\text{-}2100 \text{ cm}^{-1}$ are combinational bands of C=N/C=C and Ni–N vibrations. The Raman spectrum of **CuTIB** (Figure 21) shared similar features, which is another indicator of similar structural patterns for **NiTIB** and **CuTIB**. The bands associated with the M–N bond stretching had lower frequency for **CuTIB**, which is likely associated with larger mass of Cu atoms.

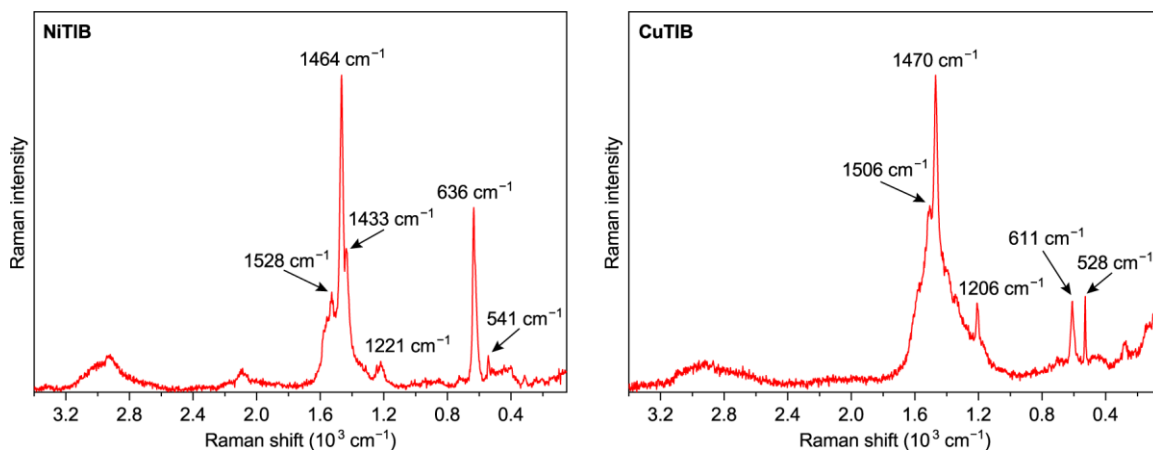


Figure 21. Raman spectra of **NiTIB** and **CuTIB** measured using a laser with $\lambda = 532$ nm.

According to powder XRD, **NiTIB** formed a crystalline structure, whereas **CuTIB** was amorphous (Figure 19c). The XRD pattern of **NiTIB** was in a good agreement with the previously reported data.⁸⁷ Small amount of Cu₂O was observed in the **CuTIB** sample, which indicates that Cu²⁺ was partially reduced by BTA during the synthesis. The content of Cu₂O was 2% wt., as determined by the XRD method of standard additions (Figure A2, see Experimental section for details). Almost no changes in the XRD pattern of **CuTIB** were observed when copper sulfate was replaced with copper chloride (Figure A3), indicating that presence/absence of SO₄²⁻ or Cl⁻ ions did not affect the crystallinity. The sample that was synthesized from copper sulfate was used in the further studies.

It might be supposed that the copper-based material is disordered because, in contrast to **NiTIB**, its formation involves reduction of metal ions by benzenetetramine. This side reaction possibly results in a different structure of **CuTIB** intermediates, as well as increased concentration of defects that prevents long-range ordering. Since a part of Cu²⁺ is consumed by Cu₂O precipitation, it results in off-stoichiometry between the ligands and the metal ions, which leads to decreased polymerization degree due to chain termination by the ligand moieties. It was previously shown that such off-stoichiometry leads to amorphization of similar coordination polymers.¹²⁶ Reduction of Cu(II) can be suppressed by increasing the redox potential of copper ions (*via* changing their coordination environment). Alternatively, benzenetetramine can be oxidized into 2,5-diamino-1,4-benzoquinonediimine¹³⁵ before Cu²⁺ ions are introduced into the reaction mixture. Optimization of the synthetic conditions is a subject of future research.

The elemental analysis of both materials revealed the discrepancy with the theoretical composition of (MC₆H₆N₄)_∞, which was more prominent in the case of **CuTIB**

(Table 1). In particular, the nitrogen content was lower than expected, which was likely due to the partial hydrolysis of NH-groups. The discrepancy might also be due to the relatively low degree of polymerization, especially for **CuTIB**. No chlorine or sulfur were found in the synthesized materials.

Table 1. Elemental composition of **NiTIB** and **CuTIB**.

| Material | Theor./Exp. | H (wt. %) | C (wt. %) | N (wt. %) | C:H (at. ratio) | C:N (at. ratio) |
|--------------|-------------|-----------|-----------|-----------|-----------------|-----------------|
| NiTIB | Theor. | 3.14 | 37.37 | 29.05 | 1 | 1.5 |
| NiTIB | Exp. | 3.42 | 34.43 | 25.26 | 0.92 | 1.59 |
| CuTIB | Theor. | 3.06 | 36.46 | 28.34 | 1 | 1.5 |
| CuTIB | Exp. | 3.30 | 31.39 | 19.78 | 0.80 | 1.85 |

Scanning electron microscopy (SEM) was used to reveal the morphology of the solid powders of both coordination polymers. The **NiTIB** particles appeared as ~200 nm long and 20-40 nm wide filaments, while **CuTIB** formed irregular agglomerates up to 5 μm in size (Figure 22).

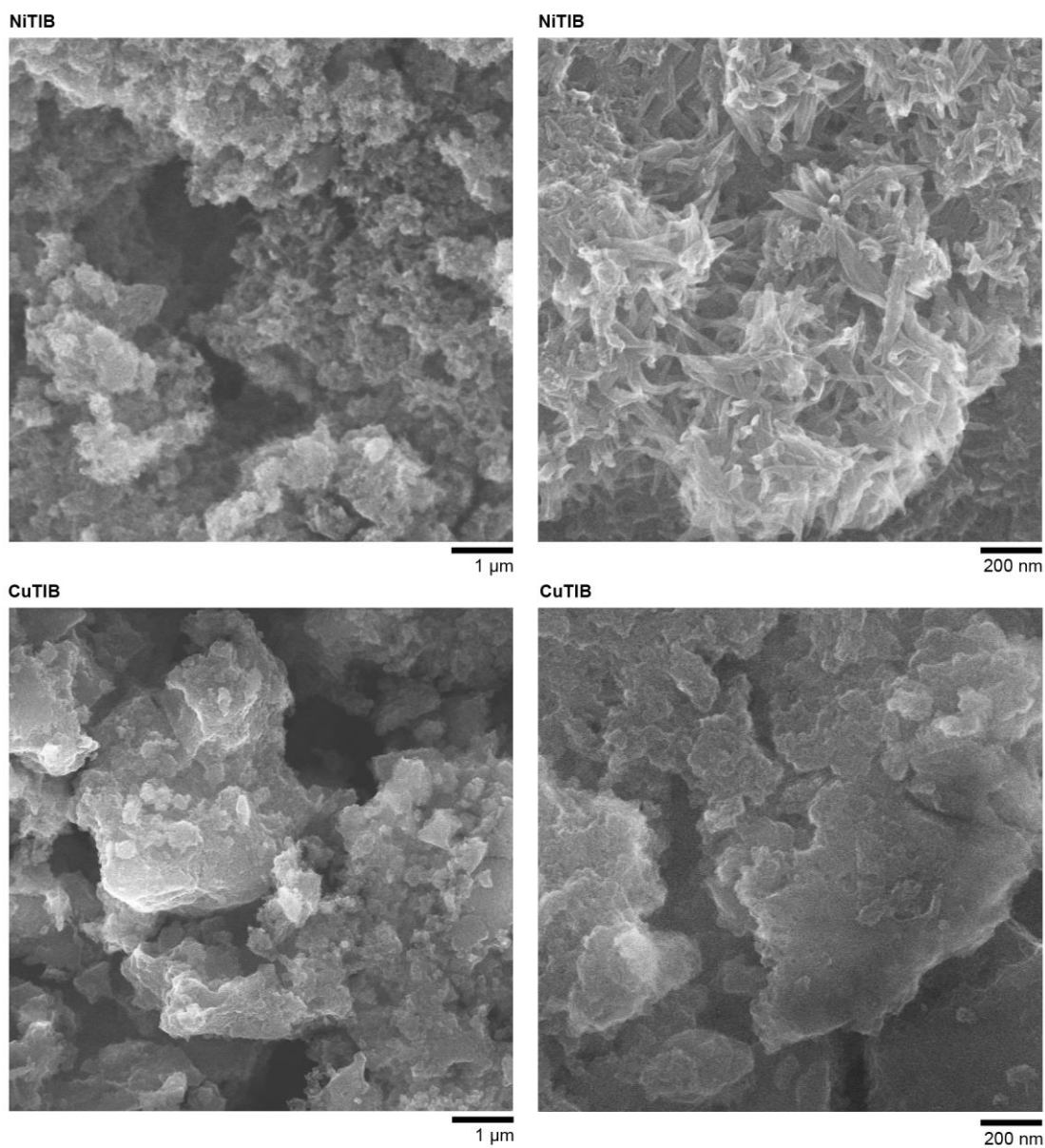


Figure 22. SEM images of **NiTiB** and **CuTiB**.

The electron conductivity of **NiTiB** at room temperature measured for pressed pellets was $2.0 \cdot 10^{-7} \text{ S cm}^{-1}$, as determined by direct-current polarization (Figure 23). For **CuTiB**, the conductivity was $<10^{-13} \text{ S cm}^{-1}$ (direct current was $<10^{-13} \text{ A cm}^{-1}$ when the voltage was set to 2 V).

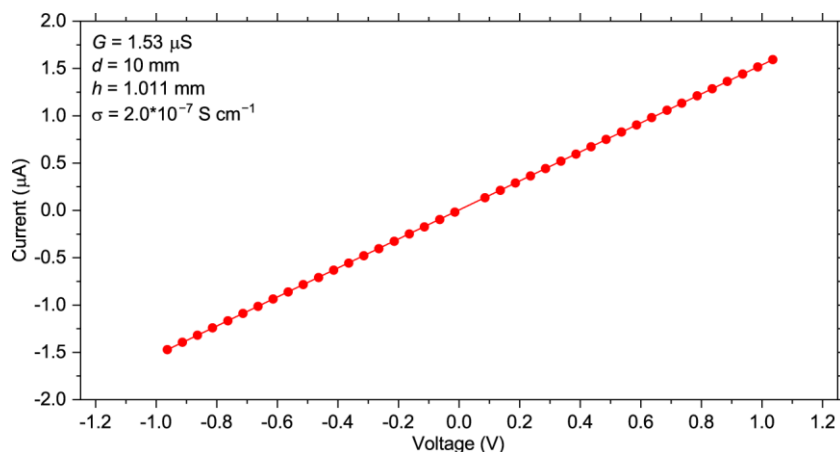


Figure 23. Direct-current polarization data for a **NiTIB** pellet at room temperature.

Conductance, diameter and height of the cylindrical pellet are given in the figure.

For π -d conjugated polymers, one would expect higher conductivities for such coordination compounds considering the literature data. Metal complexes with BTA as a ligand were shown to have efficient π -electron delocalization.¹³⁵ On the one hand, low conductivity of **NiTIB** and **CuTIB** might be explained by the presence of defects, which are known to nullify the intrinsic properties of the materials: for example, disordered HAB-derived MOFs show insulating behavior, although they are conductive in high quality crystals.⁹¹ On the other hand, one-dimensional nature of the polymers reported here can also impair the conductivity as compared to the 2D MOFs that were shown to be highly conductive. The same trend was previously observed for thiolate-based polymers: while two-dimensional frameworks derived from benzenhexathiolate are highly conductive ($>10 \text{ S cm}^{-1}$),¹⁰⁷ the electric conductivity of one-dimensional Ni-based polymer derived from benzenetetrathiol is low ($\sim 10^{-5} \text{ S cm}^{-1}$).⁸⁹

5.2. Applications as cathode materials

5.2.1. Electrochemical properties

The materials were tested in lithium-based half-cells in the potential ranges of 1.5-4.1 V or 2.0-3.8 V vs. Li^+/Li (see Experimental section for details). 1M LiPF_6 solution in a mixture of ethylene carbonate and dimethyl carbonate (1:1 v/v) was used because it is a commercially available electrolyte applied in the battery industry.¹³⁸ To increase the capacity, **CuTIB** and **NiTIB** were subjected to ball-milling, which led to a decrease in the particle size, most notably for **CuTIB** (Figure A4). This strategy was chosen because nanosizing is one of the main approaches for enhancing the electrochemical performance, which alleviates ion and electron transport and increases specific capacity and rate capability for the materials with low conductivity.¹³⁹ No substantial changes in the FTIR spectra of the ball-milled samples were observed compared to the as-synthesized ones (Figure A5), which indicates that no considerable chemical decomposition occurred under the ball-milling conditions.

The capacity of the ball-milled **CuTIB** in 1.5-4.1 V range was up to 262 mA h g^{-1} at 50 mA g^{-1} (Figure 24a), which was higher than for the previously reported hexaaminobenzene-based MOF (155 mA h g^{-1} at 10 mA g^{-1}).¹¹⁴ At the same time, the capacity of the material dropped after 25 cycles in the galvanostatic mode to about 25 mA h g^{-1} (Figure 24b). Increasing the current rate while charging/discharging the battery stabilized the electrochemical performance of the material. At 1 A g^{-1} , the maximal capacity was 145 mA h g^{-1} , and 50 mA h g^{-1} retained after 150 cycles (Figure 24b).

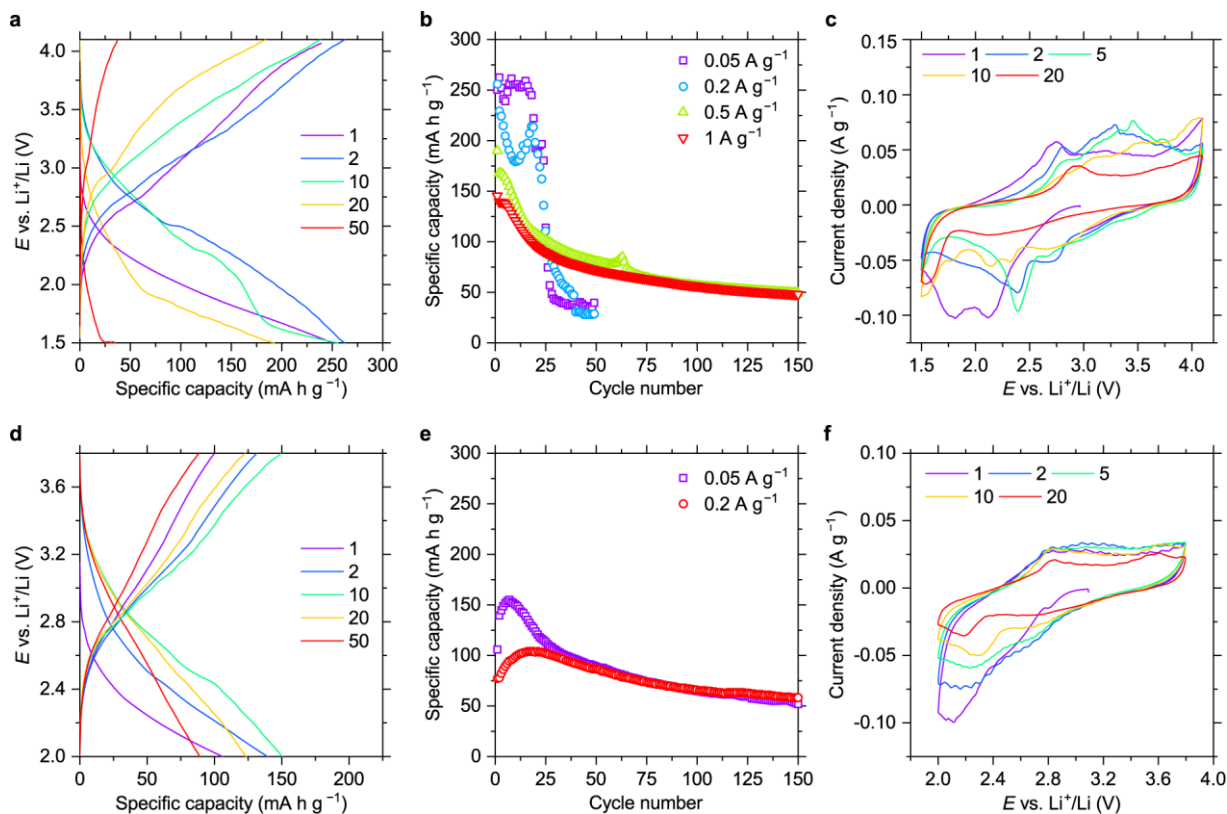


Figure 24. Electrochemical behavior of ball-milled **CuTiB** as a cathode material: charge-discharge curves for different cycles at 50 mA g^{-1} in 1.5-4.1 V range (a); specific discharge capacities in 1.5-4.1 V range (b); CVs for different cycles at 0.1 mV s^{-1} scanning rate in 1.5-4.1 V range (c); the same set of plots for 2.0-3.8 V range (d-f).

To improve the cycling stability at lower current rates, the operating potential range was narrowed to 2.0-3.8 V vs. Li^+/Li . It was supposed that narrowing the potential range should help to suppress the irreversible structural transformations and parasitic reactions occurring at low or high voltages. Indeed, the capacity after 150 cycles at 50 mA g^{-1} increased to 50 mA h g^{-1} (Figure 5c, d). The maximal capacity of 155 mA h g^{-1} was observed at 50 mA g^{-1} .

NiTiB demonstrated lower capacities in the cathode mode as compared to **CuTiB** (Figure 25). At 50 mA g^{-1} in 1.5-4.1 V range, the capacity reached 155 mA h g^{-1}

g^{-1} . Limiting the voltage range to 2.0-3.8 V improved the **NiTIB** cycling stability. After 100 cycles at 200 mA g^{-1} , the capacity was 40 mA h g^{-1} . The maximal capacity for **NiTIB**-based cathodes at 50 mA g^{-1} in the 2.0-3.8 V range was 98 mA h g^{-1} .

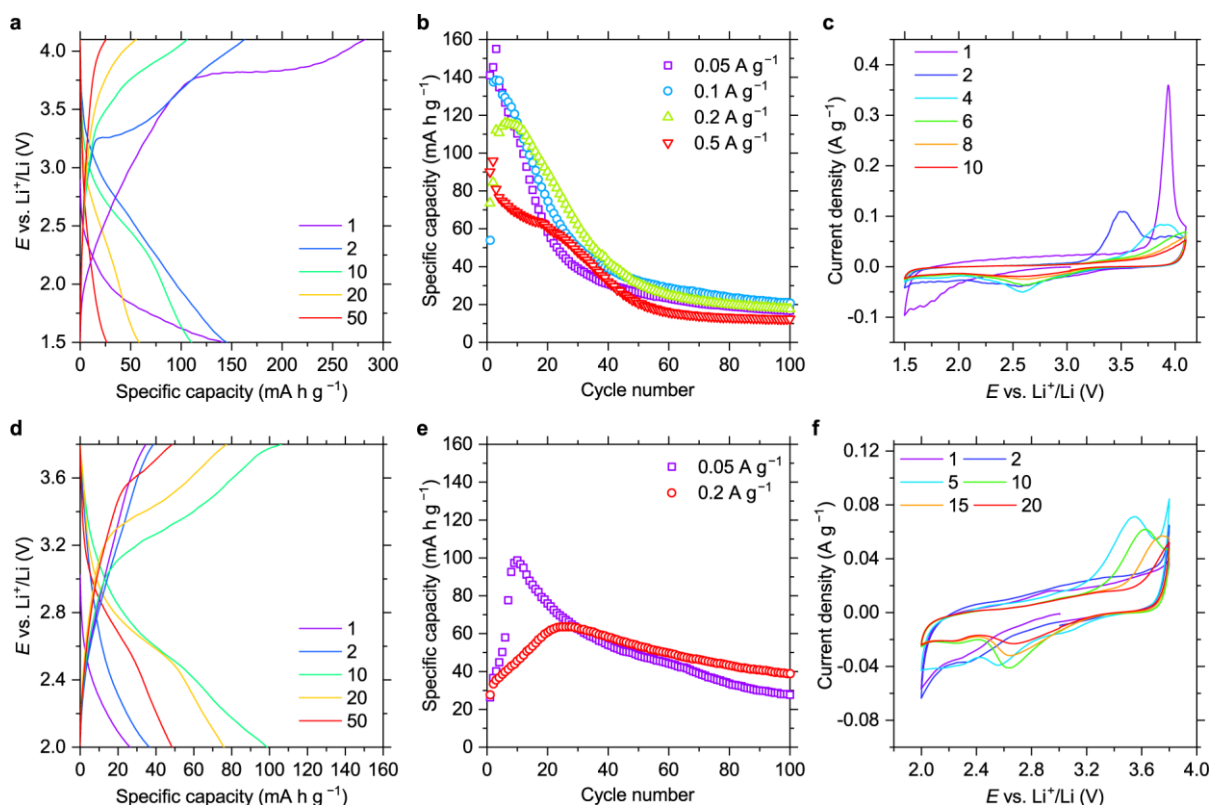


Figure 25. Electrochemical behavior of ball-milled **NiTIB** as a cathode material: charge-discharge curves for different cycles at 50 mA g^{-1} in 1.5-4.1 V range (a); specific discharge capacities in 1.5-4.1 V range (b); CVs for different cycles at 0.1 mV s^{-1} scanning rate in 1.5-4.1 V range (c); the same set of plots for 2.0-3.8 V range (d-f).

The maximal energy densities of **CuTiB** and **NiTIB** calculated per mass of the coordination polymers are depicted in Figure 26a. The highest value was 616 W h kg^{-1} for **CuTiB** in the 1.5-4.1 V range. However, it should be noted that in contrast to classic cathode materials, such as LiCoO_2 or LiFePO_4 , the studied polymers require equivalents of additional counter-ions (Li^+ and PF_6^-) for proper working, which limits the energy density. To make the estimation of specific energy more balanced, masses of

the counter-ions were considered. As discussed below in section 5.2.2, both rocking-chair and dual-ion operation modes are possible for **CuTIB** and **NiTIB**. The practical capacity proportion for these mechanisms is ambiguous at this point. For this reason, two extreme cases were considered: (a) pure rocking-chair battery operation mode, where the polymers act as n-type materials; (b) pure dual-ion battery operation mode, where the polymers act as p-type materials. The energy per material corrected mass unit (W_{corr}) was calculated as follows:

$$W_{corr} = \frac{W}{1 + \frac{Q}{F} M_{ci}} \quad (13)$$

where W is energy per **CuTIB/NiTIB** mass unit, Q is capacity per **CuTIB/NiTIB** mass unit, F is Faraday constant (26 801 mA h mol⁻¹), M_{ci} is molar mass of lithium (for the n-type mode) or LiPF₆ (for the p-type mode). Although LiPF₆ originated solely from the electrolyte in the experiments, it is principally possible to use mixtures of solid salts and relatively small amounts of electrolyte.⁷³ For this reason, the total mass of the electrolyte was not considered. The resulting ranges for specific energy values are presented in Figure 26b.

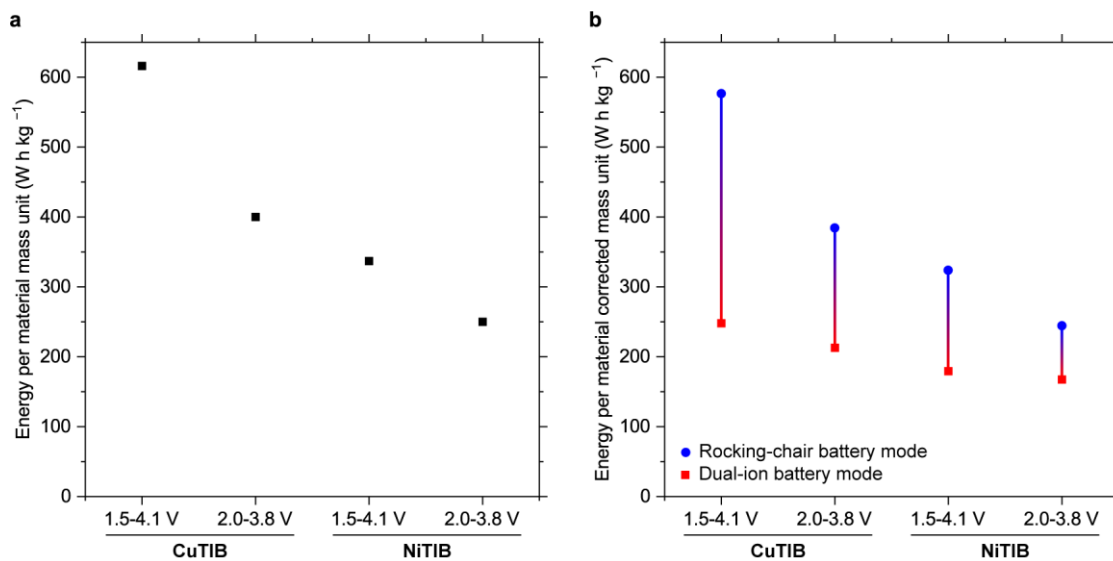


Figure 26. Maximal specific energy achieved for **CuTIB** and **NiTIB**, calculated per material mass unit (a) and material corrected mass unit (b).

For both **CuTIB** and **NiTIB**, the cyclic voltammetry profiles and charge-discharge curve profiles could generally be considered typical for pseudocapacitors (see section 2.1.1). The GCD curves (Figure 24a, d and Figure 25a, d) were sloping, and the CV profiles featured broad peaks, with the only exception of **NiTIB** at the first cycle in the 1.5-4.1 V range. However, poor cycling stability of the materials made kinetic studies, i.e., defining the current-scan rate dependencies in CVs, problematic.

5.2.2. Charge-discharge mechanisms

To study the charge storage mechanisms of the cathode materials, *ex situ* XPS measurements were carried out. For the **CuTIB** electrode charged to 4.1 V, the N1s peak appeared at 400.3 eV (Figure 27a), which was higher than for the initial state. It indicates that **CuTIB** underwent oxidation at high potentials and formed relatively stable cation species similar to the polymeric aromatic amines.¹⁴⁰ It might be supposed that the positive charge on the polymer backbone was balanced by PF₆⁻ anions. While discharging from 4.1 V to 1.5V, the reduction of the positively charged backbone was

followed by its lithiation at lower potentials (see section 5.3.2). In other words, **CuTIB** polymer backbone was ambipolar and, therefore, could accommodate both negative and positive charges at low and high cell potentials, respectively.

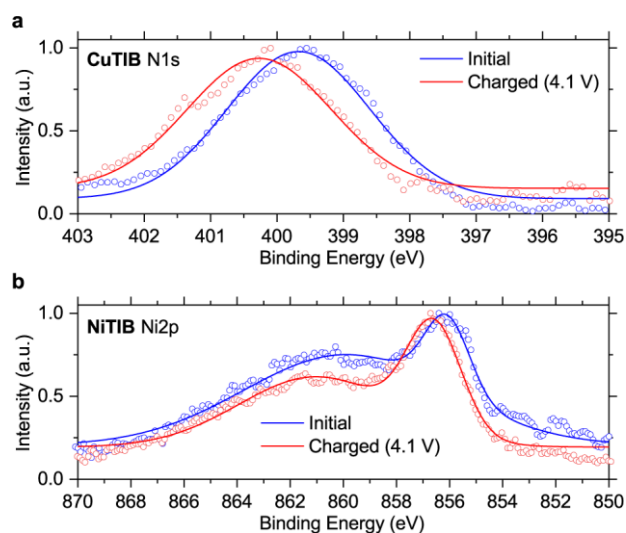


Figure 27. X-ray photoelectron spectra regions of the cathode materials: N1s region for **CuTIB** (a) and Ni2p region for **NiTIB** (b).

After charging to 4.1 V, the Ni binding energy of **NiTIB** increased as compared to the initial state with the Ni2p_{3/2} peak shifting from 856.2 to 856.7 eV (Figure 27b). This shift should be related to the positive charging of the polymer backbone compensated by PF₆⁻ anions, as revealed for **CuTIB**. Similar behavior was observed for the Ni hexaaminobenzene-based MOF charged above 4 V vs. Li⁺/Li in a lithium-based battery (see section 2.3.2).¹¹⁴

5.3. Applications as anode materials

5.3.1. Electrochemical properties

Electrochemical properties of the materials were studied in half cells with alkali metals at lower potentials (0.8-2.0 V vs. Li⁺/Li or 0.5-2.0 V vs. M⁺/M, M = Li, Na or K). Cycling at <0.5 V vs. M⁺/M was not applied to avoid irreversible structural

transformations that lead to rapid capacity fading, as previously reported for similar materials (see section 2.3.3).^{126, 127}

For the ball-milled **CuTIB** in lithium-based cells, the reversible capacity was up to 125 mA h g⁻¹ at 50 mA g⁻¹ in the potential range of 0.8-2.0 V vs. Li⁺/Li (Figure 28a, c), basing on the mass of **CuTIB**. After subtracting the contribution from Super P, which is also electrochemically active at low potentials, the capacity of **CuTIB** was estimated as ~70 mA h g⁻¹ (the capacity of Super P in the 0.8-2.0 V vs. Li⁺/Li range was ~43 mA h g⁻¹, see Figure A6). The material showed moderate cycling stability at 50 mA g⁻¹ (Figure 28c). The charge-discharge curves were sloping, and the CV profiles showed no distinct features (Figure 28a, b). Copper(I) oxide, which was detected as a minor impurity in **CuTIB** samples by XRD, is known to be an anode material that shows a plateau at 1.0-1.2 V vs. Li⁺/Li during the first discharge in galvanostatic mode, and a sharp peak in the CV, which are attributed to Cu₂O transformation into copper.^{141, 142} Since the CV profiles showed no signatures of the Cu₂O reduction, its presence might be neglected when considering the electrochemical properties of **CuTIB**.

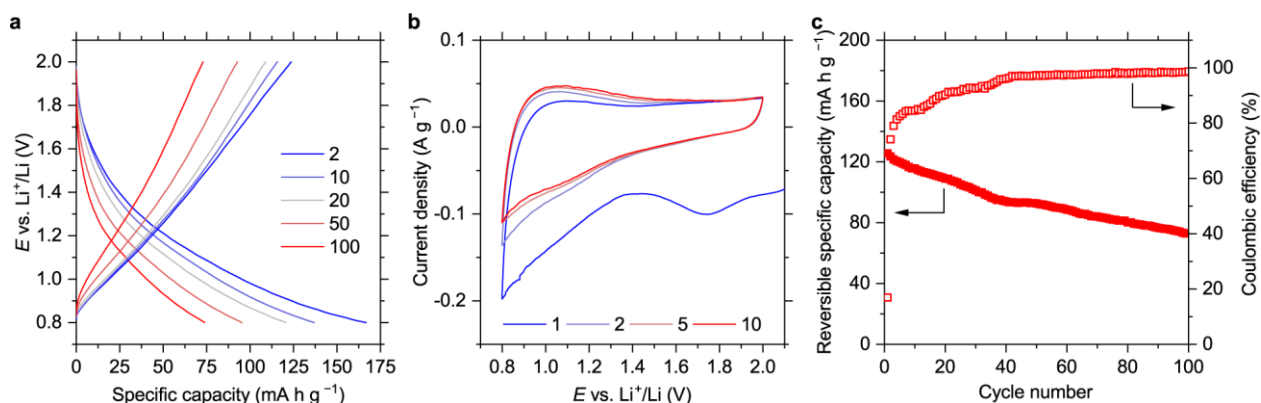


Figure 28. Electrochemical behavior of **CuTIB** in lithium-based cells in the potential range of 0.8-2.0 V vs. Li⁺/Li: charge-discharge curves for different cycles at 50 mA

g^{-1} (a); CVs for different cycles at 0.1 mV s^{-1} scanning rate (b); cycling stability at 50 mA g^{-1} (c).

Much more interesting results were obtained for **NiTIB** in the region of low potentials. **NiTIB** was not ball-milled for these studies. In lithium-based cells, the material was tested with two electrolyte systems: a carbonate-based electrolyte, 1 M LiPF_6 in EC:DMC (1:1 v/v), and an ether-based electrolyte, 1 M LiTFSI in DME:DOL (1:1 v/v), which is widely applied for some battery chemistries, e.g., Li-S cells.¹⁴³ At low current densities, the material behaved similarly with both electrolytes (Figure 29). The reversible capacity approached 280 mA h g^{-1} at 100 mA g^{-1} (calculated per **NiTIB** mass unit) in the potential range of 0.5-2.0 V vs. Li^+/Li . The average delithiation potential was 1.35 V vs. Li^+/Li .

NiTIB demonstrated excellent high-rate capabilities, especially in the ether-based electrolyte. At 5 A g^{-1} (charging in <2 minutes), the capacity reached up to 152 and 108 mA h g^{-1} with the ether-based and carbonate-based electrolytes, respectively. It could be supposed that faster charge-discharge kinetics with the ether-based electrolyte was associated with its lower viscosity and higher ionic conductivity.¹⁴⁴⁻¹⁴⁶ However, the electrolyte conductivity unlikely plays an important role for thin electrodes (**NiTIB** loading of 0.9 mg cm^{-2}) at moderate charge-discharge rates. Another reason could be the difference in the conductivities of the SEI layers that form during the initial cycles. This hypothesis can be probed using electrochemical impedance spectroscopy, which is a subject of future studies.

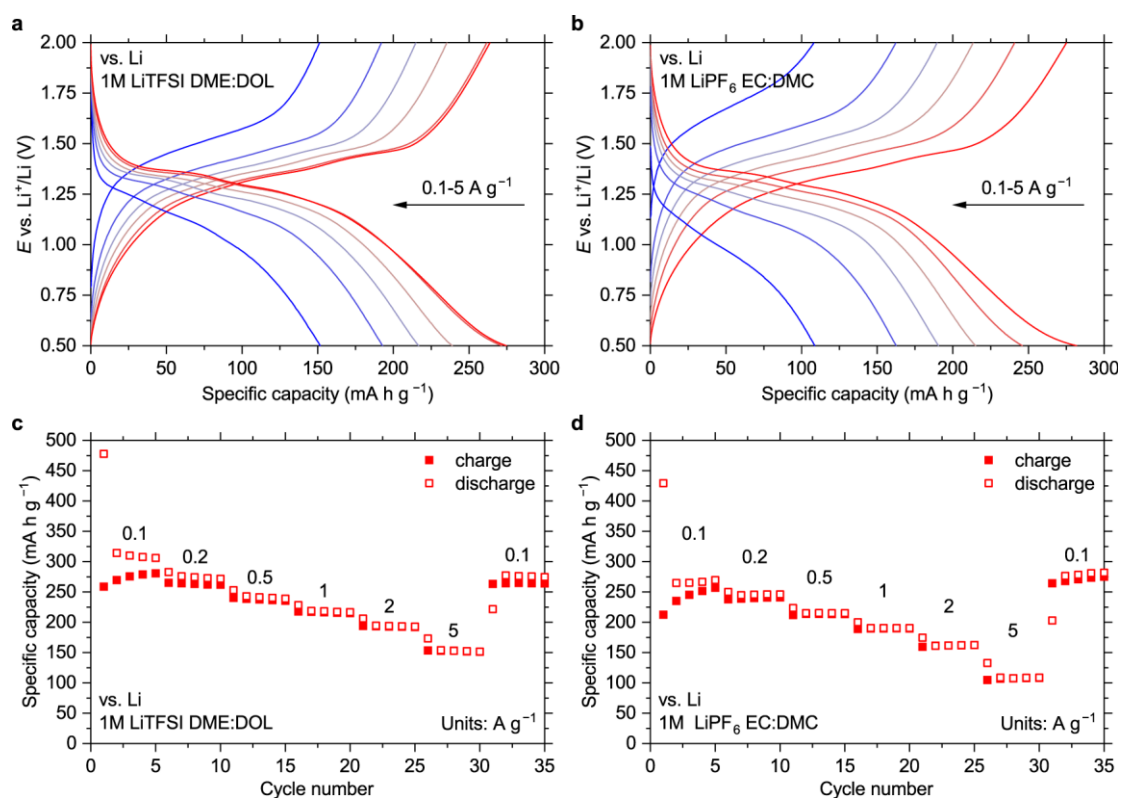


Figure 29. Charge-discharge curves of **NiTiB**-based electrodes in lithium-based cells with the ether-based (a) and carbonate-based (b) electrolytes at 0.1, 0.2, 0.5, 1, 2 and 5 A g⁻¹; dependencies of charge and discharge capacities on the cycle number at varying current densities for the cells with ether-based (c) and carbonate-based (d) electrolytes. The electrodes contained 75% wt. of **NiTiB**. Decent performance was shown for diluted electrodes (40% wt. of **NiTiB**) as well.¹⁴⁷

Moreover, the material showed impressive performance in sodium- and potassium-based cells (Figure 30). 1.5M NaPF₆ or KPF₆ solutions in DME were used because decent electrochemical performance was previously achieved with these electrolytes for organic-based materials.^{148, 149} The reversible capacities at 0.1 A g⁻¹ were 225 and 280 mA h g⁻¹ for Na-based and K-based systems, respectively, and the capacity decreased only slightly even when the current density was increased to 5 A g⁻¹. The

average desodiation and depotassiation potentials at 0.1 A g^{-1} were $1.1 \text{ V vs. Na}^+/\text{Na}$ and $1.35 \text{ V vs. K}^+/\text{K}$, respectively.

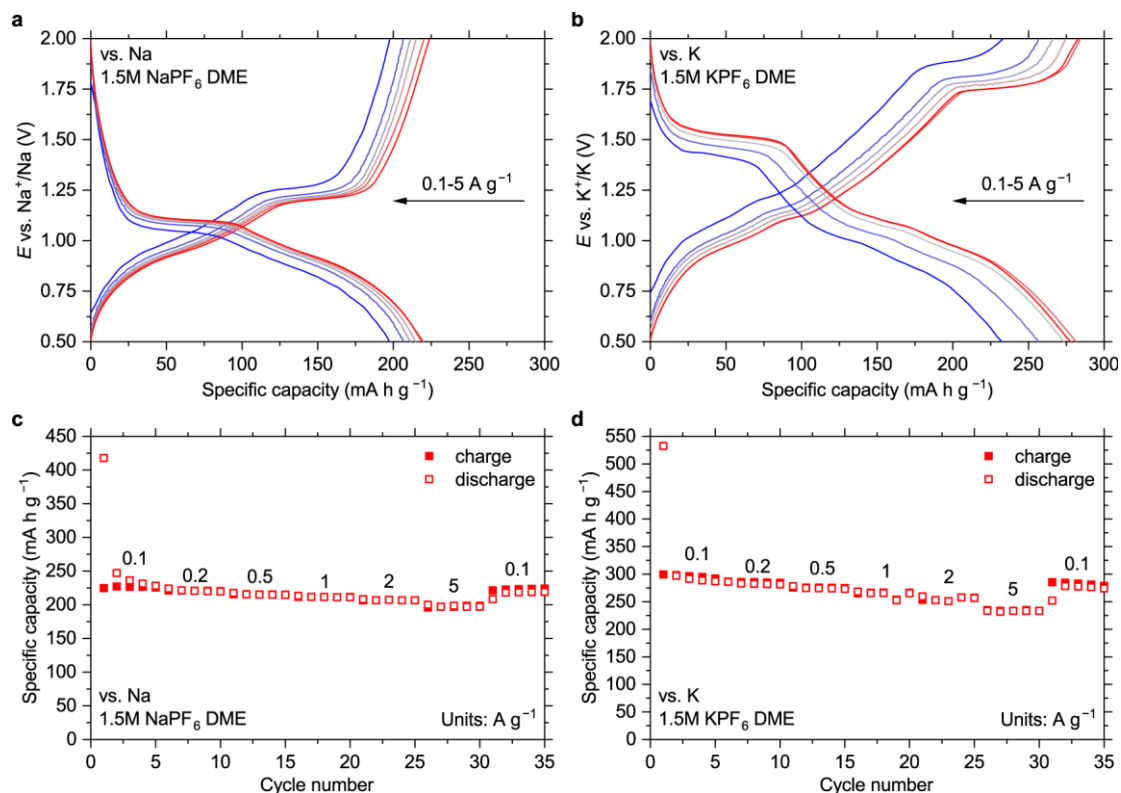


Figure 30. Charge-discharge curves of **NiTiB**-based electrodes in sodium (a) and potassium (b) cells at 0.1, 0.2, 0.5, 1, 2 and 5 A g⁻¹; dependencies of charge and discharge capacities on the cycle number at varying current densities for the sodium (c) and potassium (d) cells.

The specific capacities per **NiTiB** mass unit for different cell types and current densities are summarized in Figure 31a. The capacities after subtracting the contribution of Super P (Figure 31b, the data for Super P can be found in Figure A6 and Figure A7) were up to 265 mA h g^{-1} for Li-based and K-based cells, and up to 215 mA h g^{-1} for Na-based cells.

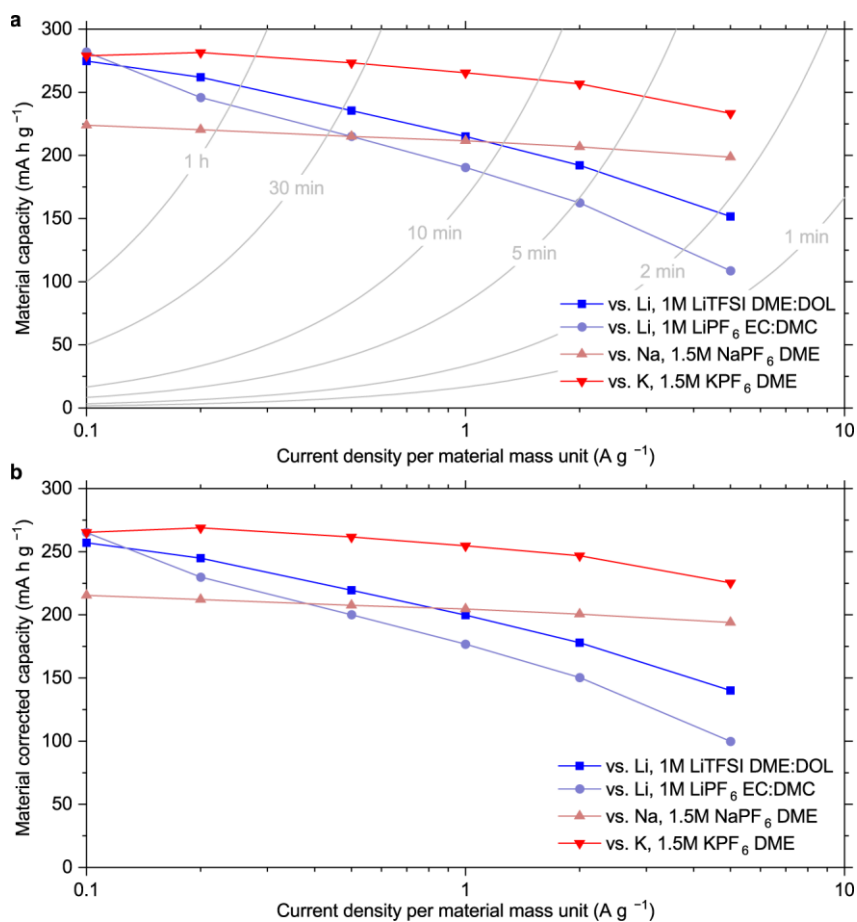


Figure 31. Capacity vs. current density calculated per **NiTIB** mass for various types of cells (a) and **NiTIB** capacity after subtracting the contribution from Super P (b).

For the potassium-based cells, electrodes with different compositions and mass loadings were tested (see Experimental section for details). The data for different electrodes are summarized in Figure 32. By increasing the electrode mass loading to 15.3 mg cm^{-2} , the areal capacity could be increased up to $2.73 \text{ mA h cm}^{-2}$. According to the recent literature analysis carried out by myself,¹⁵⁰ this areal capacity is one of the highest for potassium-ion battery anodes, with only one report on graphite¹⁵¹ showing higher values. Increasing the areal capacity helps to improve the overall energy density of the devices by decreasing the mass fraction of electrochemically inactive components, such as current collectors, sealing cases, separators, etc.¹⁵² Additionally, it helps to decrease

the battery cost per kWh and therefore make the production economically viable.¹⁵³ It should be noted that performance of the electrodes with high material loadings can be further improved by optimizing the electrode morphology and composition, e.g., by making it more porous or introducing other types of conductive fillers.^{154, 155}

Cycling stability of **NiTIB** was studied in different types of cells at the current density of 2 A g^{-1} . Before cycling at the higher currents, the cells were subjected to five cycles at 0.1 A g^{-1} to eliminate irreversible processes and suppress the activation effects when the initial capacity is very low and then steadily increases upon cycling.^{147, 156} As shown in Figure 33, excellent cycling stability could be reached for **NiTIB** in Li-based, Na-based and K-based systems. For the lithium-based cells, the capacity fading rate was much slower for the carbonate-based electrolyte (Figure 33a). The capacity fading rate was 0.005% per cycle ($0.009 \text{ mA h g}^{-1} \text{ cycle}^{-1}$), 0.011% per cycle ($0.024 \text{ mA h g}^{-1} \text{ cycle}^{-1}$) and 0.028% per cycle ($0.069 \text{ mA h g}^{-1} \text{ cycle}^{-1}$) for the Li-based, Na-based and K-based cells, respectively.

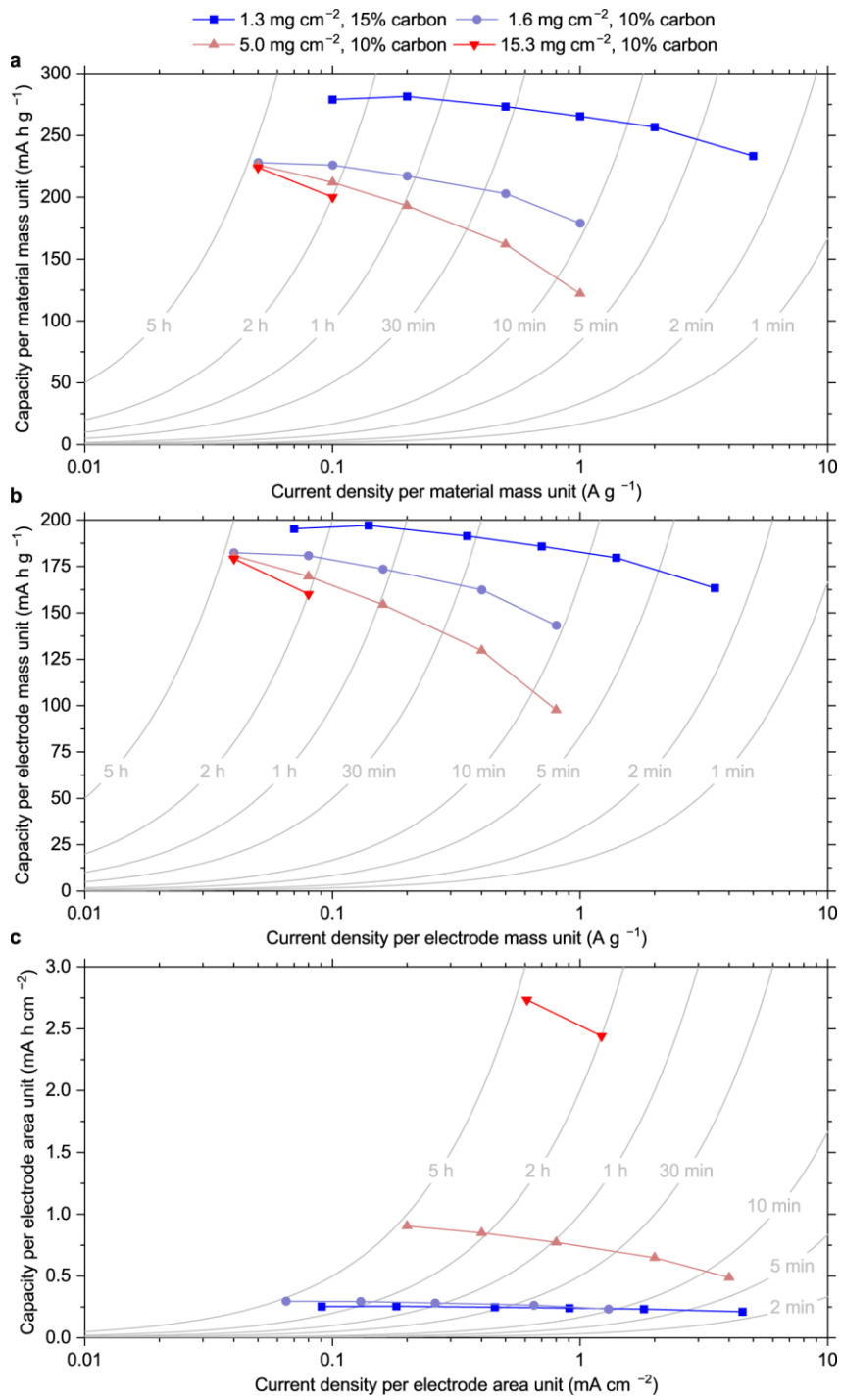


Figure 32. Rate performance of NiTiB-based electrodes with different electrode loadings and Super P contents in potassium cells: capacity vs. current per material mass (a), total electrode mass (b) and electrode area (c).

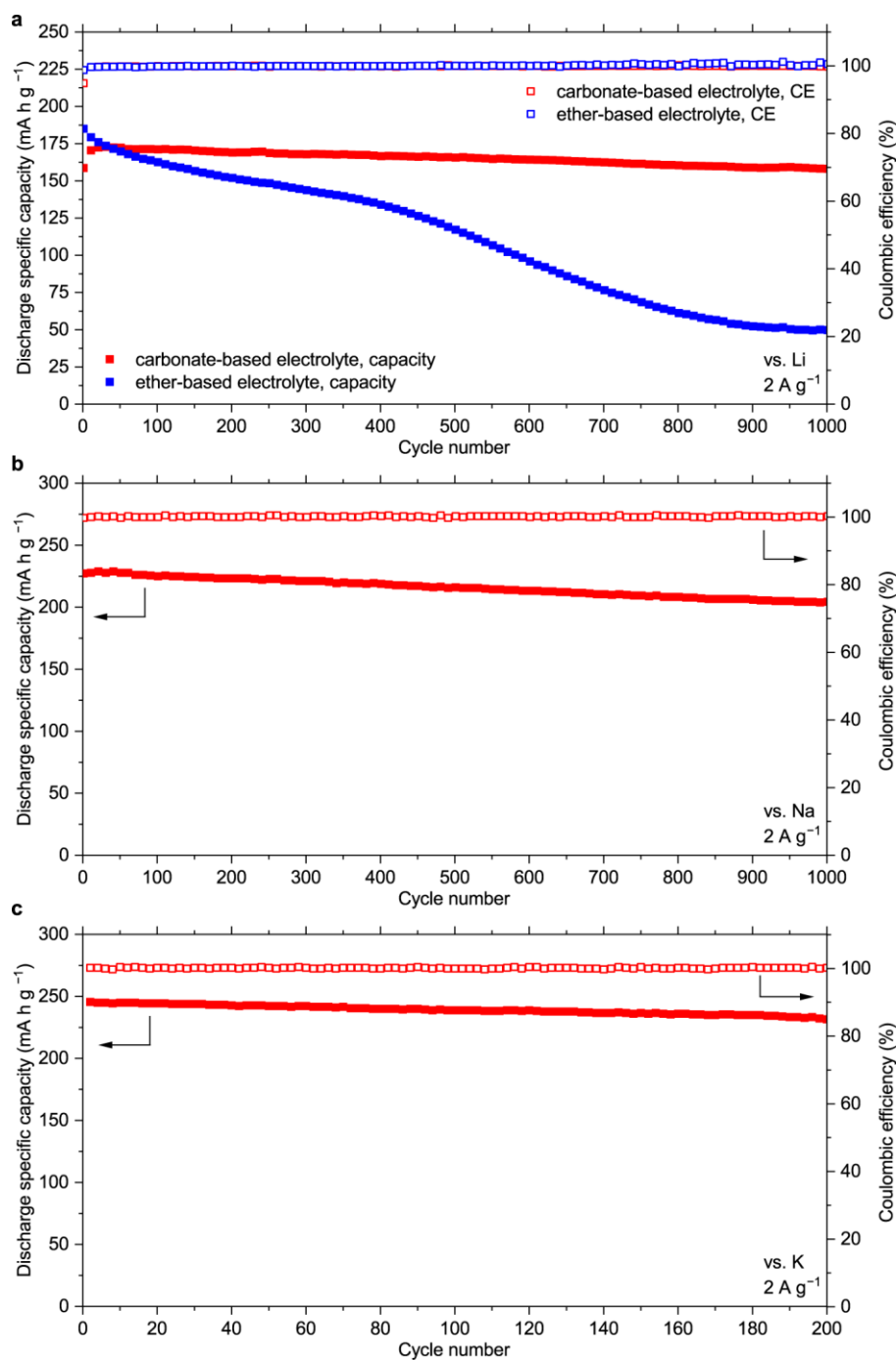


Figure 33. Cycling stability of **NiTiB** in Li-based (a), Na-based (b) and K-based (c) cells at 2 A g⁻¹.

In contrast to **CuTiB**, **NiTiB** exhibited distinct features in the charge-discharge profiles. In the Li-based cells, the charge-discharge curves had a sloping plateau at ~1.2-1.4 V vs. Li⁺/Li (Figure 29). The curves for the Na-based and K-based cells had well-

defined plateaus at higher potentials and sloping regions at lower potentials (Figure 30). These data are in agreement with the cyclic voltammetry profiles shown in Figure 34. In the lithium-based cells, two sets of closely located peaks at $\sim 1.2\text{-}1.4$ V vs. Li^+/Li (O1/R1 and O2/R2) could be observed. For the sodium-based cells, two sets of peaks were also present, but they were more separated; the peaks at higher potentials (O1/R1) were sharp and the other peaks (O2/R2) were much broader. A similar pattern was observed for the potassium-based cells, but in this case, several sets of peaks were observed in the region of lower potentials (<1.3 V vs. K^+/K).

CV peak profiles for the Li-based cell are typical for diffusion-controlled intercalation.¹⁵⁷ For Na- and K-based systems, the features at higher potentials (O1/R1) are sharp and have a pronounced voltage gap, indicating nucleation control.¹⁵⁷ At the same time, the features at lower potentials (O2/R2 for the Na-based cells and O3/R3 for the K-based cells) have small peak-to-peak separations (<30 mV at 0.2 mV s⁻¹, see Figure 35) and broad profiles, which are attributes of pseudocapacitive processes.⁵⁹ Another indicator of pseudocapacitance is almost linear dependence of the peak current on the potential scan rate (Figure 34h, i).⁵⁹

As discussed in section 2.1.1, there are two main types of pseudocapacitance for energy storage materials, namely redox pseudocapacitance (surface pseudocapacitance) and intercalation pseudocapacitance (Figure 3b, c). If the pseudocapacitance of the low-potential features was surface-confined, the O1/R1 features would be pseudocapacitive or would have much higher integral intensities. However, the O1/R1 peaks have a signature of “battery-like” bulk processes, and the capacities of the high- and low-potential regions are comparable. Therefore, it appears that there is intercalation pseudocapacitance at low potentials in the Na- and K-based systems. It might be supposed that the

initial portions of the Na^+ or K^+ ions that intercalated into **NiTIB** served as “pillars”, expanding the structure and creating void channels where the rest of the ions could move freely without affecting the framework.

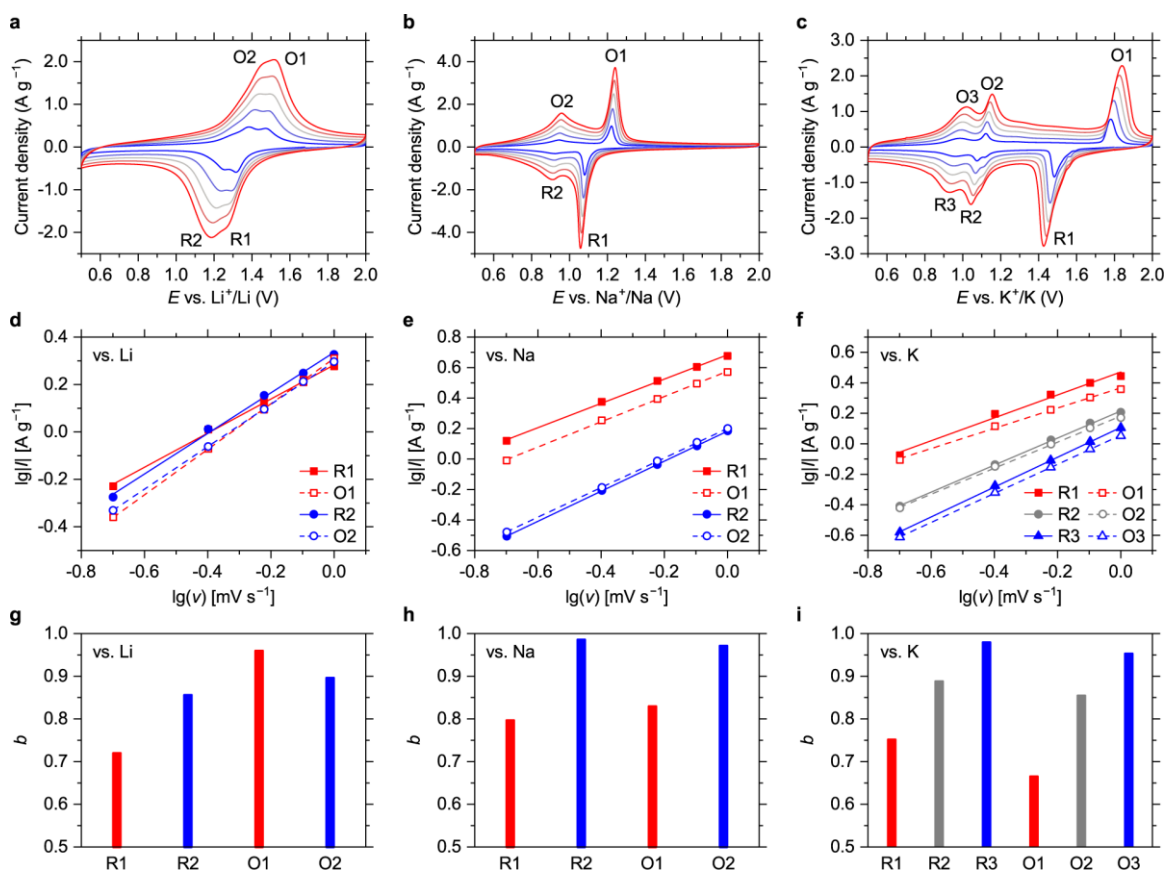


Figure 34. CV profiles for **NiTIB** in Li-based (a), Na-based (b) and K-based (c) cells, measured at scan rates of 0.2, 0.4, 0.6, 0.8 and 1 mV s^{-1} ; $\lg|I|$ vs. $\lg(v)$ dependencies for the CV peaks (d-f); *b* values of the CV peaks estimated from the linear fit (equation $\lg|I| = b \cdot \lg(v) + \lg(a)$) (g-i). Ten CV cycles at 1 mV s^{-1} in the potential ranges of 0.5-2.0 V vs. M^+/M were performed prior to the measurements to eliminate irreversible processes, after which the cells were resting for 10 minutes.

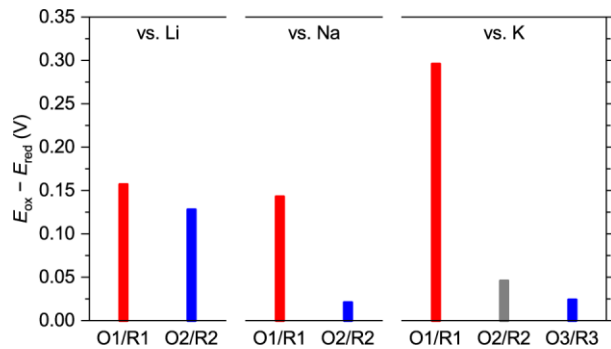


Figure 35. Potential differences for oxidation and reduction CV peaks of **NiTiB** at a scan rate of 0.2 mV s^{-1} .

NiTiB might be considered a promising alternative to widely popular lithium titanate⁸⁰ as the anode material. While sharing the safe operation potentials, which prevent alkali metal plating, it has a ~1.5 times higher specific capacity ($>250 \text{ mA h g}^{-1}$, compared to the theoretical capacity of 175 mA h g^{-1} for LTO). Considering the densities of LTO ($2.8\text{-}2.9 \text{ g cm}^{-3}$)¹⁵⁸ and **NiTiB** (1.84 g cm^{-3}), it might be concluded that their volumetric capacities should be comparable. A major advantage of **NiTiB** is that it is universally applicable for lithium-, sodium- and potassium-ion batteries. It is currently the most advanced anode material for K-ion batteries that shares similar electrochemical properties with LTO in Li-ion cells.¹⁵⁰

5.3.2. Charge-discharge mechanisms

Charge storage mechanism of **CuTiB** as the anode material was studied using *ex situ* XPS. In the initial state, **CuTiB** electrode showed a set of peaks typical for Cu(II), with Cu2p_{3/2} signal at 934.4 eV and strong satellites at 938-948 eV (Figure 36a).¹⁴⁰ An additional peak at 932.3 eV corresponds to Cu(I),¹⁴⁰ which is attributed to Cu₂O impurity detected by XRD (Figure 19c, section 5.1).

The content of Cu(II) decreased during lithiation, which is evident from the spectra of the electrodes discharged to 1.5 V and 0.8 V vs. Li⁺/Li (Figure 36a). For the

electrode discharged to 0.8 V, a single peak with no apparent satellites was observed, which indicates that reduction of Cu(II) to Cu(I) was virtually complete. The N1s peak of **CuTIB** shifted from 399.6 eV in the initial state to 399.2 eV for the electrode discharged to 0.8 V; the same shift was observed for the sample discharged to 1.5 V (Figure 36b). Hence, it might be supposed that both copper and the ligand participate in the electrochemical processes during the lithiation.

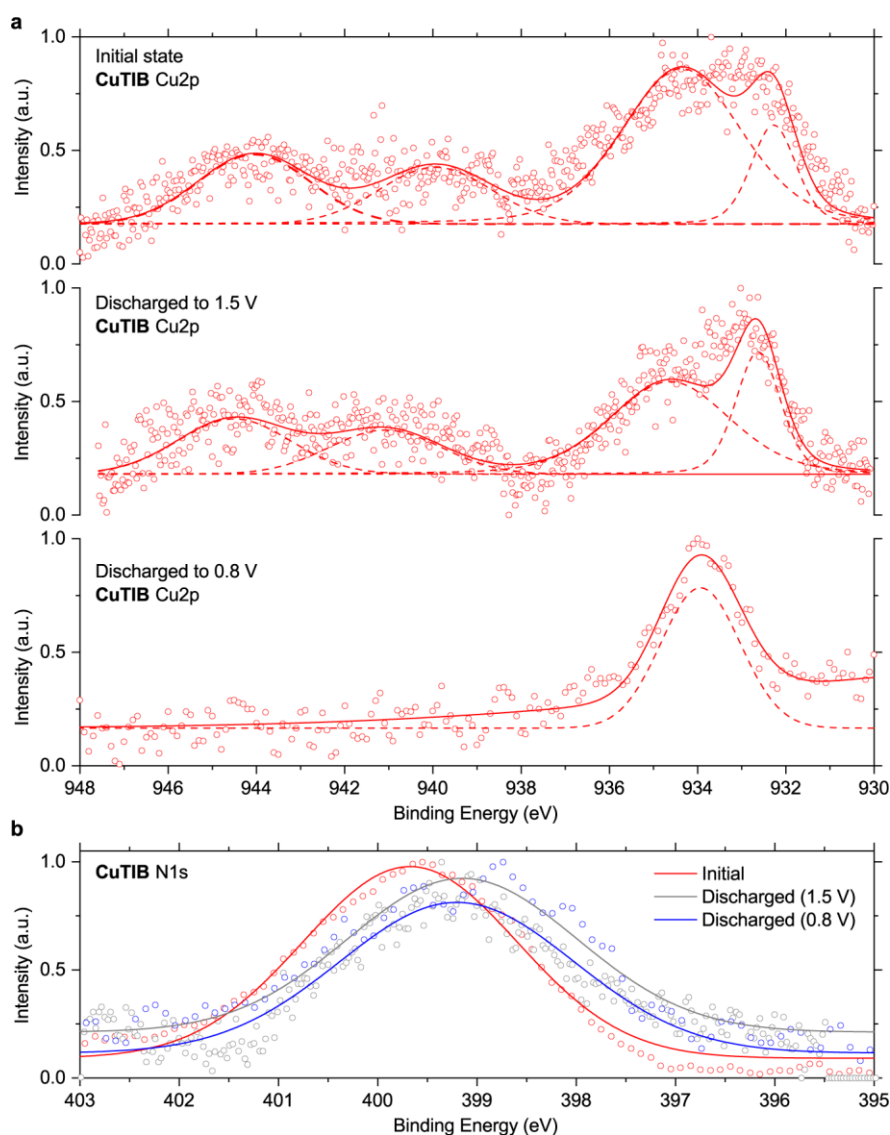


Figure 36. X-ray photoelectron spectra regions of **CuTIB** in the initial and reduced states: Cu2p regions (a) and N1s regions (b).

For **NiTIB** as the anode material, the experimental capacities in all types of cells were close to the theoretical capacity for two-electron reduction of the ligands (278 mA h g^{-1}). As discussed in section 5.1, the structure of **NiTIB** can be considered as a superposition of quinoid structures. It is known that the charge-discharge mechanism for organic quinoid compounds involves two-electron reduction to hydroquinone derivatives (Figure 37a), and the charge-discharge process often appears as two sets of peaks in the CV profiles.¹⁵⁹⁻¹⁶³ Basing on the structural features of **NiTIB** (quinoid nature of the ligands), its electrochemical properties (specific capacities, CV profiles) and the literature data, it could be proposed that the charge-discharge mechanism of **NiTIB** was similar to quinones (Figure 37b). Oxidation state of nickel was likely intact within the applied potential ranges ($>0.5 \text{ V vs. M}^+/\text{M}$), following the previous reports on two-dimensional analogs of **NiTIB** (see section 2.3.3).^{126, 127}

However, several points were unclear about the charge-discharge mechanisms of **NiTIB** from the experimental data. Firstly, it was unclear why additional peaks appeared in the CV profiles for the potassium-based cells, while two sets of peaks were present for Li-based and Na-based cells (Figure 34). Was the mechanism different for the K-based system on the molecular level or was the additional peak related to an extra phase transition that was not present for other types of charge carriers?

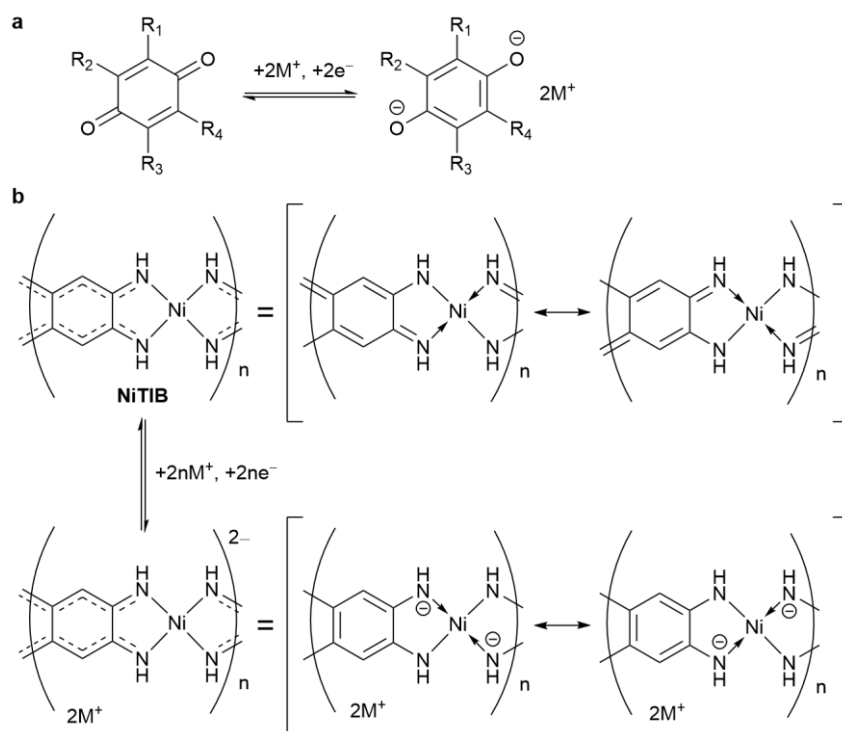


Figure 37. Redox reaction scheme for 1,4-quinones (a) and proposed overall redox reaction scheme for **NiTIB** as the anode material (b).

Secondly, it was unclear if irreversible transformations of **NiTIB** were taking place during the first cycle, which exhibited irreversible capacity losses (Figure 29c, d and Figure 30c, d), as well as distinct discharge curve profiles. Such behavior is typical for anode materials and is associated with factors such as SEI formation or macroscopic structural rearrangements,^{164, 165} but it can also indicate irreversible reduction of the electrode material itself.^{156, 166} In **NiTIB**, for example, the NH-protons should be acidic to some extent,¹⁶⁷ so these protons could be substituted by alkali metal cations, accompanied by irreversible H₂ evolution.^{167, 168} The question about the origin of the irreversible capacity is extremely important from the point of practical applications. It is crucial to understand what should be done to increase the initial Coulombic efficiency (ICE). If the low ICE originates from the SEI formation, the strategies to solve this issue

include optimizing the electrolyte composition or the binder structure, creating artificial SEI layers, or modulating the material particle size and specific surface area.^{164, 165} If the inferior ICE is caused by the transformations of the active material, this problem should be solved via molecular design, e.g., substituting the acidic protons with methyl groups.

The charge-discharge mechanism of **NiTIB** in the K-based cells was studied using *ex situ* XPS. For C1s spectra, contributions from C=N and C-N of the polymer¹²⁹ could be distinguished along with C-O/CO₂ groups of sodium carboxymethyl cellulose binder and C-C/C-H groups of the carbon and binder additives¹⁶⁹⁻¹⁷¹ (Figure 38a). In the discharged state, the contribution from C=N groups was lower compared to the discharged state, which suggests the reduction of the ligand upon potassiation.¹²⁹

In the Ni2p spectra regions (Figure 38b), a shift to lower binding energies was observed upon discharge, which was due to the increased negative charge on the polymer backbone. However, there was no evidence of Ni(II) transition to lower oxidation states. In the discharged state, the binding energy for Ni2p_{3/2} was 854.2 eV, which is characteristic for Ni(II).¹⁷² In the charged state, satellite structure giving signals at ~863 and ~880 eV was observed in Ni2p spectrum (Figure 38b). These features were previously reported for pristine **NiTIB**¹²⁹ and might arise from a charge transfer between nickel and the ligand.¹⁷²

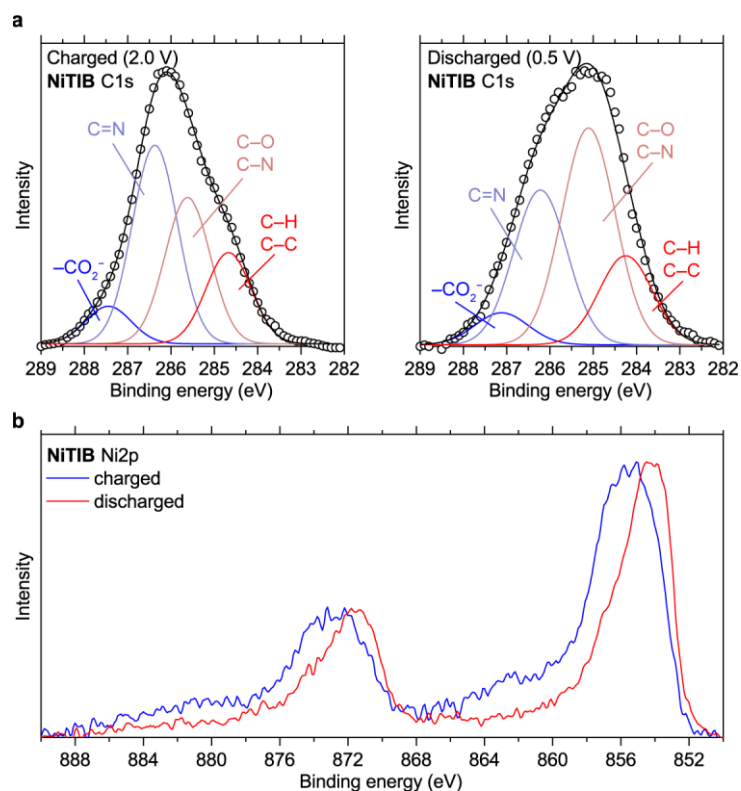


Figure 38. *Ex situ* XPS profiles for **NiTIB**-based electrodes cycled in potassium-based cells: C1s (a) and Ni2p (b) spectra regions for the charged and discharged states. Experimental data points for (a) are shown in circles, overall fit curves are shown as black lines.

To study the structural transformations of **NiTIB** during charging-discharging, *operando* and *ex situ* powder XRD measurements were carried out. As shown in Figure 39, the XRD profiles of **NiTIB** changed only slightly upon lithiation/delithiation. The most prominent shift was observed for the peak at 2θ of $\sim 24^\circ$ ($d \sim 3.7 \text{ \AA}$). Two regions of XRD pattern evolution might be observed during the charge-discharge processes. For the first region, almost no changes occurred, with the intensity of the $\sim 24^\circ$ signal slightly decreasing. For the second region, the peaks at 2θ of $\sim 20.7^\circ$ ($d \sim 4.3 \text{ \AA}$) and $\sim 29.3^\circ$ ($d \sim 3.0 \text{ \AA}$) shifted slightly, the signal at $\sim 24^\circ$ shifted to $\sim 24.5^\circ$ and became significantly less intensive. The second step took place when **NiTIB** was roughly halfway

lithiated (~ 1 Li^+ ion per repeating unit). Because the XRD peaks of **NiTIB** were wide and the peak positions shifted slightly, it is hard to determine at this point if the second stage occurred via a solid solution mechanism or if it was a two-phase transition.

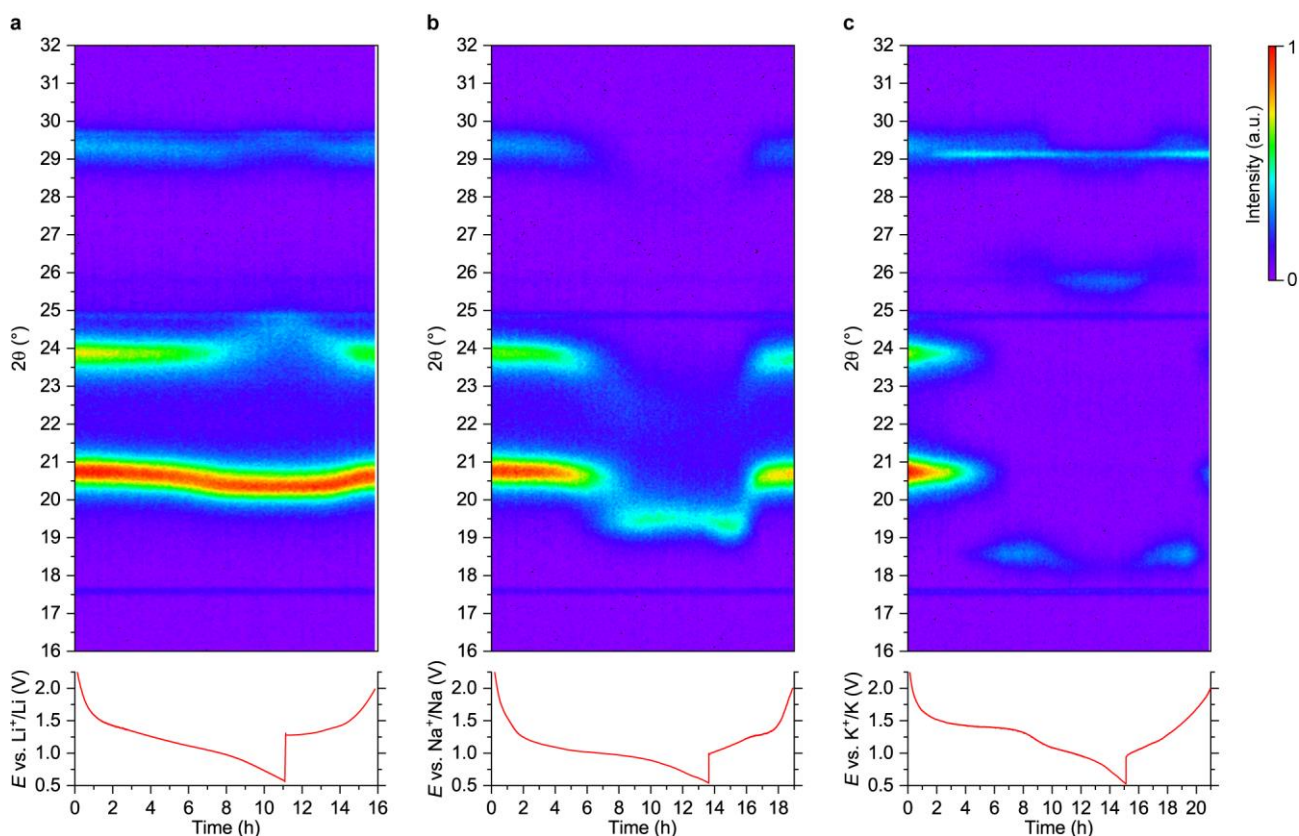


Figure 39. Intensity maps for *operando* XRD patterns of **NiTIB** during galvanostatic charge-discharge in Li-based (a), Na-based (b) and K-based (c) cells, measured with $\text{CuK}\alpha$ radiation. Charge-discharge profiles of the cells are plotted below.

In contrast, it is clearly seen that a two-phase transition took place in the sodium-based system. When **NiTIB** was half-discharged (~ 1 Na^+ ion per repeating unit), the peaks of the initial phase disappeared completely, and a peak at 2θ of $\sim 19.3^\circ$ ($d \sim 4.6$ Å) appeared. Upon further sodiation, the position of this peak was almost constant. For the potassium-based cell, two two-phase transitions were observed, occurring when the number of K^+ per repeating unit was ~ 0.7 or ~ 1.4 . During the first transition, a peak at

$\sim 18.5^\circ$ ($d \sim 4.8 \text{ \AA}$) appeared, and after the second transition a signal at $\sim 26.5^\circ$ ($d \sim 3.4 \text{ \AA}$) emerged. A narrow peak observed at 2θ of $\sim 29^\circ$ ($d \sim 3.1 \text{ \AA}$) corresponds to potassium fluoride forming upon the SEI formation.

Ex situ XRD patterns measured over a wide range of 2θ (Figure 40) showed that structure of the lithiated **NiTiB** was similar to the pristine material, while the changes that occurred after sodiation and potassiation were significant. This is in agreement with the *operando* experiments and is expectable because larger cations generally lead to more substantial structural rearrangements. For the sodiated and potassiated samples, the peaks of metal fluorides were observed, which should be originating from the SEI layers.

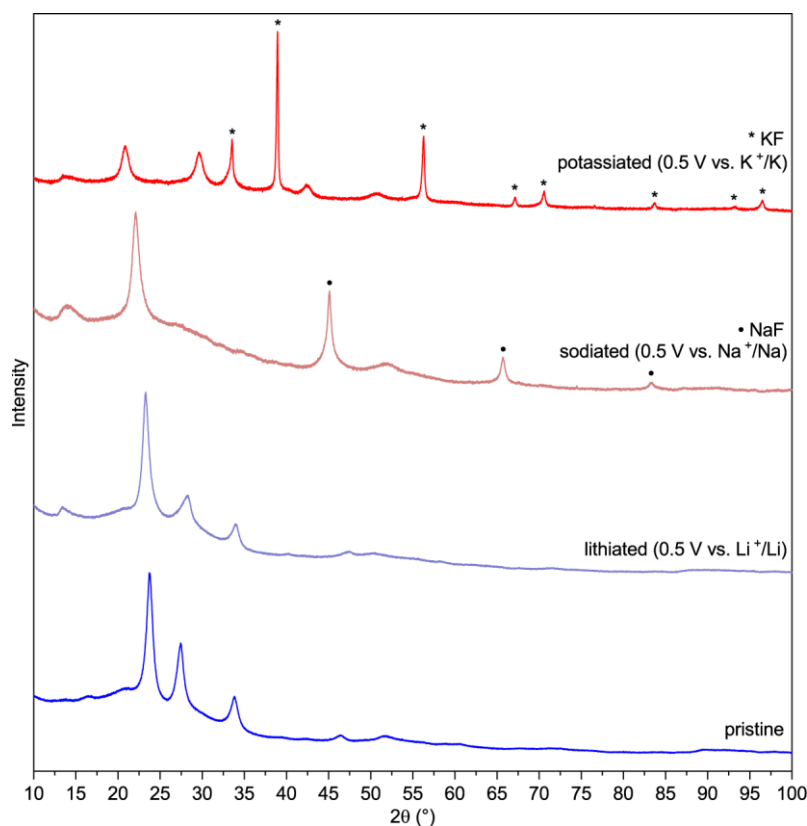


Figure 40. *Ex situ* XRD patterns for discharged and pristine **NiTiB**, measured with $\text{CoK}\alpha 1$ radiation ($\lambda = 1.78892 \text{ \AA}$).

The cyclic voltammetry features of **NiTIB** (discussed in section 5.3.1) can be explained using the data from the *operando* XRD. Additional peaks in the CV profiles for the K-based cells were related to an extra phase transition, which was not observed for the Li-based and Na-based cells. On the molecular level, the charge storage mechanisms of **NiTIB** with different charge carriers (Li^+ , Na^+ , K^+) might be considered similar, which is typical for compounds with redox-active organic moieties.³⁸

From the *operando* XRD data, it is seen that the structural rearrangements of **NiTIB** are reversible, with signals of the initial phase reappearing upon reoxidation. Therefore, it might be supposed no irreversible reactions, such as NH-proton substitution, took place on the molecular level. To confirm reversibility of the **NiTIB** reduction, *operando* Raman spectroscopy measurements were performed. Initially, an infrared laser ($\lambda = 780 \text{ nm}$) was selected to reduce the intensity of fluorescence and signals from the electrolyte, carbon black and SEI components. The intensity of **NiTIB** spectra dropped approximately by an order of magnitude upon reduction and restored after reoxidation (Figure 41a, c, e). Importantly, spectra of the reoxidized material after the first and the second cycles were nearly identical to the initial one (Figure 41b, d, f). Relative intensities of the peaks varied only slightly, and changes of the Raman shifts were below 2 cm^{-1} .

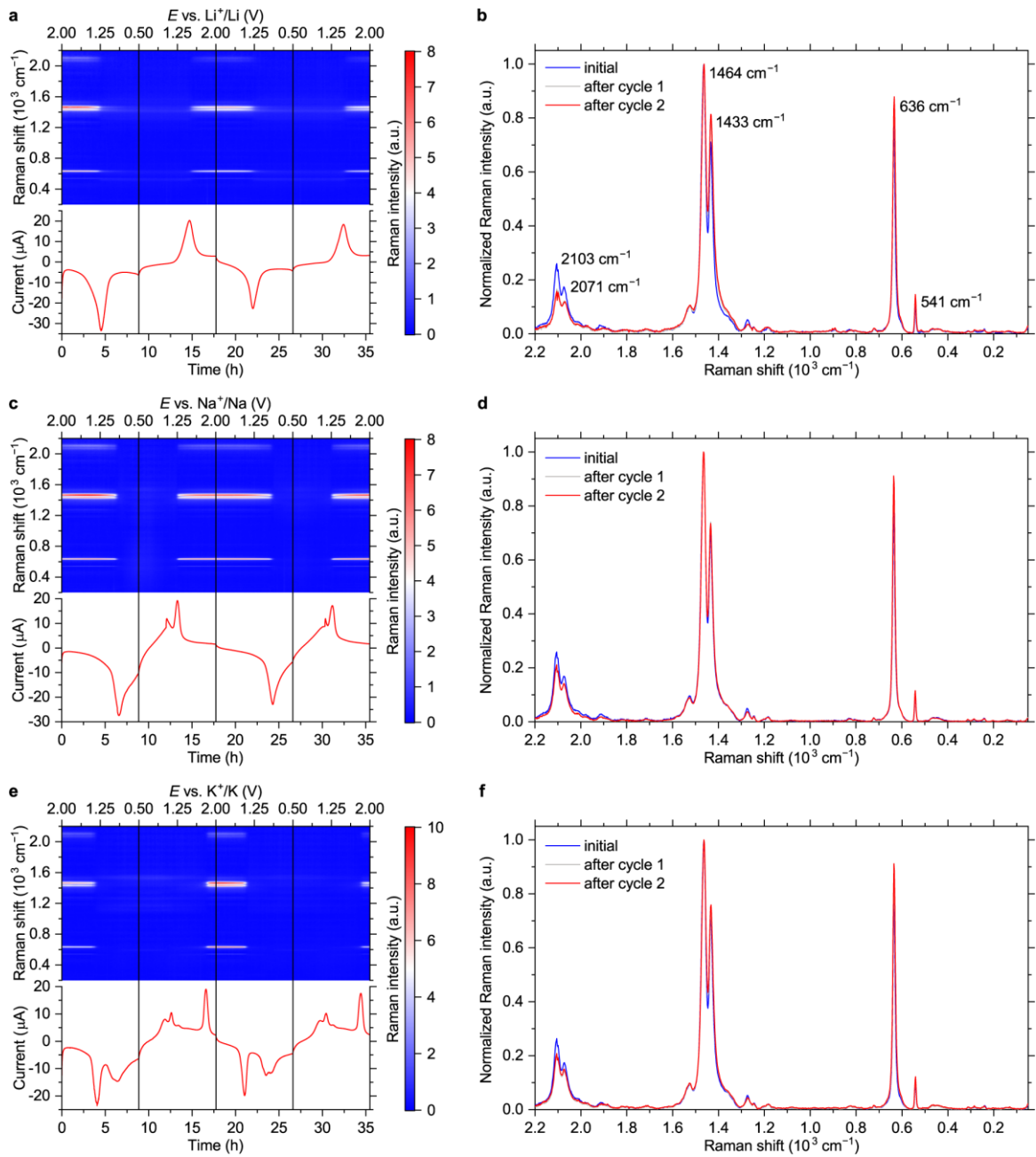


Figure 41. Evolution of Raman spectra of NiTiB measured with an infrared laser ($\lambda = 780 \text{ nm}$) for Li-based (a, b), Na-based (c, d) and K-based (e, f) cells: Raman intensity maps and current vs. time (vs. potential) profiles (a, c, e); normalized initial spectrum compared to the spectra after the 1st and the 2nd cycles (b, d, f).

According to these data, no irreversible transformations took place for NiTiB in Li-, Na- or K-ion batteries in the potential range 0.5–2.0 V vs. M^+/M , which

disproves the initial hypothesis about irreversible NH-proton substitution. Irreversible capacity losses should be originating from the SEI formation, and this issue can be solved by tuning the electrolyte or electrode composition, creating artificial SEI layers, or modulating the particle size of **NiTIB**.^{164, 165}

Raman intensity is a function of difference between the energy of the laser photons and the energy of electronic transitions.¹⁷³ If this difference is small or zero, the intensity might increase dramatically, which is the basis for resonance Raman spectroscopy.¹⁷³ Since **NiTIB** is a narrow-gap semiconductor that absorbs near-infrared light,⁸⁸ it can be concluded that its resonance Raman spectra were measured when the infrared laser ($\lambda = 780$ nm) was selected.

To better understand the electronic structure evolution, UV-Vis-NIR spectra were acquired. While there were no issues with measuring the pristine **NiTIB**, studying the reduced states was more challenging. Measurements of the discharged electrodes could give ambiguous results because of absorption by carbon black,^{174, 175} and separating contributions from the two materials correctly would be difficult. Electrochemical reduction of **NiTIB** without conductive fillers was problematic because of its low electronic conductivity.¹⁴⁷ For this reason, chemical reduction of **NiTIB** films was carried out using excessive amount of potassium naphthalenide (see Experimental section). Naphthalenides have low oxidation potentials (~ 0.5 V vs. Li^+/Li),¹⁷⁶ which makes them suitable for complete reduction of **NiTIB**. This approach has recently been shown applicable for a wide range of materials.¹⁷⁷⁻¹⁷⁹ Successful chemical reduction was confirmed by Raman spectroscopy (Figure A8).

As shown in Figure 42, pristine **NiTIB** had a broad absorption feature with the onset at ~ 600 nm and maximum at ~ 950 nm. Substantial absorption was observed at

780 nm, which should induce resonance Raman effect at this wavelength. After the reduction, this broad peak disappeared, and the spectrum showed a sloping absorption feature at shorter wavelengths (<800 nm). This change is an indicator of the bandgap increase, which explains why the infrared Raman intensities decreased by an order of magnitude upon reduction. Similar trends in the UV-Vis spectra were previously reported for a low-molecular analog of **NiTIB**.¹⁸⁰

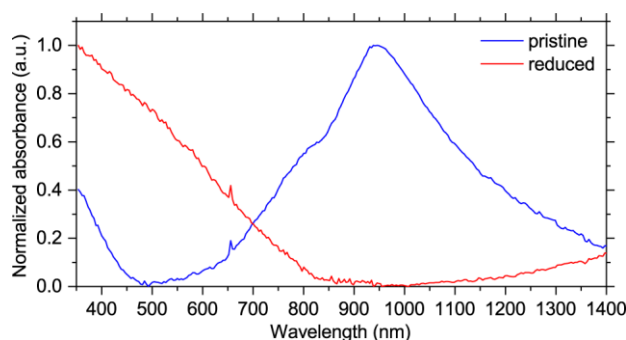


Figure 42. UV-Vis-NIR spectra of **NiTIB** before and after chemical reduction.

To gain more information about the structure evolution upon charging-discharging, the laser wavelength was switched to 532 nm. As shown in Figure 43, Raman intensity of the reduced states increased dramatically with the green laser.

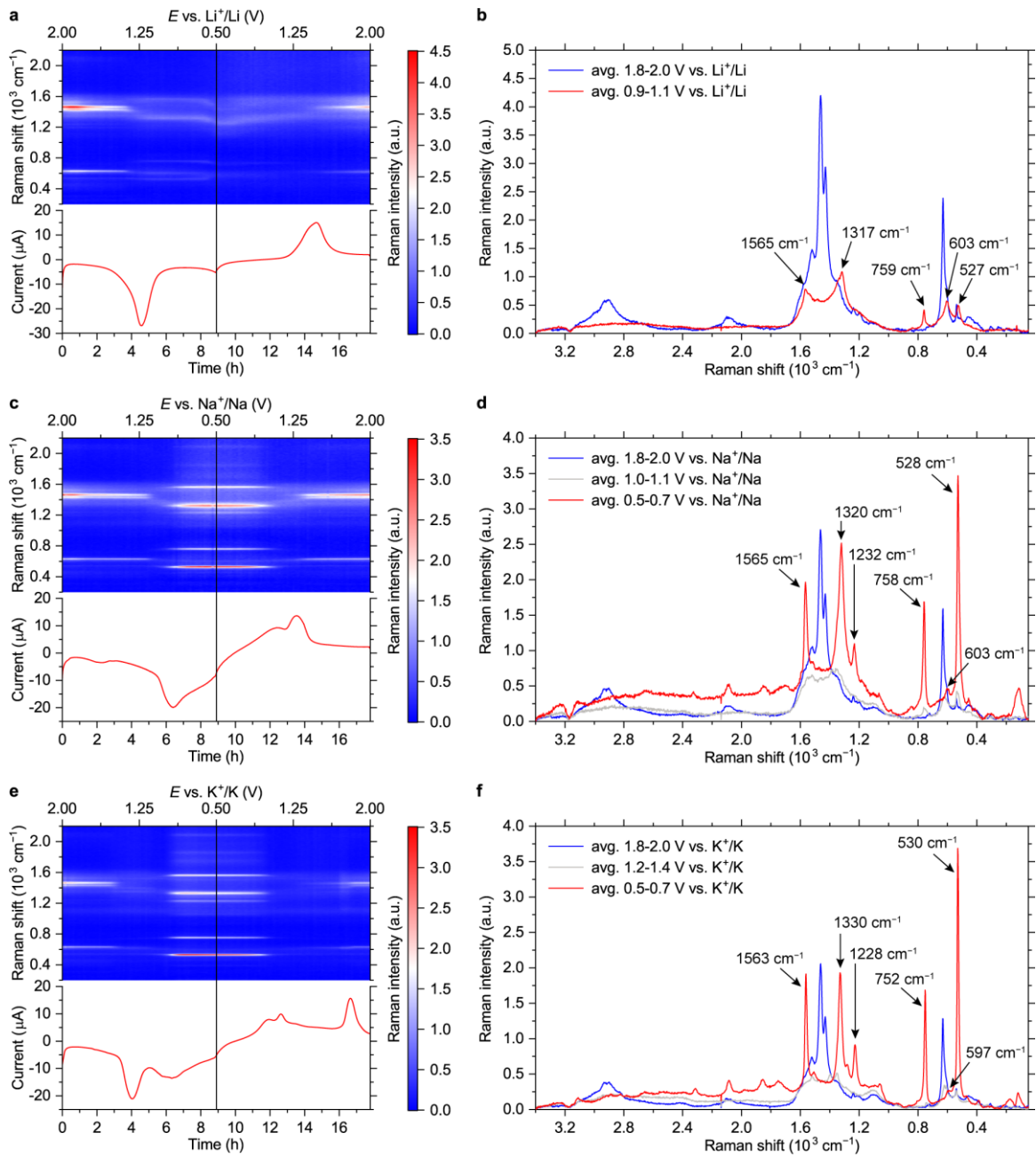


Figure 43. Evolution of Raman spectra of **NiTiB** measured with a green laser ($\lambda = 532$ nm) for Li-based (a, b), Na-based (c, d) and K-based (e, f) cells: Raman intensity maps and current vs. time (vs. potential) profiles (a, c, e); averaged Raman spectra for selected potential ranges during the initial discharge (b, d, f).

Spectra of the fully lithiated, sodiated and potassiated states had similar patterns, with characteristic peaks at $1563\text{--}1565\text{ cm}^{-1}$, $1317\text{--}1330\text{ cm}^{-1}$, $752\text{--}759\text{ cm}^{-1}$, 597--

603 cm^{-1} , and 527–530 cm^{-1} (Figure 43b, d, f). Similarities of these spectra (especially pronounced for the Na- and K-based systems) indicate that the charge storage mechanisms were similar on the molecular level. This confirms that appearance of the third set of peaks for the K-based cells (Figure 34c) was caused by an additional phase transition rather than some unusual reduction of Ni^{2+} or the ligands which was not occurring in the Li- and Na-based batteries.

Although the spectra of fully lithiated, sodiated and potassiated materials were similar, certain variability of both Raman shifts and intensities was present. The most obvious difference was observed for the Li-based cells, where the spectra were less structured and intensive compared to the Na- and K-based systems. The distinctions should be associated with the differences of local environments of the macromolecules.

Chapter 6. Conclusions

In this work, nickel- and copper-based coordination compounds derived from 1,2,4,5-benzenetetraamine were synthesized, characterized using a set of physicochemical methods, and studied as active electrode materials for non-aqueous energy storage devices that use alkali metal ions as charge carriers. The main conclusions are the following:

- While the Ni-based material has a well-defined structure and was crystalline, the Cu-based material is disordered, contains impurities, and apparently has lower degree of polymerization and higher concentration of defects. The possible reason for this is partial reduction of Cu^{2+} by benzenetetraamine, which takes place during the synthesis.
- The materials are redox-active in lithium-based cells in the potential ranges of 1.5-4.1 or 2.0-3.8 V vs. Li^+/Li . Higher specific capacities are observed for the ball-milled copper-based material (up to 262 mA h g^{-1}). According to XPS, it can accommodate negative and positive charges at low and high cell potentials, respectively. However, the compounds exhibit inferior cycling stability, which limits their applicability as materials for positive electrodes.
- In the potential range of 0.8-2.0 V vs. Li^+/Li , the Cu-based material shows moderate specific capacity (70 mA h g^{-1} after subtracting the contribution from carbon black) and moderate cycling stability at low current density (50 mA g^{-1}). Upon lithiation, Cu(II) reduces to Cu(I), and the ligands are redox-active as well.
- The Ni-based compound shows impressive performance in the potential ranges of 0.5-2.0 V vs. M^+/M ($\text{M} = \text{Li, Na, K}$), making it a promising material for

lithium-ion, sodium-ion and potassium-ion batteries. The material exhibits high specific capacities (up to 265 mA h g^{-1} after subtracting the contribution from carbon black), high-rate capabilities (up to 5 A g^{-1} , charging or discharging in $<2 \text{ min}$) and cycling stability (capacity fading rate of $<0.03\%$ per cycle). High areal capacities (up to $2.73 \text{ mA h cm}^{-2}$) are demonstrated. The average delithiation, desodiation and depotassiation potentials are $\sim 1.35 \text{ V vs. Li}^+/\text{Li}$, $\sim 1.1 \text{ V vs. Na}^+/\text{Na}$ and $\sim 1.35 \text{ V vs. K}^+/\text{K}$, respectively. The material might be considered an attractive alternative to lithium titanate, which has higher capacity and is compatible with various charge carriers.

- On the molecular level, the charge storage mechanism of the Ni-based polymer is similar for Li-based, Na-based and K-based systems, involving reversible two-electron reduction of the ligands. Theoretical capacity of the material is 278 mA h g^{-1} .
- Differences in the charge-discharge curve profiles and CV profiles of the Ni-based material in Li-, Na- and K-based cells are associated with different crystal structure rearrangements during the charge-discharge processes.
- When partially reduced, the Ni-based material exhibits intercalation pseudocapacitance, i.e., fast bulk faradaic reactions, in the Na- and K-based batteries.

Bibliography

- (1) Li, M.; Lu, J.; Chen, Z.; Amine, K., 30 Years of Lithium-Ion Batteries. *Adv. Mater.* **2018**, *30* (33), 1800561.
- (2) Soloveichik, G. L., Flow Batteries: Current Status and Trends. *Chem. Rev.* **2015**, *115* (20), 11533-11558.
- (3) Simon, P.; Gogotsi, Y., Materials for electrochemical capacitors. *Nat. Mater.* **2008**, *7* (11), 845-854.
- (4) Park, M.; Ryu, J.; Wang, W.; Cho, J., Material design and engineering of next-generation flow-battery technologies. *Nat. Rev. Mater.* **2016**, *2* (1), 16080.
- (5) Wang, G.; Zhang, L.; Zhang, J., A review of electrode materials for electrochemical supercapacitors. *Chem. Soc. Rev.* **2012**, *41* (2), 797-828.
- (6) Shao, Y.; El-Kady, M. F.; Sun, J.; Li, Y.; Zhang, Q.; Zhu, M.; Wang, H.; Dunn, B.; Kaner, R. B., Design and Mechanisms of Asymmetric Supercapacitors. *Chem. Rev.* **2018**, *118* (18), 9233-9280.
- (7) Kirubakaran, A.; Jain, S.; Nema, R. K., A review on fuel cell technologies and power electronic interface. *Renew. Sustain. Energy Rev.* **2009**, *13* (9), 2430-2440.
- (8) Whittingham, M. S., Lithium Batteries and Cathode Materials. *Chem. Rev.* **2004**, *104* (10), 4271-4302.
- (9) Van Noorden, R., The rechargeable revolution: A better battery. *Nature* **2014**, *507* (7490), 26.
- (10) Schmuch, R.; Wagner, R.; Hörpel, G.; Placke, T.; Winter, M., Performance and cost of materials for lithium-based rechargeable automotive batteries. *Nat. Energy* **2018**, *3* (4), 267-278.

- (11) Kamat, P. V., Lithium-Ion Batteries and Beyond: Celebrating the 2019 Nobel Prize in Chemistry – A Virtual Issue. *ACS Energy Lett.* **2019**, *4* (11), 2757-2759.
- (12) Goodenough, J. B.; Park, K.-S., The Li-Ion Rechargeable Battery: A Perspective. *Journal of the American Chemical Society* **2013**, *135* (4), 1167-1176.
- (13) Turcheniuk, K.; Bondarev, D.; Singhal, V.; Yushin, G., Ten years left to redesign lithium-ion batteries. *Nature* **2018**, *559*, 467-470.
- (14) Kabir, M. M.; Demirocak, D. E., Degradation mechanisms in Li-ion batteries: a state-of-the-art review. *Int. J. Energy Res.* **2017**, *41* (14), 1963-1986.
- (15) Woody, M.; Arbabzadeh, M.; Lewis, G. M.; Keoleian, G. A.; Stefanopoulou, A., Strategies to limit degradation and maximize Li-ion battery service lifetime - Critical review and guidance for stakeholders. *J. Energy Storage* **2020**, *28*, 101231.
- (16) Logan, E. R.; Dahn, J. R., Electrolyte Design for Fast-Charging Li-Ion Batteries. *Trends Chem.* **2020**, *2* (4), 354-366.
- (17) Tarascon, J. M.; Armand, M., Issues and challenges facing rechargeable lithium batteries. *Nature* **2001**, *414* (6861), 359-367.
- (18) Chung, S.-H.; Manthiram, A., Current Status and Future Prospects of Metal–Sulfur Batteries. *Adv. Mater.* **2019**, *31* (27), 1901125.
- (19) Chen, S.; Dai, F.; Cai, M., Opportunities and Challenges of High-Energy Lithium Metal Batteries for Electric Vehicle Applications. *ACS Energy Lett.* **2020**, *5* (10), 3140-3151.
- (20) Krauskopf, T.; Richter, F. H.; Zeier, W. G.; Janek, J., Physicochemical Concepts of the Lithium Metal Anode in Solid-State Batteries. *Chem. Rev.* **2020**, *120* (15), 7745-7794.

- (21) Jung, J.-W.; Cho, S.-H.; Nam, J. S.; Kim, I.-D., Current and future cathode materials for non-aqueous Li-air (O₂) battery technology – A focused review. *Energy Storage Mater.* **2020**, *24*, 512-528.
- (22) Liu, T.; Vivek, J. P.; Zhao, E. W.; Lei, J.; Garcia-Araez, N.; Grey, C. P., Current Challenges and Routes Forward for Nonaqueous Lithium–Air Batteries. *Chem. Rev.* **2020**, *120* (14), 6558-6625.
- (23) Martin, G.; Rentsch, L.; Höck, M.; Bertau, M., Lithium market research – global supply, future demand and price development. *Energy Storage Mater.* **2017**, *6*, 171-179.
- (24) Battistel, A.; Palagonia, M. S.; Brogioli, D.; La Mantia, F.; Trócoli, R., Electrochemical Methods for Lithium Recovery: A Comprehensive and Critical Review. *Adv. Mater.* **2020**, *32* (23), 1905440.
- (25) Yabuuchi, N.; Kubota, K.; Dahbi, M.; Komaba, S., Research Development on Sodium-Ion Batteries. *Chem. Rev.* **2014**, *114* (23), 11636-11682.
- (26) Slater, M. D.; Kim, D.; Lee, E.; Johnson, C. S., Sodium-Ion Batteries. *Adv. Funct. Mater.* **2013**, *23* (8), 947-958.
- (27) Gourley, S. W. D.; Or, T.; Chen, Z., Breaking Free from Cobalt Reliance in Lithium-Ion Batteries. *iScience* **2020**, *23* (9), 101505.
- (28) Vaalma, C.; Buchholz, D.; Weil, M.; Passerini, S., A cost and resource analysis of sodium-ion batteries. *Nat. Rev. Mater.* **2018**, *3* (4), 18013.
- (29) Zhang, W.; Liu, Y.; Guo, Z., Approaching high-performance potassium-ion batteries via advanced design strategies and engineering. *Sci. Adv.* **2019**, *5* (5), eaav7412.

- (30) Niro, M.; Kisaburo, U.; Zen'ichi, T., Standard Potentials of Alkali Metals, Silver, and Thallium Metal/Ion Couples in N,N'-Dimethylformamide, Dimethyl Sulfoxide, and Propylene Carbonate. *Bull. Chem. Soc. Jpn.* **1974**, *47* (4), 813-817.
- (31) Komaba, S.; Hasegawa, T.; Dahbi, M.; Kubota, K., Potassium intercalation into graphite to realize high-voltage/high-power potassium-ion batteries and potassium-ion capacitors. *Electrochem. Commun.* **2015**, *60*, 172-175.
- (32) Ge, P.; Fouletier, M., Electrochemical intercalation of sodium in graphite. *Solid State Ionics* **1988**, *28-30*, 1172-1175.
- (33) Nobuhara, K.; Nakayama, H.; Nose, M.; Nakanishi, S.; Iba, H., First-principles study of alkali metal-graphite intercalation compounds. *J. Power Sources* **2013**, *243*, 585-587.
- (34) Kubota, K.; Dahbi, M.; Hosaka, T.; Kumakura, S.; Komaba, S., Towards K-Ion and Na-Ion Batteries as “Beyond Li-Ion”. *Chem. Rec.* **2018**, *18* (4), 459-479.
- (35) Pham, T. A.; Kweon, K. E.; Samanta, A.; Lordi, V.; Pask, J. E., Solvation and Dynamics of Sodium and Potassium in Ethylene Carbonate from ab Initio Molecular Dynamics Simulations. *J. Phys. Chem. C* **2017**, *121* (40), 21913-21920.
- (36) Liang, Y.; Lai, W.-H.; Miao, Z.; Chou, S.-L., Nanocomposite Materials for the Sodium-Ion Battery: A Review. *Small* **2018**, *14* (5), 1702514.
- (37) Zuo, X.; Zhu, J.; Müller-Buschbaum, P.; Cheng, Y.-J., Silicon based lithium-ion battery anodes: A chronicle perspective review. *Nano Energy* **2017**, *31*, 113-143.
- (38) Schon, T. B.; McAllister, B. T.; Li, P.-F.; Seferos, D. S., The rise of organic electrode materials for energy storage. *Chem. Soc. Rev.* **2016**, *45* (22), 6345-6404.
- (39) Muench, S.; Wild, A.; Friebe, C.; Häupler, B.; Janoschka, T.; Schubert, U. S., Polymer-Based Organic Batteries. *Chem. Rev.* **2016**, *116* (16), 9438-9484.

- (40) Zhang, H.; Li, C.; Eshetu, G. G.; Laruelle, S.; Grugeon, S.; Zaghib, K.; Julien, C.; Mauger, A.; Guyomard, D.; Rojo, T.; Gisbert-Trejo, N.; Passerini, S.; Huang, X.; Zhou, Z.; Johansson, P.; Forsyth, M., From Solid-Solution Electrodes and the Rocking-Chair Concept to Today's Batteries. *Angew. Chem. Int. Ed.* **2020**, *59* (2), 534-538.
- (41) Nitta, N.; Wu, F.; Lee, J. T.; Yushin, G., Li-ion battery materials: present and future. *Mater. Today* **2015**, *18* (5), 252-264.
- (42) Lee, B.; Paek, E.; Mitlin, D.; Lee, S. W., Sodium Metal Anodes: Emerging Solutions to Dendrite Growth. *Chem. Rev.* **2019**, *119* (8), 5416-5460.
- (43) Zhang, C.; Huang, K., A Comprehensive Review on the Development of Solid-State Metal–Air Batteries Operated on Oxide-Ion Chemistry. *Adv. Energy Mater.* **2021**, *11* (2), 2000630.
- (44) Ding, J.; Zhang, H.; Fan, W.; Zhong, C.; Hu, W.; Mitlin, D., Review of Emerging Potassium–Sulfur Batteries. *Adv. Mater.* **2020**, *32* (23), 1908007.
- (45) Xing, M.; Zhao, Z. Z.; Zhang, Y. J.; Zhao, J. W.; Cui, G. L.; Dai, J. H., Advances and issues in developing metal-iodine batteries. *Mater. Today Energy* **2020**, *18*, 100534.
- (46) Wang, M.; Tang, Y., A Review on the Features and Progress of Dual-Ion Batteries. *Adv. Energy Mater.* **2018**, *8* (19), 1703320.
- (47) Placke, T.; Heckmann, A.; Schmuck, R.; Meister, P.; Beltrop, K.; Winter, M., Perspective on Performance, Cost, and Technical Challenges for Practical Dual-Ion Batteries. *Joule* **2018**, *2* (12), 2528-2550.
- (48) Chen, S.; Kuang, Q.; Fan, H. J., Dual-Carbon Batteries: Materials and Mechanism. *Small* **2020**, *16* (40), 2002803.

- (49) Zhang, L. L.; Zhao, X. S., Carbon-based materials as supercapacitor electrodes. *Chem. Soc. Rev.* **2009**, *38* (9), 2520-2531.
- (50) Jiang, Y.; Liu, J., Definitions of Pseudocapacitive Materials: A Brief Review. *Energy Environ. Mater.* **2019**, *2* (1), 30-37.
- (51) Conway, B. E., *Electrochemical supercapacitors: scientific fundamentals and technological applications*. Springer Science & Business Media: 2013.
- (52) Hu, L.; Chen, W.; Xie, X.; Liu, N.; Yang, Y.; Wu, H.; Yao, Y.; Pasta, M.; Alshareef, H. N.; Cui, Y., Symmetrical MnO₂-Carbon Nanotube-Textile Nanostructures for Wearable Pseudocapacitors with High Mass Loading. *ACS Nano* **2011**, *5* (11), 8904-8913.
- (53) Wen, S.; Lee, J.-W.; Yeo, I.-H.; Park, J.; Mho, S.-i., The role of cations of the electrolyte for the pseudocapacitive behavior of metal oxide electrodes, MnO₂ and RuO₂. *Electrochim. Acta* **2004**, *50* (2), 849-855.
- (54) Simon, P.; Gogotsi, Y.; Dunn, B., Where Do Batteries End and Supercapacitors Begin? *Science* **2014**, *343* (6176), 1210-1211.
- (55) Aricò, A. S.; Bruce, P.; Scrosati, B.; Tarascon, J.-M.; van Schalkwijk, W., Nanostructured materials for advanced energy conversion and storage devices. *Nat. Mater.* **2005**, *4* (5), 366-377.
- (56) Augustyn, V.; Come, J.; Lowe, M. A.; Kim, J. W.; Taberna, P.-L.; Tolbert, S. H.; Abruña, H. D.; Simon, P.; Dunn, B., High-rate electrochemical energy storage through Li⁺ intercalation pseudocapacitance. *Nat. Mater.* **2013**, *12* (6), 518-522.
- (57) Zúkalová, M.; Kalbáč, M.; Kavan, L.; Exnar, I.; Graetzel, M., Pseudocapacitive Lithium Storage in TiO₂(B). *Chem. Mater.* **2005**, *17* (5), 1248-1255.

- (58) Brezesinski, T.; Wang, J.; Tolbert, S. H.; Dunn, B., Ordered mesoporous α -MoO₃ with iso-oriented nanocrystalline walls for thin-film pseudocapacitors. *Nat. Mater.* **2010**, *9* (2), 146-151.
- (59) Augustyn, V.; Simon, P.; Dunn, B., Pseudocapacitive oxide materials for high-rate electrochemical energy storage. *Energy Environ. Sci.* **2014**, *7* (5), 1597-1614.
- (60) Herrero, E.; Buller, L. J.; Abruña, H. D., Underpotential Deposition at Single Crystal Surfaces of Au, Pt, Ag and Other Materials. *Chem. Rev.* **2001**, *101* (7), 1897-1930.
- (61) Wang, J.; Polleux, J.; Lim, J.; Dunn, B., Pseudocapacitive Contributions to Electrochemical Energy Storage in TiO₂ (Anatase) Nanoparticles. *J. Phys. Chem. C* **2007**, *111* (40), 14925-14931.
- (62) Chao, D.; Liang, P.; Chen, Z.; Bai, L.; Shen, H.; Liu, X.; Xia, X.; Zhao, Y.; Savilov, S. V.; Lin, J.; Shen, Z. X., Pseudocapacitive Na-Ion Storage Boosts High Rate and Areal Capacity of Self-Branched 2D Layered Metal Chalcogenide Nanoarrays. *ACS Nano* **2016**, *10* (11), 10211-10219.
- (63) Yu, P.; Li, C.; Guo, X., Sodium Storage and Pseudocapacitive Charge in Textured Li₄Ti₅O₁₂ Thin Films. *J. Phys. Chem. C* **2014**, *118* (20), 10616-10624.
- (64) Noori, A.; El-Kady, M. F.; Rahmanifar, M. S.; Kaner, R. B.; Mousavi, M. F., Towards establishing standard performance metrics for batteries, supercapacitors and beyond. *Chem. Soc. Rev.* **2019**, *48* (5), 1272-1341.
- (65) Tang, Y.; Zhang, Y.; Li, W.; Ma, B.; Chen, X., Rational material design for ultrafast rechargeable lithium-ion batteries. *Chem. Soc. Rev.* **2015**, *44* (17), 5926-5940.

- (66) Lu, Y.; Zhang, Q.; Li, L.; Niu, Z.; Chen, J., Design Strategies toward Enhancing the Performance of Organic Electrode Materials in Metal-Ion Batteries. *Chem* **2018**, *4* (12), 2786-2813.
- (67) Choi, S.; Kwon, T.-w.; Coskun, A.; Choi, J. W., Highly elastic binders integrating polyrotaxanes for silicon microparticle anodes in lithium ion batteries. *Science* **2017**, *357* (6348), 279-283.
- (68) Wang, H.; Fu, J.; Wang, C.; Wang, J.; Yang, A.; Li, C.; Sun, Q.; Cui, Y.; Li, H., A binder-free high silicon content flexible anode for Li-ion batteries. *Energy Environ. Sci.* **2020**, *13* (3), 848-858.
- (69) Chen, J.; Fan, X.; Li, Q.; Yang, H.; Khoshi, M. R.; Xu, Y.; Hwang, S.; Chen, L.; Ji, X.; Yang, C.; He, H.; Wang, C.; Garfunkel, E.; Su, D.; Borodin, O.; Wang, C., Electrolyte design for LiF-rich solid–electrolyte interfaces to enable high-performance micro-sized alloy anodes for batteries. *Nat. Energy* **2020**, *5* (5), 386-397.
- (70) Azam, M. A.; Safie, N. E.; Ahmad, A. S.; Yuza, N. A.; Zulkifli, N. S. A., Recent advances of silicon, carbon composites and tin oxide as new anode materials for lithium-ion battery: A comprehensive review. *J. Energy Storage* **2021**, *33*, 102096.
- (71) Yang, C.; Xin, S.; Mai, L.; You, Y., Materials Design for High-Safety Sodium-Ion Battery. *Adv. Energy Mater.* **2021**, *11* (2), 2000974.
- (72) Liu, K.; Liu, Y.; Lin, D.; Pei, A.; Cui, Y., Materials for lithium-ion battery safety. *Sci. Adv.* **2018**, *4* (6), eaas9820.
- (73) Yang, C.; Chen, J.; Ji, X.; Pollard, T. P.; Lü, X.; Sun, C.-J.; Hou, S.; Liu, Q.; Liu, C.; Qing, T.; Wang, Y.; Borodin, O.; Ren, Y.; Xu, K.; Wang, C., Aqueous Li-ion battery enabled by halogen conversion–intercalation chemistry in graphite. *Nature* **2019**, *569* (7755), 245-250.

- (74) Chen, S.; Wen, K.; Fan, J.; Bando, Y.; Golberg, D., Progress and future prospects of high-voltage and high-safety electrolytes in advanced lithium batteries: from liquid to solid electrolytes. *J. Mater. Chem. A* **2018**, *6* (25), 11631-11663.
- (75) Tan, S.; Ji, Y. J.; Zhang, Z. R.; Yang, Y., Recent Progress in Research on High-Voltage Electrolytes for Lithium-Ion Batteries. *ChemPhysChem* **2014**, *15* (10), 1956-1969.
- (76) Bommier, C.; Ji, X., Electrolytes, SEI Formation, and Binders: A Review of Nonelectrode Factors for Sodium-Ion Battery Anodes. *Small* **2018**, *14* (16), 1703576.
- (77) Zheng, F.; Kotobuki, M.; Song, S.; Lai, M. O.; Lu, L., Review on solid electrolytes for all-solid-state lithium-ion batteries. *J. Power Sources* **2018**, *389*, 198-213.
- (78) Wu, Z.; Xie, Z.; Yoshida, A.; Wang, Z.; Hao, X.; Abudula, A.; Guan, G., Utmost limits of various solid electrolytes in all-solid-state lithium batteries: A critical review. *Renew. Sustain. Energy Rev.* **2019**, *109*, 367-385.
- (79) Zheng, Y.; Yao, Y.; Ou, J.; Li, M.; Luo, D.; Dou, H.; Li, Z.; Amine, K.; Yu, A.; Chen, Z., A review of composite solid-state electrolytes for lithium batteries: fundamentals, key materials and advanced structures. *Chem. Soc. Rev.* **2020**, *49* (23), 8790-8839.
- (80) Sandhya, C. P.; John, B.; Gouri, C., Lithium titanate as anode material for lithium-ion cells: a review. *Ionics* **2014**, *20* (5), 601-620.
- (81) Wandt, J.; Freiberg, A. T. S.; Ogorodnik, A.; Gasteiger, H. A., Singlet oxygen evolution from layered transition metal oxide cathode materials and its implications for lithium-ion batteries. *Mater. Today* **2018**, *21* (8), 825-833.

- (82) Manthiram, A.; Knight, J. C.; Myung, S.-T.; Oh, S.-M.; Sun, Y.-K., Nickel-Rich and Lithium-Rich Layered Oxide Cathodes: Progress and Perspectives. *Adv. Energy Mater.* **2016**, *6* (1), 1501010.
- (83) Darago, L. E.; Aubrey, M. L.; Yu, C. J.; Gonzalez, M. I.; Long, J. R., Electronic Conductivity, Ferrimagnetic Ordering, and Reductive Insertion Mediated by Organic Mixed-Valence in a Ferric Semiquinoid Metal–Organic Framework. *Journal of the American Chemical Society* **2015**, *137* (50), 15703-15711.
- (84) Ziebel, M. E.; Darago, L. E.; Long, J. R., Control of Electronic Structure and Conductivity in Two-Dimensional Metal–Semiquinoid Frameworks of Titanium, Vanadium, and Chromium. *Journal of the American Chemical Society* **2018**, *140* (8), 3040-3051.
- (85) DeGayner, J. A.; Jeon, I.-R.; Sun, L.; Dincă, M.; Harris, T. D., 2D Conductive Iron-Quinoid Magnets Ordering up to $T_c = 105$ K via Heterogenous Redox Chemistry. *Journal of the American Chemical Society* **2017**, *139* (11), 4175-4184.
- (86) Benmansour, S.; Abhervé, A.; Gómez-Claramunt, P.; Vallés-García, C.; Gómez-García, C. J., Nanosheets of Two-Dimensional Magnetic and Conducting Fe(II)/Fe(III) Mixed-Valence Metal–Organic Frameworks. *ACS Applied Mater. Interfaces* **2017**, *9* (31), 26210-26218.
- (87) Cheng, X.-F.; Shi, E.-B.; Hou, X.; Shu, J.; He, J.-H.; Li, H.; Xu, Q.-F.; Li, N.-J.; Chen, D.-Y.; Lu, J.-M., 1D π -d Conjugated Coordination Polymers for Multilevel Memory of Long-Term and High-Temperature Stability. *Adv. Electron. Mater.* **2017**, *3* (8), 1700107.
- (88) Cai, G.; Cui, P.; Shi, W.; Morris, S.; Lou, S. N.; Chen, J.; Ciou, J.-H.; Paidi, V. K.; Lee, K.-S.; Li, S.; Lee, P. S., One-Dimensional π -d Conjugated Coordination

Polymer for Electrochromic Energy Storage Device with Exceptionally High Performance. *Adv. Sci.* **2020**, *7* (20), 1903109.

(89) Matsuoka, R.; Sakamoto, R.; Kambe, T.; Takada, K.; Kusamoto, T.; Nishihara, H., Ordered alignment of a one-dimensional π -conjugated nickel bis(dithiolene) complex polymer produced via interfacial reactions. *Chem. Commun.* **2014**, *50* (60), 8137-8139.

(90) Shinde, S. S.; Lee, C. H.; Jung, J.-Y.; Wagh, N. K.; Kim, S.-H.; Kim, D.-H.; Lin, C.; Lee, S. U.; Lee, J.-H., Unveiling dual-linkage 3D hexaiminobenzene metal-organic frameworks towards long-lasting advanced reversible Zn-air batteries. *Energy Environ. Sci.* **2019**, *12* (2), 727-738.

(91) Dou, J.-H.; Sun, L.; Ge, Y.; Li, W.; Hendon, C. H.; Li, J.; Gul, S.; Yano, J.; Stach, E. A.; Dincă, M., Signature of Metallic Behavior in the Metal-Organic Frameworks $M_3(\text{hexaiminobenzene})_2$ ($M = \text{Ni, Cu}$). *Journal of the American Chemical Society* **2017**, *139* (39), 13608-13611.

(92) Jin, Z.; Yan, J.; Huang, X.; Xu, W.; Yang, S.; Zhu, D.; Wang, J., Solution-processed transparent coordination polymer electrode for photovoltaic solar cells. *Nano Energy* **2017**, *40*, 376-381.

(93) Kambe, T.; Sakamoto, R.; Kusamoto, T.; Pal, T.; Fukui, N.; Hoshiko, K.; Shimojima, T.; Wang, Z.; Hirahara, T.; Ishizaka, K.; Hasegawa, S.; Liu, F.; Nishihara, H., Redox Control and High Conductivity of Nickel Bis(dithiolene) Complex π -Nanosheet: A Potential Organic Two-Dimensional Topological Insulator. *Journal of the American Chemical Society* **2014**, *136* (41), 14357-14360.

(94) Kambe, T.; Sakamoto, R.; Hoshiko, K.; Takada, K.; Miyachi, M.; Ryu, J.-H.; Sasaki, S.; Kim, J.; Nakazato, K.; Takata, M.; Nishihara, H., π -Conjugated Nickel

Bis(dithiolene) Complex Nanosheet. *Journal of the American Chemical Society* **2013**, *135* (7), 2462-2465.

(95) Cui, Y.; Yan, J.; Chen, Z.; Zhang, J.; Zou, Y.; Sun, Y.; Xu, W.; Zhu, D., [Cu₃(C₆Se₆)_n]: The First Highly Conductive 2D π -d Conjugated Coordination Polymer Based on Benzenhexaselenolate. *Adv. Sci.* **2019**, *6* (9), 1802235.

(96) Huang, X.; Sheng, P.; Tu, Z.; Zhang, F.; Wang, J.; Geng, H.; Zou, Y.; Di, C.-a.; Yi, Y.; Sun, Y.; Xu, W.; Zhu, D., A two-dimensional π -d conjugated coordination polymer with extremely high electrical conductivity and ambipolar transport behaviour. *Nat. Commun.* **2015**, *6* (1), 7408.

(97) Ko, M.; Aykanat, A.; Smith, M. K.; Mirica, K. A., Drawing Sensors with Ball-Milled Blends of Metal-Organic Frameworks and Graphite. *Sensors* **2017**, *17* (10), 2192.

(98) Mähringer, A.; Jakowetz, A. C.; Rotter, J. M.; Bohn, B. J.; Stolarczyk, J. K.; Feldmann, J.; Bein, T.; Medina, D. D., Oriented Thin Films of Electroactive Triphenylene Catecholate-Based Two-Dimensional Metal-Organic Frameworks. *ACS Nano* **2019**, *13* (6), 6711-6719.

(99) Miner, E. M.; Wang, L.; Dincă, M., Modular O₂ electroreduction activity in triphenylene-based metal-organic frameworks. *Chem. Sci.* **2018**, *9* (29), 6286-6291.

(100) Day, R. W.; Bediako, D. K.; Rezaee, M.; Parent, L. R.; Skorupskii, G.; Arguilla, M. Q.; Hendon, C. H.; Stassen, I.; Gianneschi, N. C.; Kim, P.; Dincă, M., Single Crystals of Electrically Conductive Two-Dimensional Metal-Organic Frameworks: Structural and Electrical Transport Properties. *ACS Cent. Sci.* **2019**, *5* (12), 1959-1964.

- (101) Lian, Y.; Yang, W.; Zhang, C.; Sun, H.; Deng, Z.; Xu, W.; Song, L.; Ouyang, Z.; Wang, Z.; Guo, J.; Peng, Y., Unpaired 3d Electrons on Atomically Dispersed Cobalt Centres in Coordination Polymers Regulate both Oxygen Reduction Reaction (ORR) Activity and Selectivity for Use in Zinc–Air Batteries. *Angew. Chem. Int. Ed.* **2020**, *59* (1), 286-294.
- (102) Campbell, M. G.; Sheberla, D.; Liu, S. F.; Swager, T. M.; Dincă, M., Cu₃(hexaiminotriphenylene)₂: An Electrically Conductive 2D Metal–Organic Framework for Chemiresistive Sensing. *Angew. Chem. Int. Ed.* **2015**, *54* (14), 4349-4352.
- (103) Campbell, M. G.; Liu, S. F.; Swager, T. M.; Dincă, M., Chemiresistive Sensor Arrays from Conductive 2D Metal–Organic Frameworks. *Journal of the American Chemical Society* **2015**, *137* (43), 13780-13783.
- (104) Sheberla, D.; Sun, L.; Blood-Forsythe, M. A.; Er, S.; Wade, C. R.; Brozek, C. K.; Aspuru-Guzik, A.; Dincă, M., High Electrical Conductivity in Ni₃(2,3,6,7,10,11-hexamino-triphenylene)₂, a Semiconducting Metal–Organic Graphene Analogue. *Journal of the American Chemical Society* **2014**, *136* (25), 8859-8862.
- (105) Clough, A. J.; Skelton, J. M.; Downes, C. A.; de la Rosa, A. A.; Yoo, J. W.; Walsh, A.; Melot, B. C.; Marinescu, S. C., Metallic Conductivity in a Two-Dimensional Cobalt Dithiolene Metal–Organic Framework. *Journal of the American Chemical Society* **2017**, *139* (31), 10863-10867.
- (106) Dong, R.; Han, P.; Arora, H.; Ballabio, M.; Karakus, M.; Zhang, Z.; Shekhar, C.; Adler, P.; Petkov, P. S.; Erbe, A.; Mannsfeld, S. C. B.; Felser, C.; Heine, T.; Bonn, M.; Feng, X.; Cánovas, E., High-mobility band-like charge transport in a

semiconducting two-dimensional metal–organic framework. *Nat. Mater.* **2018**, *17* (11), 1027-1032.

(107) Xie, L. S.; Skorupskii, G.; Dincă, M., Electrically Conductive Metal–Organic Frameworks. *Chem. Rev.* **2020**, *120* (16), 8536-8580.

(108) Sheberla, D.; Bachman, J. C.; Elias, J. S.; Sun, C.-J.; Shao-Horn, Y.; Dincă, M., Conductive MOF electrodes for stable supercapacitors with high areal capacitance. *Nat. Mater.* **2017**, *16* (2), 220-224.

(109) Li, W.-H.; Ding, K.; Tian, H.-R.; Yao, M.-S.; Nath, B.; Deng, W.-H.; Wang, Y.; Xu, G., Conductive Metal–Organic Framework Nanowire Array Electrodes for High-Performance Solid-State Supercapacitors. *Adv. Funct. Mater.* **2017**, *27* (27), 1702067.

(110) Feng, D.; Lei, T.; Lukatskaya, M. R.; Park, J.; Huang, Z.; Lee, M.; Shaw, L.; Chen, S.; Yakovenko, A. A.; Kulkarni, A.; Xiao, J.; Fredrickson, K.; Tok, J. B.; Zou, X.; Cui, Y.; Bao, Z., Robust and conductive two-dimensional metal–organic frameworks with exceptionally high volumetric and areal capacitance. *Nat. Energy* **2018**, *3* (1), 30-36.

(111) Lukatskaya, M. R.; Feng, D.; Bak, S.-M.; To, J. W. F.; Yang, X.-Q.; Cui, Y.; Feldblyum, J. I.; Bao, Z., Understanding the Mechanism of High Capacitance in Nickel Hexaaminobenzene-Based Conductive Metal–Organic Frameworks in Aqueous Electrolytes. *ACS Nano* **2020**, *14* (11), 15919-15925.

(112) Banda, H.; Dou, J.-H.; Chen, T.; Libretto, N. J.; Chaudhary, M.; Bernard, G. M.; Miller, J. T.; Michaelis, V. K.; Dincă, M., High-Capacitance Pseudocapacitors from Li⁺ Ion Intercalation in Nonporous, Electrically Conductive 2D Coordination Polymers. *Journal of the American Chemical Society* **2021**, *143* (5), 2285-2292.

- (113) Liu, J.; Zhou, Y.; Xie, Z.; Li, Y.; Liu, Y.; Sun, J.; Ma, Y.; Terasaki, O.; Chen, L., Conjugated Copper–Catecholate Framework Electrodes for Efficient Energy Storage. *Angew. Chem. Int. Ed.* **2020**, *59* (3), 1081-1086.
- (114) Wada, K.; Sakaushi, K.; Sasaki, S.; Nishihara, H., Multielectron-Transfer-based Rechargeable Energy Storage of Two-Dimensional Coordination Frameworks with Non-Innocent Ligands. *Angew. Chem. Int. Ed.* **2018**, *57* (29), 8886-8890.
- (115) Wada, K.; Maeda, H.; Tsuji, T.; Sakaushi, K.; Sasaki, S.; Nishihara, H., Tailoring the Electrochemical Properties of Two-Dimensional Bis(diimino)metal Coordination Frameworks by Introducing Co/Ni Heterometallic Structures. *Inorganic Chemistry* **2020**, *59* (15), 10604-10610.
- (116) Jiang, Q.; Xiong, P.; Liu, J.; Xie, Z.; Wang, Q.; Yang, X.-Q.; Hu, E.; Cao, Y.; Sun, J.; Xu, Y.; Chen, L., A Redox-Active 2D Metal–Organic Framework for Efficient Lithium Storage with Extraordinary High Capacity. *Angew. Chem. Int. Ed.* **2020**, *59* (13), 5273-5277.
- (117) Wang, Z.; Wang, G.; Qi, H.; Wang, M.; Wang, M.; Park, S.; Wang, H.; Yu, M.; Kaiser, U.; Fery, A.; Zhou, S.; Dong, R.; Feng, X., Ultrathin two-dimensional conjugated metal–organic framework single-crystalline nanosheets enabled by surfactant-assisted synthesis. *Chem. Sci.* **2020**, *11* (29), 7665-7671.
- (118) Nam, K. W.; Park, S. S.; dos Reis, R.; Dravid, V. P.; Kim, H.; Mirkin, C. A.; Stoddart, J. F., Conductive 2D metal-organic framework for high-performance cathodes in aqueous rechargeable zinc batteries. *Nat. Commun.* **2019**, *10* (1), 4948.
- (119) Chang, C.-H.; Li, A.-C.; Popovs, I.; Kaveevivitchai, W.; Chen, J.-L.; Chou, K.-C.; Kuo, T.-S.; Chen, T.-H., Elucidating metal and ligand redox activities of a

copper-benzoquinoid coordination polymer as the cathode for lithium-ion batteries.

Journal of Materials Chemistry A **2019**, 7 (41), 23770-23774.

(120) Ziebel, M. E.; Gaggioli, C. A.; Turkiewicz, A. B.; Ryu, W.; Gagliardi, L.; Long, J. R., Effects of Covalency on Anionic Redox Chemistry in Semiquinoid-Based Metal–Organic Frameworks. *Journal of the American Chemical Society* **2020**, 142 (5), 2653-2664.

(121) Wu, Y.; Chen, Y.; Tang, M.; Zhu, S.; Jiang, C.; Zhuo, S.; Wang, C., A highly conductive conjugated coordination polymer for fast-charge sodium-ion batteries: reconsidering its structures. *Chem. Commun.* **2019**, 55 (73), 10856-10859.

(122) Reynolds, J. R.; Jolly, C. A.; Krichene, S.; Cassoux, P.; Faulmann, C., Poly (metal tetrathiooxalates): A structural and charge-transport study. *Synth. Met.* **1989**, 31 (1), 109-126.

(123) Reynolds, J. R.; Chien, J. C. W.; Lillya, C. P., Intrinsically electrically conducting poly(metal tetrathiooxalates). *Macromolecules* **1987**, 20 (6), 1184-1191.

(124) Sun, Y.; Sheng, P.; Di, C.; Jiao, F.; Xu, W.; Qiu, D.; Zhu, D., Organic Thermoelectric Materials and Devices Based on p- and n-Type Poly(metal 1,1,2,2-ethenetetrathiolate)s. *Adv. Mater.* **2012**, 24 (7), 932-937.

(125) Wu, Z.; Adekoya, D.; Huang, X.; Kiefel, M. J.; Xie, J.; Xu, W.; Zhang, Q.; Zhu, D.; Zhang, S., Highly Conductive Two-Dimensional Metal–Organic Frameworks for Resilient Lithium Storage with Superb Rate Capability. *ACS Nano* **2020**, 14 (9), 12016-12026.

(126) Park, J.; Lee, M.; Feng, D.; Huang, Z.; Hinckley, A. C.; Yakovenko, A.; Zou, X.; Cui, Y.; Bao, Z., Stabilization of Hexaaminobenzene in a 2D Conductive

Metal–Organic Framework for High Power Sodium Storage. *Journal of the American Chemical Society* **2018**, *140* (32), 10315-10323.

(127) Dong, S.; Wu, L.; Xue, M.; Li, Z.; Xiao, D.; Xu, C.; Shen, L.; Zhang, X., Conductive Metal–Organic Framework for High Energy Sodium-Ion Hybrid Capacitors. *ACS Applied Energy Mater.* **2021**, *4* (2), 1568-1574.

(128) Xie, J.; Cheng, X.-F.; Cao, X.; He, J.-H.; Guo, W.; Li, D.-S.; Xu, Z. J.; Huang, Y.; Lu, J.-M.; Zhang, Q., Nanostructured Metal–Organic Conjugated Coordination Polymers with Ligand Tailoring for Superior Rechargeable Energy Storage. *Small* **2019**, *15* (49), 1903188.

(129) Chen, Y.; Tang, M.; Wu, Y.; Su, X.; Li, X.; Xu, S.; Zhuo, S.; Ma, J.; Yuan, D.; Wang, C.; Hu, W., A One-Dimensional π -d Conjugated Coordination Polymer for Sodium Storage with Catalytic Activity in Negishi Coupling. *Angew. Chem. Int. Ed.* **2019**, *58* (41), 14731-14739.

(130) Phapale, V. B.; Cárdenas, D. J., Nickel-catalysed Negishi cross-coupling reactions: scope and mechanisms. *Chem. Soc. Rev.* **2009**, *38* (6), 1598-1607.

(131) Mahmood, J.; Kim, D.; Jeon, I.-Y.; Lah, M. S.; Baek, J.-B., Scalable synthesis of pure and stable hexaaminobenzene trihydrochloride. *Synlett* **2013**, *24* (02), 246-248.

(132) Yip, H. K.; Schier, A.; Riede, J.; Schmidbaur, H., Benzenehexathiol as a template rim for a golden wheel: synthesis and structure of [$\{CSAu(PPh_3)\}_6$]. *J. Chem. Soc., Dalton Trans.* **1994**, (15), 2333-2334.

(133) Leriche, J. B.; Hamelet, S.; Shu, J.; Morcrette, M.; Masquelier, C.; Ouvrard, G.; Zerrouki, M.; Soudan, P.; Belin, S.; Elkaïm, E.; Baudalet, F., An Electrochemical Cell for Operando Study of Lithium Batteries Using Synchrotron Radiation. *J. Electrochem. Soc.* **2010**, *157* (5), A606.

- (134) Weaving, J. S.; Lim, A.; Millichamp, J.; Neville, T. P.; Ledwoch, D.; Kendrick, E.; McMillan, P. F.; Shearing, P. R.; Howard, C. A.; Brett, D. J. L., Elucidating the Sodiation Mechanism in Hard Carbon by Operando Raman Spectroscopy. *ACS Applied Energy Mater.* **2020**, *3* (8), 7474-7484.
- (135) Audi, H.; Chen, Z.; Charaf-Eddin, A.; D'Aléo, A.; Canard, G.; Jacquemin, D.; Siri, O., Extendable nickel complex tapes that reach NIR absorptions. *Chem. Commun.* **2014**, *50* (96), 15140-15143.
- (136) Veber, S. L.; Fedin, M. V.; Fokin, S. V.; Sagdeev, R. Z.; Ovcharenko, V. I.; Bagryanskaya, E. G., EPR Study of Ligand Effects in Spin Triads of Bis(o-Semiquinonato)Copper(II) Complexes. *Appl. Magn. Reson.* **2009**, *37* (1), 693.
- (137) Chaudhuri, P.; Verani, C. N.; Bill, E.; Bothe, E.; Weyhermüller, T.; Wieghardt, K., Electronic Structure of Bis(o-iminobenzosemiquinonato)metal Complexes (Cu, Ni, Pd). The Art of Establishing Physical Oxidation States in Transition-Metal Complexes Containing Radical Ligands. *Journal of the American Chemical Society* **2001**, *123* (10), 2213-2223.
- (138) Xu, K., Nonaqueous Liquid Electrolytes for Lithium-Based Rechargeable Batteries. *Chem. Rev.* **2004**, *104* (10), 4303-4418.
- (139) Wagemaker, M.; Mulder, F. M., Properties and Promises of Nanosized Insertion Materials for Li-Ion Batteries. *Acc. Chem. Res.* **2013**, *46* (5), 1206-1215.
- (140) Biesinger, M. C.; Payne, B. P.; Grosvenor, A. P.; Lau, L. W. M.; Gerson, A. R.; Smart, R. S. C., Resolving surface chemical states in XPS analysis of first row transition metals, oxides and hydroxides: Cr, Mn, Fe, Co and Ni. *Appl. Surf. Sci.* **2011**, *257* (7), 2717-2730.

- (141) Zhang, C. Q.; Tu, J. P.; Huang, X. H.; Yuan, Y. F.; Chen, X. T.; Mao, F., Preparation and electrochemical performances of cubic shape Cu₂O as anode material for lithium ion batteries. *J. Alloys Compd.* **2007**, *441* (1), 52-56.
- (142) Fu, L. J.; Gao, J.; Zhang, T.; Cao, Q.; Yang, L. C.; Wu, Y. P.; Holze, R.; Wu, H. Q., Preparation of Cu₂O particles with different morphologies and their application in lithium ion batteries. *J. Power Sources* **2007**, *174* (2), 1197-1200.
- (143) Zhang, S. S., Liquid electrolyte lithium/sulfur battery: Fundamental chemistry, problems, and solutions. *J. Power Sources* **2013**, *231*, 153-162.
- (144) Hayashi, K.; Nemoto, Y.; Tobishima, S.-i.; Yamaki, J.-i., Mixed solvent electrolyte for high voltage lithium metal secondary cells. *Electrochim. Acta* **1999**, *44* (14), 2337-2344.
- (145) Dahbi, M.; Ghamouss, F.; Tran-Van, F.; Lemordant, D.; Anouti, M., Comparative study of EC/DMC LiTFSI and LiPF₆ electrolytes for electrochemical storage. *J. Power Sources* **2011**, *196* (22), 9743-9750.
- (146) Kim, H.-S.; Jeong, C.-S., Electrochemical properties of binary electrolytes for lithium-sulfur batteries. *Bull. Korean Chem. Soc.* **2011**, *32* (10), 3682-3686.
- (147) Kapaev, R. R.; Olthof, S.; Zhidkov, I. S.; Kurmaev, E. Z.; Stevenson, K. J.; Meerholz, K.; Troshin, P. A., Nickel(II) and Copper(II) Coordination Polymers Derived from 1,2,4,5-Tetraaminobenzene for Lithium-Ion Batteries. *Chem. Mater.* **2019**, *31* (14), 5197-5205.
- (148) Kapaev, R. R.; Scherbakov, A. G.; Shestakov, A. F.; Stevenson, K. J.; Troshin, P. A., m-Phenylenediamine as a Building Block for Polyimide Battery Cathode Materials. *ACS Applied Energy Mater.* **2021**, *4* (5), 4465-4472.

- (149) Kapaev, R. R.; Shestakov, A. F.; Vasil'ev, S. G.; Stevenson, K. J., Conjugated Ladder-Type Polymer with Hexaazatriphenylene Units as a Cathode Material for Lithium, Sodium, and Potassium Batteries. *ACS Applied Energy Mater.* **2021**, *4* (10), 10423-10427.
- (150) Kapaev, R. R.; Troshin, P. A., Organic-based active electrode materials for potassium batteries: status and perspectives. *J. Mater. Chem. A* **2020**, *8* (34), 17296-17325.
- (151) Cui, Y.; Liu, W.; Wang, X.; Li, J.; Zhang, Y.; Du, Y.; Liu, S.; Wang, H.; Feng, W.; Chen, M., Bioinspired Mineralization under Freezing Conditions: An Approach to Fabricate Porous Carbons with Complicated Architecture and Superior K⁺ Storage Performance. *ACS Nano* **2019**, *13* (10), 11582-11592.
- (152) Patry, G.; Romagny, A.; Martinet, S.; Froelich, D., Cost modeling of lithium-ion battery cells for automotive applications. *Energy Science & Engineering* **2015**, *3* (1), 71-82.
- (153) Wood, D. L.; Li, J.; Daniel, C., Prospects for reducing the processing cost of lithium ion batteries. *J. Power Sources* **2015**, *275*, 234-242.
- (154) Molina, A.; Patil, N.; Ventosa, E.; Liras, M.; Palma, J.; Marcilla, R., Electrode Engineering of Redox-Active Conjugated Microporous Polymers for Ultra-High Areal Capacity Organic Batteries. *ACS Energy Lett.* **2020**, *5* (9), 2945-2953.
- (155) Yang, J.; Li, D.; Wang, X.; Zhang, X.; Xu, J.; Chen, J., Constructing micro-nano Na₃V₂(PO₄)₃/C architecture for practical high-loading electrode fabrication as superior-rate and ultralong-life sodium ion battery cathode. *Energy Storage Mater.* **2020**, *24*, 694-699.

- (156) Saverina, E. A.; Kapaev, R. R.; Stishenko, P. V.; Galushko, A. S.; Balycheva, V. A.; Ananikov, V. P.; Egorov, M. P.; Jouikov, V. V.; Troshin, P. A.; Syroeshkin, M. A., 2-Carboxyethylgermanium Sesquioxide as A Promising Anode Material for Li-Ion Batteries. *ChemSusChem* **2020**, *13* (12), 3137-3146.
- (157) Nikitina, V. A.; Vassiliev, S. Y.; Stevenson, K. J., Metal-Ion Coupled Electron Transfer Kinetics in Intercalation-Based Transition Metal Oxides. *Adv. Energy Mater.* **2020**, *10* (22), 1903933.
- (158) Klix, A.; Verzilov, Y.; Ochiai, K.; Nishitani, T.; Takahashi, A., Heterogeneous breeding blanket experiment with lithium titanate and beryllium. *Fusion Eng. Des.* **2005**, *72* (4), 327-337.
- (159) Liang, Y.; Jing, Y.; Gheyhani, S.; Lee, K.-Y.; Liu, P.; Facchetti, A.; Yao, Y., Universal quinone electrodes for long cycle life aqueous rechargeable batteries. *Nat. Mater.* **2017**, *16* (8), 841-848.
- (160) Ding, Y.; Li, Y.; Yu, G., Exploring Bio-inspired Quinone-Based Organic Redox Flow Batteries: A Combined Experimental and Computational Study. *Chem* **2016**, *1* (5), 790-801.
- (161) Liang, Y.; Zhang, P.; Yang, S.; Tao, Z.; Chen, J., Fused Heteroaromatic Organic Compounds for High-Power Electrodes of Rechargeable Lithium Batteries. *Adv. Energy Mater.* **2013**, *3* (5), 600-605.
- (162) Häupler, B.; Burges, R.; Janoschka, T.; Jähnert, T.; Wild, A.; Schubert, U. S., PolyTCAQ in organic batteries: enhanced capacity at constant cell potential using two-electron-redox-reactions. *J. Mater. Chem. A* **2014**, *2* (24), 8999-9001.

- (163) Schmidt, D.; Häupler, B.; Stolze, C.; Hager, M. D.; Schubert, U. S., Poly[N-(10-oxo-2-vinylanthracen-9(10H)-ylidene)cyanamide] as a novel cathode material for li-organic batteries. *J. Polym. Sci., Part A: Polym. Chem.* **2015**, *53* (21), 2517-2523.
- (164) Li, X.; Sun, X.; Hu, X.; Fan, F.; Cai, S.; Zheng, C.; Stucky, G. D., Review on comprehending and enhancing the initial Coulombic efficiency of anode materials in lithium-ion/sodium-ion batteries. *Nano Energy* **2020**, *77*, 105143.
- (165) He, H.; Sun, D.; Tang, Y.; Wang, H.; Shao, M., Understanding and improving the initial Coulombic efficiency of high-capacity anode materials for practical sodium ion batteries. *Energy Storage Mater.* **2019**, *23*, 233-251.
- (166) Guo, B.; Shu, J.; Wang, Z.; Yang, H.; Shi, L.; Liu, Y.; Chen, L., Electrochemical reduction of nano-SiO₂ in hard carbon as anode material for lithium ion batteries. *Electrochem. Commun.* **2008**, *10* (12), 1876-1878.
- (167) Wu, J.; Rui, X.; Long, G.; Chen, W.; Yan, Q.; Zhang, Q., Pushing Up Lithium Storage through Nanostructured Polyazaacene Analogues as Anode. *Angew. Chem. Int. Ed.* **2015**, *54* (25), 7354-7358.
- (168) Wang, C.; Tang, W.; Yao, Z.; Chen, Y.; Pei, J.; Fan, C., Using an organic acid as a universal anode for highly efficient Li-ion, Na-ion and K-ion batteries. *Org. Electron.* **2018**, *62*, 536-541.
- (169) Darwiche, A.; Bodenes, L.; Madec, L.; Monconduit, L.; Martinez, H., Impact of the salts and solvents on the SEI formation in Sb/Na batteries: An XPS analysis. *Electrochim. Acta* **2016**, *207*, 284-292.
- (170) Bodenes, L.; Darwiche, A.; Monconduit, L.; Martinez, H., The Solid Electrolyte Interphase a key parameter of the high performance of Sb in sodium-ion

batteries: Comparative X-ray Photoelectron Spectroscopy study of Sb/Na-ion and Sb/Li-ion batteries. *J. Power Sources* **2015**, *273*, 14-24.

(171) Zhao, J.; Yang, X.; Yao, Y.; Gao, Y.; Sui, Y.; Zou, B.; Ehrenberg, H.; Chen, G.; Du, F., Moving to Aqueous Binder: A Valid Approach to Achieving High-Rate Capability and Long-Term Durability for Sodium-Ion Battery. *Adv. Sci.* **2018**, *5* (4), 1700768.

(172) Grosvenor, A. P.; Biesinger, M. C.; Smart, R. S. C.; McIntyre, N. S., New interpretations of XPS spectra of nickel metal and oxides. *Surf. Sci.* **2006**, *600* (9), 1771-1779.

(173) Clark, R. J.; Stewart, B., The resonance raman effect—Review of the theory and of applications in inorganic chemistry. In *Inorganic Chemistry and Spectroscopy*, Springer: Berlin, Heidelberg, 1979; Vol. 36, pp 1-80.

(174) Sharif Sh, M.; Golestani Fard, F.; Khatibi, E.; Sarpoolaky, H., Dispersion and stability of carbon black nanoparticles, studied by ultraviolet–visible spectroscopy. *Journal of the Taiwan Institute of Chemical Engineers* **2009**, *40* (5), 524-527.

(175) Russo, C.; Apicella, B.; Lighty, J. S.; Ciajolo, A.; Tregrossi, A., Optical properties of organic carbon and soot produced in an inverse diffusion flame. *Carbon* **2017**, *124*, 372-379.

(176) Cong, G.; Wang, W.; Lai, N.-C.; Liang, Z.; Lu, Y.-C., A high-rate and long-life organic–oxygen battery. *Nat. Mater.* **2019**, *18* (4), 390-396.

(177) Kapaev, R. R.; Stevenson, K. J., Solution-based chemical pre-alkaliation of metal-ion battery cathode materials for increased capacity. *J. Mater. Chem. A* **2021**, *9* (19), 11771-11777.

- (178) Dose, W. M.; Kim, S.; Liu, Q.; Trask, S. E.; Dunlop, A. R.; Ren, Y.; Zhang, Z.; Fister, T. T.; Johnson, C. S., Dual functionality of over-lithiated NMC for high energy silicon-based lithium-ion batteries. *J. Mater. Chem. A* **2021**, *9* (21), 12818-12829.
- (179) Wang, F.; Wang, B.; Li, J.; Wang, B.; Zhou, Y.; Wang, D.; Liu, H.; Dou, S., Prelithiation: A Crucial Strategy for Boosting the Practical Application of Next-Generation Lithium Ion Battery. *ACS Nano* **2021**, *15* (2), 2197-2218.
- (180) Herebian, D.; Bothe, E.; Neese, F.; Weyhermüller, T.; Wieghardt, K., Molecular and Electronic Structures of Bis-(o-diiminobenzosemiquinonato)metal(II) Complexes (Ni, Pd, Pt), Their Monocations and -Anions, and of Dimeric Dications Containing Weak Metal–Metal Bonds. *Journal of the American Chemical Society* **2003**, *125* (30), 9116-9128.

Appendix A. Supplementary materials

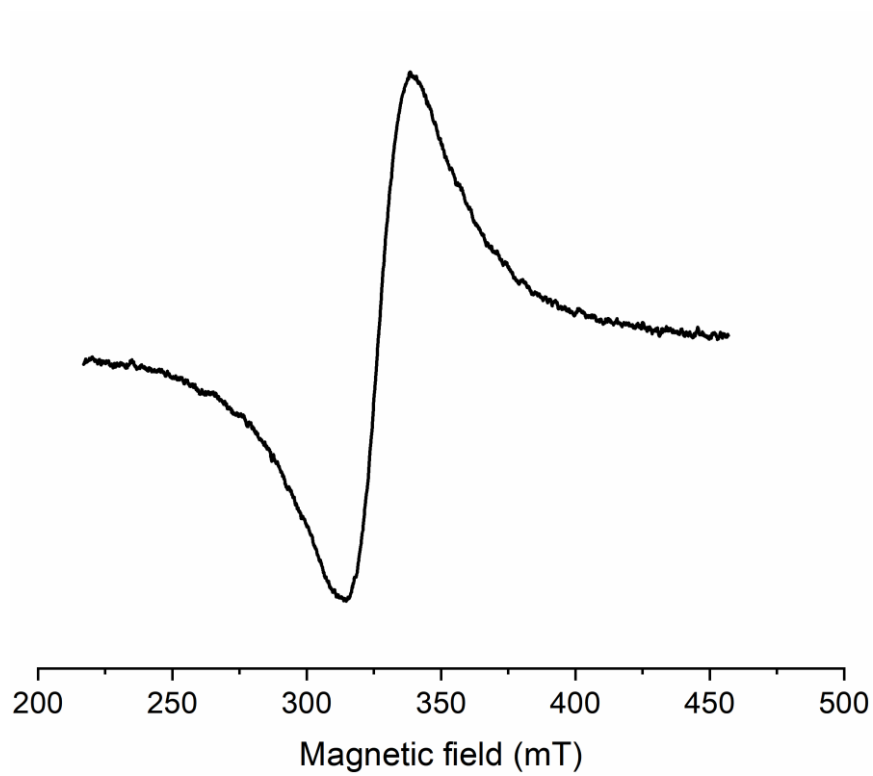


Figure A1. ESR spectrum of **CuTIB**.

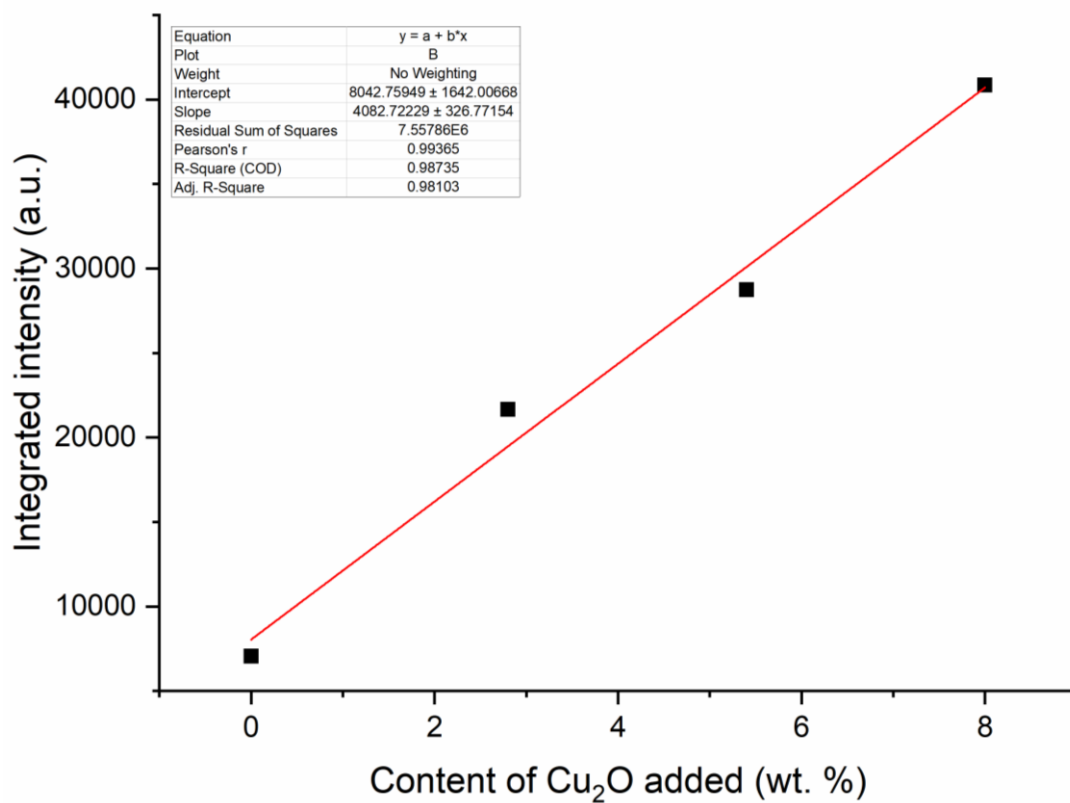


Figure A2. Intensity of Cu₂O peak (hkl = 111) in **CuTIB** sample depending on the amount of Cu₂O added.

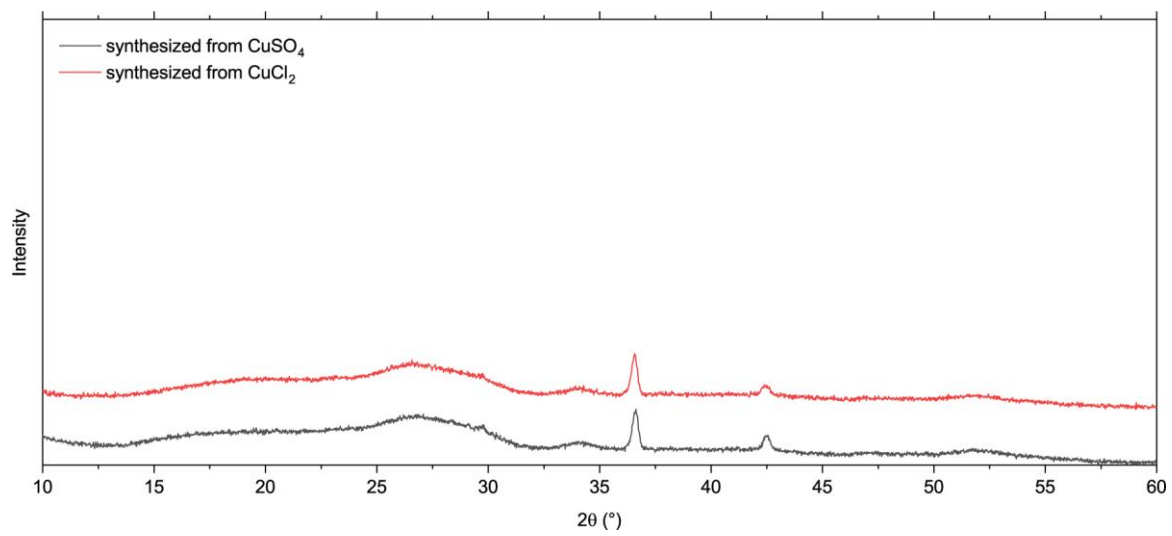


Figure A3. XRD patterns of **CuTIB** obtained from copper sulfate and copper chloride.

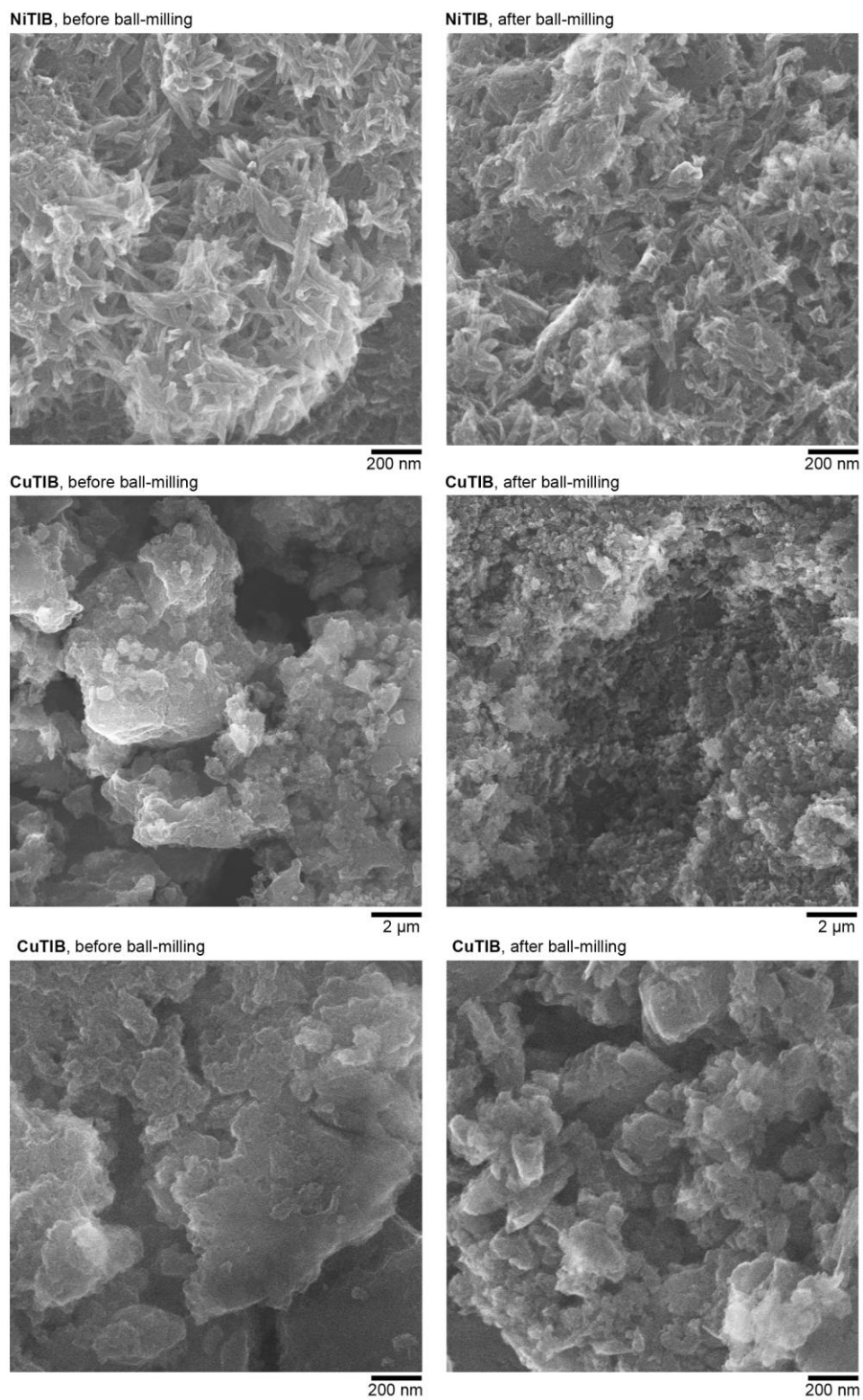


Figure A4. SEM images of NiTiB and CuTiB before/after ball-milling.

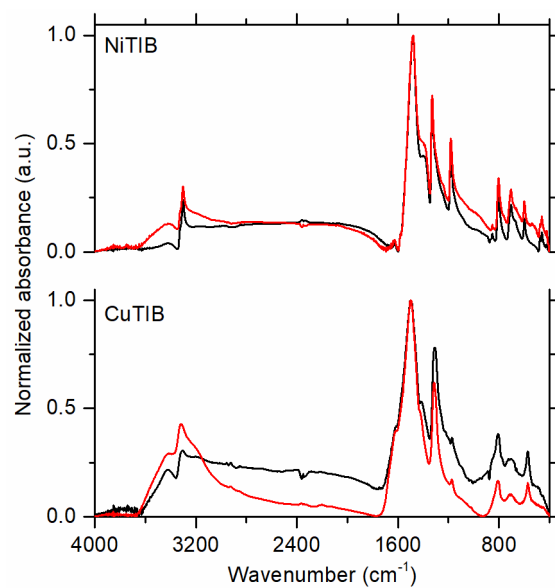


Figure A5. FTIR spectra of as-synthesized (black lines) and ball-milled (red lines) **NiTiB** and **CuTiB**.

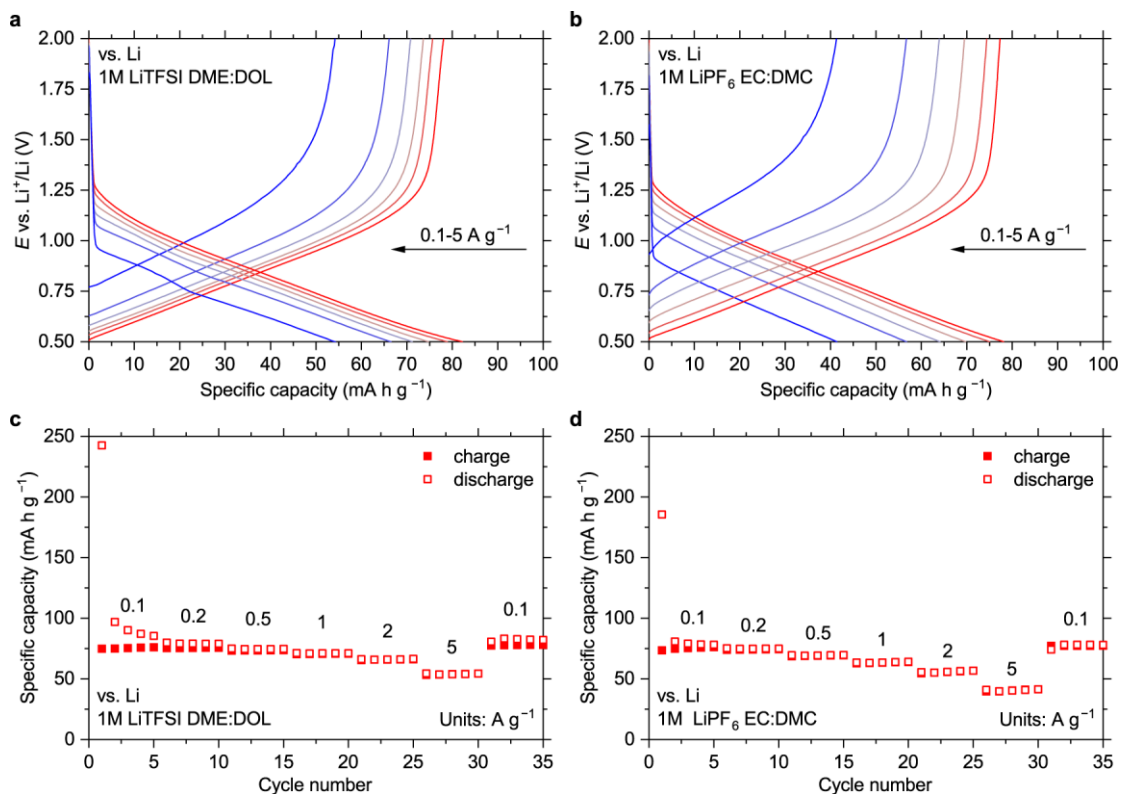


Figure A6. Charge-discharge curves of Super P in lithium-based cells with the ether-based (a) and carbonate-based (b) electrolytes at 0.1, 0.2, 0.5, 1, 2 and 5 A g^{-1} ; dependencies of charge and discharge capacities on the cycle number at varying current densities for the cells with ether-based (c) and carbonate-based (d) electrolytes.

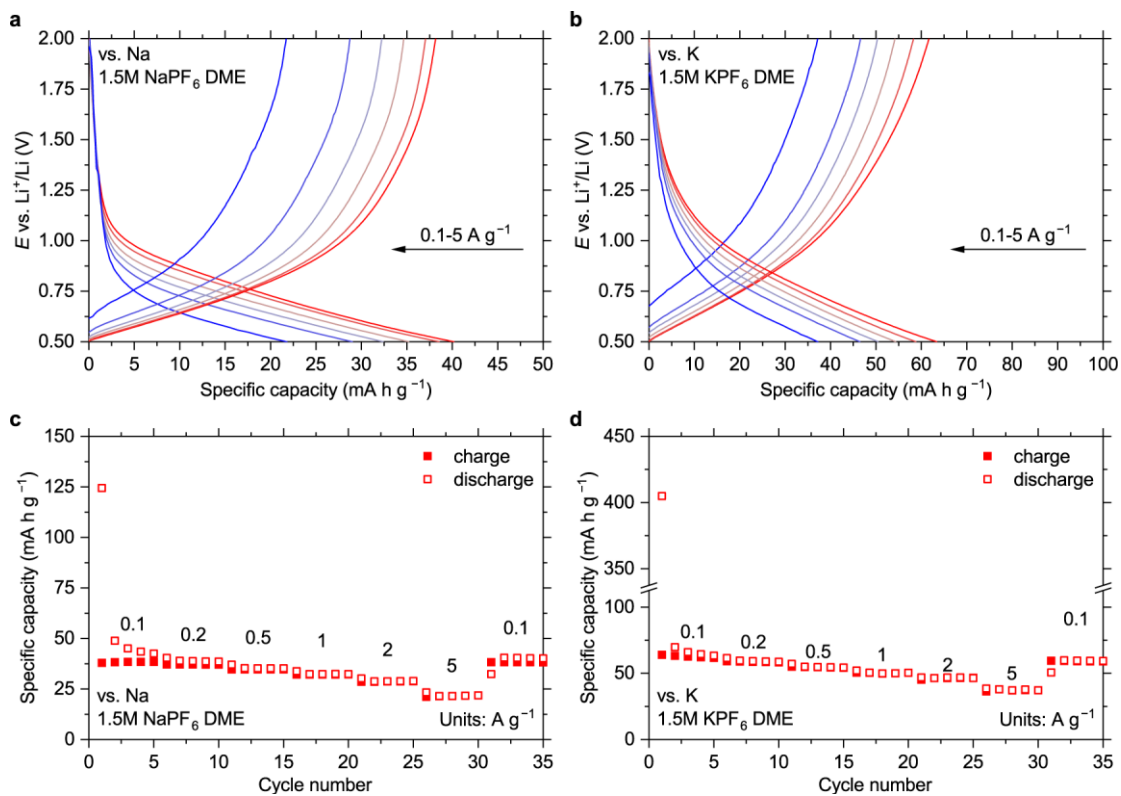


Figure A7. Charge-discharge curves of Super P in sodium-based (a) and potassium-based cells (b) at 0.1, 0.2, 0.5, 1, 2 and 5 A g⁻¹; dependencies of charge and discharge capacities on the cycle number at varying current densities for sodium-based (c) and potassium-based cells (d).

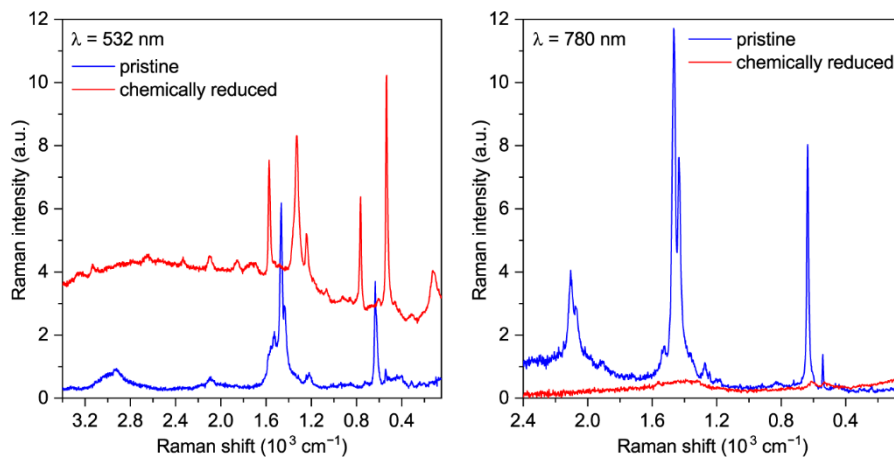


Figure A8. Raman spectra of NiBTA-based films before and after chemical reduction measured with the green (left) and infrared (right) lasers.